NACA RM A55J03

NACA

RESEARCH MEMORANDUM

STATIC LATERAL-DIRECTIONAL STABILITY CHARACTERISTICS OF FIVE CONTEMPORARY AIRPLANE MODELS FROM WIND-TUNNEL TESTS AT HIGH SUBSONIC AND SUPERSONIC SPEEDS

By Willard G. Smith and Louis H. Ball

Ames Aeronautical Laboratory
Moffett Field, Calif.

NATIONAL ADVISORY COMMITTEE FOR AERONAUTICS

WASHINGTON

January 4, 1956

NACA RM A55J03

NATIONAL ADVISORY COMMITTEE FOR AERONAUTICS

RESEARCH MEMORANDUM

STATIC LATERAL-DIRECTIONAL STABILITY CHARACTERISTICS OF FIVE CONTEMPORARY AIRPLANE MODELS FROM WIND-TUNNEL TESTS AT HIGH SUBSONIC AND SUPERSONIC SPEEDS

By Willard G. Smith and Louis H. Ball

SUMMARY

This report presents the static lateral-directional stability characteristics of several airplane models recently investigated which cover many of the geometric arrangements of high-speed airplane components of current interest. The measured aerodynamic qualities afford information on the aerodynamic derivatives required for calculation of airplane motions. The results are presented for a subsonic Mach number of 0.9 and for supersonic Mach numbers ranging from 1.2 to 1.9. The Reynolds numbers of the tests ranged from 1 to 4 million based on the mean aerodynamic chord.

Discussion of the results is limited to the most pertinent aerodynamic phenomena contributing to the lateral-directional characteristics of each airplane type. The directional stability of all the models deteriorated with increasing angle of attack and increasing Mach number. Interference effects are shown to have a strong influence upon the vertical-tail effectiveness and, consequently, upon the directional stability. These effects are, for the most part, associated with complex flow involving vorticity or shock waves and are, therefore, difficult to analyze. In order to expedite publication no analysis has been made. The data, however, serve to give some insight into the basic phenomena involved.

INTRODUCTION

Much attention is being focused on the lateral-directional stability of aircraft capable of flight at supersonic speeds. The low-aspect-ratio wings and high-fineness-ratio bodies necessary to satisfy the low drag requirements of these airplanes have increased the complexity of the aerodynamic problems encountered in their design. The use of far rearward

center-of-gravity locations with the consequent short tail arms further aggravates the situation. Only a small amount of aerodynamic data is available for a study of these problems. For this reason, a review of existing pertinent data was undertaken with a view toward supplying some of this needed information.

It is the purpose of this report to summarize some of the current information regarding lateral-directional characteristics. These data were obtained, for the most part, from developmental wind-tunnel tests of predetermined model configurations as requested by the military services. The five models for which results are presented (see fig. 1) are believed to be fairly representative of current design philosophy concerning airplanes capable of flight speeds of the order of twice the speed of sound.

NOTATION

All results are presented in standard NACA coefficient form with the forces referred to the wind axes and the moments referred to the stability axes. In the stability system the Z axis lies in the plane of symmetry and is normal to the relative wind; the Y axis is normal to the plane of symmetry; and the X axis is normal to the Y and Z axes. (See table I for moment center locations.) The notation and definitions used in this report are as follows:

C_n yawing-moment coefficient, $\frac{\text{yawing moment}}{qSb}$

C_c cross-wind-force coefficient, $\frac{\text{cross-wind force}}{qS}$

C_l rolling-moment coefficient, $\frac{\text{rolling moment}}{qSb}$

C_{n_β} rate of change of yawing-moment coefficient with sideslip angle, per deg

C_{c_β} rate of change of cross-wind-force coefficient with sideslip angle, per deg

C_{l_β} rate of change of rolling-moment coefficient with sideslip angle, per deg

$\frac{C_n}{\beta}$ yawing-moment coefficient measured at a sideslip angle of 5° divided by 5°, per deg

[redacted]

$\frac{C_c}{\beta}$ cross-wind-force coefficient measured at a sideslip angle of 5° divided by 5°, per deg

$\frac{C_l}{\beta}$ rolling-moment coefficient measured at a sideslip angle of 5° divided by 5°, per deg

M free-stream Mach number

S total wing area including the area formed by extending the leading and trailing edges to the vertical plane of symmetry, sq ft

b wing span, ft

$\bar{c}$ mean aerodynamic chord of the wing, ft

$\frac{m}{m_\infty}$ ratio of mass flow through duct to mass flow through an equivalent stream tube in the free stream

q free-stream dynamic pressure, lb/sq ft

α angle of attack measured between the projection of the relative wind in the plane of symmetry and the wing chord plane, deg

β sideslip angle measured between the relative wind and the vertical plane of symmetry, deg

APPARATUS

Wind Tunnel and Equipment

These investigations were conducted in the Ames 6- by 6-foot supersonic wind tunnel. This wind tunnel is of the closed-return, variable-pressure type in which the pressure and Mach number can be continuously varied. Stagnation pressures from 2 to 17 pounds per square inch absolute and Mach numbers from 0.60 to 0.90 and from 1.20 to 1.90 can be obtained. A complete description of the wind tunnel is given in reference 1.

The models in each case were sting-mounted with the plane of movement of the system horizontal to utilize the most uniform stream conditions (see ref. 1). The aerodynamic forces and moments were measured with an electrical strain-gage balance enclosed within the model. The electric unbalance in the strain-gage circuits were registered by recording-type galvanometers which were calibrated by applying known loads to the balance.

[redacted]

Models used during these tests were of polished metal construction. The models were all constructed so that the various component parts could be removed or modified. Two models were used in performing the tests of Model E. These models were essentially identical but one of the models incorporated certain modifications to allow for internal air flow. In the main, these modifications consisted of removing the side-inlet fairings, adding a duct exit fairing through which air egressed to the free stream, and extending and altering slightly the rear fuselage lines so as to accommodate both the duct exit fairing and the sting. Also the wing leading-edge flaps were deflected down 3° for a concurrent investigation of certain longitudinal characteristics of this ducted model. The primary geometric characteristics of the models are presented in table I.

TESTS AND PROCEDURE

The range of test conditions for the five models varies somewhat since this report is a compilation of five separate tests. Data were obtained for Mach numbers of 0.9 and for a supersonic range of about 1.2 to 1.9. The lowest supersonic test Mach number for a particular model was somewhat higher for the larger models in order that the shock waves reflected from the tunnel walls would not intersect any part of the model. The range of test variables for each model also differed somewhat. Data were obtained over a range of sideslip angles of about plus and minus 5° in increments of 2°. In some tests the plus range was extended to 8°. For those tests with angle of sideslip as the primary variable, the angle of attack was held constant; generally at 0° or 5°. The Reynolds number was held constant for each model with values ranging from 1 to 4 million for the various models.

Tests were made for several of the models with sideslip angle held constant at 5° while the angle of attack was varied from -4° to about 18° in increments of 2°. The lateral-directional stability parameters C_n/β, C_c/β, and C_l/β were obtained from these data by taking increments between the results obtained at sideslip angles of plus and minus 5°. These values may disagree somewhat with the derivatives taken through zero angle of sideslip due to nonlinearities in the curves. The primary usefulness of these figures is then to show the variation with angle of attack of the lateral-directional stability derivatives.

Corrections to the data to account for the effects of stream irregularities known to exist in the wind tunnel (ref. 1) were obtained by testing each model in the upright and inverted attitudes. The correction was taken as one half of the difference between the slope of the upright and the inverted data (taken at $\beta = 0°$ and $\alpha = 0°$). Since the effects of stream irregularities were obtained from an analysis of the test results, it was not practical to include them in the computation of the basic data

which is presented herein as plots with angle of sideslip or attack as the primary variable. However, the lateral-directional stability derivatives have been corrected for the effects of stream irregularities in those figures where Mach number is the primary variable. The stability derivatives were obtained by taking the slopes of the basic plots (which are uncorrected) and applying the corrections for stream effects from table II.

A flow-visualization technique known as the "vapor-screen method" was used in tests of Model D to qualitatively study the flow field in the vicinity of the tail. A rather complete description of the technique is given in reference 2. In the present investigation the camera, used to photograph the vapor screen, was mounted directly behind the model in a manner similar to the rear camera in reference 2.

RESULTS

The lateral-directional stability characteristics of the various models are presented in plots of C_{n_β}, C_{c_β}, and C_{l_β} versus Mach number. The basic plots of C_n, C_c, and C_l versus β are also presented, primarily to show the nonlinearity with sideslip angle. However, as previously noted, the basic data plots have not been corrected for the effects of stream irregularities and should be used with consideration of the corrections listed in table II.

The results of these tests are grouped according to models. No comparison of the test results for the various models is made. In order to facilitate identification of the model configuration for which the data in a particular graph pertain, a silhouette of the basic model configuration is shown in the upper portion of each graph. Any modifications or additions to the model are shown as a dashed line on the silhouette. The form of presentation for each model group is as follows:

1. Dimensional sketch of the model.

2. Variation of yawing-moment, rolling-moment, and cross-wind-force coefficient with angle of sideslip.

3. Variation of the lateral-directional stability parameters C_n/β, C_c/β, and C_l/β with angle of attack.

4. Variation of the lateral-directional stability derivatives with Mach number.

An index of the results is presented in table III. In general, this order of presentation is adhered to throughout this report. However, in

certain of the tests (Models C and E) the range of variables was insufficient to warrant the complete presentation used for the other models.

DISCUSSION

It is the intent to discuss herein only the broad aspects of the lateral-directional characteristics of each particular model and to point out the pertinent aerodynamic factors contributing to the results. Possible conclusions to be drawn from a comparison of the aerodynamic qualities of the models are left to the reader.

Model A

At supersonic speeds, externally mounted nacelles (or stores) can have large aerodynamic effects, particularly upon directional stability. This fact is significantly illustrated in the data for Model A, the geometric characteristics of which are shown in figure 2. Detailed information concerning the effects of nacelle position upon the lateral-directional characteristics of this model for both tail-on and tail-off configurations is presented in figure 3. The variation of C_l/β, C_c/β, and C_n/β with angle of attack is shown in figure 4 for the model with Siamese nacelles. Portions of the data presented in figure 3 are more conveniently summarized in figure 5.

Interference effects of the nacelles on the vertical-tail effectiveness can be seen best by comparing the directional stability of the model with the nacelles off (dashed line in fig. 5(a)) and with the outboard nacelles mounted in the wing chord plane (solid line in fig. 5(b)). At the lowest supersonic Mach number where comparable data exist (Mach number of 1.6), the model with chord-plane-mounted nacelles shows a substantial decrease in directional stability relative to that of the model without nacelles. The difference between the directional stability for the two configurations diminishes with increasing Mach number to the extent that at a Mach number of 1.9, essentially no effect of the nacelles upon this parameter is evident. The decreased directional stability for the model with outboard nacelles mounted in the wing chord plane is evidently caused by the compression waves from these nacelles which impinge upon the vertical tail. The effect of these waves is to decrease the loading on the vertical tail due to sideslip and consequently to decrease the directional stability. To illustrate how the outboard nacelles influence the directional stability, consider the case of a positive sideslip angle (right wing advanced). The inboard side of the right nacelle becomes an expansion surface while the inboard side of the left nacelle becomes a corresponding compression surface. When the expansion waves from the right nacelle and the compression waves from the left nacelle impinge on the vertical tail,

the differential loading results in a destabilizing force on the vertical tail. It can be seen that the nacelle-vertical-tail interference depends on the relative location of the nacelle Mach cones and the vertical tail. This interference, for a given outboard nacelle location, is then a function of Mach number, angle of sideslip, and angle of attack. At higher supersonic speeds, the pressure disturbances from these nacelles which are propagated nearly along Mach lines move rearward. The boundary of the area of the vertical tail influenced by these pressures, therefore, moves rearward and the extent of this region diminishes with increasing Mach number. At a Mach number of 1.9 the pressure disturbances apparently pass behind the vertical tail. However, the tail moves into the disturbance region with increasing sideslip angle resulting, as shown in figure 3(c), in decreased directional stability at sideslip angles larger than 4° at a Mach number of 1.75 and larger than 6° at a Mach number of 1.9.

The results show a general decrease in directional stability with increasing angle of attack for this model with several nacelle arrangements (figs. 5(d) through 5(f)). The reduction in directional stability is believed to be the result of a loss in the effectiveness of the vertical tail which, at supersonic speed, occurs primarily because of the decreased dynamic pressure associated with the expansion of the air stream over the upper surface of the wing at positive angles of attack. The forward position of the vertical tail relative to the wing contributes to its vulnerability from this source, particularly at the higher Mach numbers.

Another effect of angle of attack on directional stability is shown for the model with chord-plane-mounted outboard nacelles (fig. 5(d)). Results in the figure show not only a decrease in stability at an angle of attack of 8° compared to an angle of attack of 3°, but also a considerably different variation with Mach number. Since the relative position of the vertical tail with respect to the Mach cones from the nacelles changes with angle of attack, it is conceivable that at an angle of attack of 8° the interference effects previously discussed might occur at a higher Mach number and that the strength of these effects might be changed.

Not all the nacelle arrangements tested decreased the directional stability. Specifically, when the model was fitted with outboard nacelles mounted under the wing, adverse interference effects were not evident. In these cases the vertical tail was shielded from the outboard nacelles by the wing.

Two modifications were made to the chord-plane-mounted nacelles to improve the directional stability of the model. The outboard nacelles were pitched down 5° from their original position to lower the inlets, and the nacelles were rotated inboard (again from the original position) to bring their inlets closer to the vertical plane of symmetry. The results of these nacelle modifications on the directional stability (fig. 5(b)) indicate that small changes in shielding of the vertical tail or in location of the nacelle Mach cones relative to the vertical tail

can reduce the interference effects considerably. Part of the increased stability for the model with "toed-in" nacelles is due to direct air loads on the nacelles as the asymmetric nacelle drag in sideslip is stabilizing. It might be noted that a chordwise shift of the inboard nacelle has no unusual effect on the lateral-directional stability characteristics of the model (fig. 5(c)).

The consequence of a sudden engine failure for an airplane with external engine nacelles mounted well outboard of the plane of symmetry is of considerable concern. In this investigation the static-lateral-directional stability characteristics were obtained for the model with an outboard nacelle plugged to simulate this condition. These data show only the aerodynamic effects of reducing the duct mass-flow ratio to zero and no attempt was made to simulate asymmetric thrust conditions. Two nacelle arrangements were tested in this condition. Figure 3(h) presents results for a plugged chord-plane-mounted nacelle while figure 3(q) is a plugged pylon-mounted nacelle. The same nacelle arrangements, unplugged, are shown in figures 3(c) and 3(n). Both nacelle arrangements with the port outboard nacelle plugged exhibited a small increment of negative yawing moment, compared to the symmetrical condition, which increased with speed to an unbalanced equivalent to a 2° yaw angle at a Mach number of 1.9 for the chord-plane-mounted nacelles. The directional stability of the model with a chord-plane-mounted outboard nacelle plugged was decreased slightly while the pylon-mounted outboard nacelles showed little change except at a Mach number of 1.90 where both arrangements show a sizable decrease in directional stability. The erratic variation of the lateral-directional characteristics with sideslip angle for the model with a chord-plane-mounted nacelle plugged (fig. 3(h)) is probably the result of the nacelle-tail interference previously discussed (note that these variations did not occur for the model with pylon-mounted nacelles). It is difficult to analyze the effects of nacelle-tail interference for one outboard nacelle plugged since the Mach cones from the nacelles are no longer symmetrical and the position of the detached bow wave in the vicinity of the vertical tail cannot be predicted.

The conical camber in the wing of Model A was incorporated for reasons other than those pertaining to the lateral-directional stability characteristics. Tests were not made to evaluate the extent to which this camber influenced the present results, although it is believed to have but a small effect. Conical camber and its influence on the lateral-directional stability characteristics of a wing similar to that of Model A is discussed in reference 3.

Model B

The three-view drawing of this model (fig. 6) shows the wing plan form to be basically triangular, but modified by rounded tips and indented trailing edges. The model had a sweptback vertical tail but no horizontal tail. Side inlets were incorporated in the fuselage. These engine inlets blended into the wing root as a fillet-type fairing. Air flowed through internal ducts and exhausted at the rear of the fuselage at mass-flow ratios that were representative of flight conditions.

The lateral-directional stability characteristics versus sideslip angle of Model B (presented in fig. 7) showed no anomalous variations with angle of attack or Mach number. The decrease in directional stability with increasing angle of attack (fig. 8) is believed to be due primarily to a decrease in tail effectiveness resulting from the decrease in dynamic pressure associated with the expansion of the air stream passing over the upper surface of the wing at angle of attack. The decrease in directional stability with Mach number (fig. 9) is no greater than would be expected, from consideration of compressibility effects.

The variation of rolling-moment coefficient with angle of attack and Mach number shown by this model (fig. 8) is an intrinsic property of the wing plan form. The variation of the parameter C_l/β with angle of attack is negative and reduces in magnitude as the Mach number increases to $M = 1.65$. The slope of the C_l/β curve is positive for a Mach number of 1.90 where the component of velocity perpendicular to the wing leading edge is supersonic. These results, including the reversal of sign when the wing leading edge becomes supersonic, are in good agreement with predictions based on linearized potential theory (ref. 4) for a triangular wing of aspect ratio 2.

Model C

The aerodynamic results for Model C illustrate the lateral-directional stability characteristics of a triangular-wing airplane similar to Models A and B, but stabilized by twin vertical fins mounted midway out on the wing (see fig. 10). This model also had a longitudinal control surface, detached from the wing trailing edge, which was believed to have only a secondary effect on the directional characteristics. The wind-tunnel investigation from which these data were obtained was concerned primarily with the longitudinal characteristics of the model; however, a limited amount of lateral data was obtained. These data are considered to be important since they point out the existence of severe lateral-directional stability reversals which might occur for any airplane, during certain flight conditions, with a highly swept wing leading edge and with vertical fins mounted outboard on the wing.

[redacted]

Figure 11 presents the lateral-directional stability characteristics of Model C at angles of attack of 0°, 5°, and 10°. The data are only slightly nonlinear at 0° and 5° (figs. 11(a) and 11(b)); however, at 10° angle of attack (fig. 11(c)) the yawing-moment and rolling-moment characteristics for the two subsonic Mach numbers show reversals at small angles of sideslip. An examination was made of the longitudinal aerodynamic characteristics of the model (not presented in this report) which also revealed discontinuities in the 10° angle-of-attack region. The lift-curve slope decreased slightly and there was a forward shift in the center-of-pressure location which would indicate the onset of a wing-tip stall. Similar variations in the longitudinal characteristics were observed in reference 5 with regard to an aspect-ratio-2 triangular wing even though no fins were mounted on the wing. In reference 5, it was noted that these variations result from the failure of the separated flow at the leading edge of the wing to reattach over the outboard portion of the wing at the higher angles of attack. It is apparent then that in the neighborhood of 10° angle of attack the wing of Model C is in a critical region of tip stall. Further, it is believed that the presence of the vertical fins near the critical region of detached flow has an adverse effect on the flow pattern over the wing and that, when separation occurs, the entire portion of the wing outboard of the fins stalls. It is conjectured that when the model was yawed at an angle of attack of 10°, the change of the air-flow pattern over the wing resulting from the decrease in effective sweep angle caused a premature stall on the advancing wing. The sudden stalling of the advancing wing tip produces the reversal of dihedral effect found near zero sideslip angle. The decrease in directional stability which accompanies the rolling-moment variations is due to mutual interference between the wing tips and fins. The tip stall on the advancing wing apparently decreases the effectiveness of the adjacent fin. These observations are substantiated by the results of an investigation (ref. 6) of the effects of outboard fins on the static-stability and rolling characteristics of a triangular wing model. The results presented in figure 11(c) are somewhat erratic (rolling-moment and yawing-moment curves lack symmetry) because of the difficulty in obtaining consistent data for the unsteady flow conditions associated with the wing-tip stall.

Model D

The lateral-directional characteristics of this model are interesting, particularly in that the results offer the opportunity to study the aerodynamic influence of the fuselage upon the stabilizing effectiveness of the tail. A three-view drawing of this model is shown in figure 12 and further details concerning its geometric characteristics are presented in table I.

The coefficients C_c, C_l, and C_n vs. β are presented in figure 13 while figure 14 shows C_n vs. β, on a larger scale, for the basic model at angles of attack of 0° and 10°. Figure 15 presents the variation of C_l/β, C_c/β, and C_n/β with α for the basic model with various modifications. Photographs showing the flow pattern behind the wing-body model are shown in figure 16. Figure 17 presents the variation of the lateral-directional stability characteristics with Mach number at angles of attack of 0° and 10° for the model with several vertical-tail arrangements. From an examination of the data presented in figures 15 and 17, it is evident that the directional stability of Model D decreased markedly with increasing angle of attack and Mach number, especially at supersonic speeds. Moreover, the yawing moment of the model (fig. 13) varies nonlinearly with sideslip angle because of the nonlinear variation of vertical-tail load with sideslip (cf. figs. 13(a) and 13(b)). A more detailed examination of this nonlinearity is presented in figure 14, wherein the variation of the yawing moment with sideslip angle is shown at two angles of attack and several Mach numbers.

The decrease in directional stability with Mach number shown in figure 17 is about as expected, from consideration of the effect of Mach number upon the vertical-tail effectiveness. Notice, however, that the large destabilizing body contribution remains constant with Mach number while that of the vertical fin decreases so that the model has almost neutral directional stability at a Mach number of 1.9. That addition of the wing has very little effect upon this unstable body contribution can be seen by comparing the results for the body alone with those of the wing-body combination (see figs. 15(g) and 15(b)).

Investigation of the effect of angle of attack upon the lateral-directional characteristics revealed a further serious effect of the long fuselage. The deterioration of directional stability with increasing angle of attack (fig. 15) was found to be related in part to the fact that the effectiveness of the vertical tail is influenced by vorticity associated with the lifting fuselage. A qualitative study of this problem was made by examining the induced flow field in the tail region of Model D in conditions of combined angle of attack and sideslip with the vapor-screen flow-visualization technique described in detail in reference 2. Some typical vapor-screen photographs obtained in these tests are shown in figure 16. The point from which these photographs were taken was located inside the wind tunnel directly downstream from the model. The thin plane of intense light was projecting across the wind tunnel from the left; consequently, a shadow of the model was cast to the right. The dark circular spots on the vapor screen are caused by regions of concentrated vorticity shed from lifting elements of the model forward of the vapor screen. The spinning action of the vortices forces moisture particles outward from their centers of rotation. Innermost areas of the vortices, therefore, are devoid of particles capable of reflecting light and hence these vortex regions appear as dark spots on the vapor screen.

[redacted]

In figure 16(a) the dark spot at the left is caused by the wing-tip vortex shed from the left wing of the model. The corresponding vortex from the right wing is obscured somewhat by the shadow cast by the fuselage. In addition to these vortices, two more vortices originating from the fuselage are shown to be located in close proximity to the positions normally occupied by the tail of the model. Note that at 12° angle of attack the intensity of all of the vortices increases (see fig. 16(b)) as is indicated by an increase in the size of the dark spots. Also, at 12° angle of attack another vortex appears at a point approximately midway between the fuselage and the right wing-tip vortex. This vortex is believed to form as a result of flow separation associated with the leading edge of a sweptback wing. Because of the proximity of the fuselage vortices to the tail position, particularly the vertical tail, it is believed that they have a large effect upon the directional stability of the model at angle of attack. Similarly, the directional stability probably is influenced to a lesser degree (in the angle ranges tested) by the induced effects of the wing-tip and separation vortices because of their remote location relative to the tail. From physical considerations in conjunction with a study of the location and direction of rotation, particularly of the upper fuselage vortex, it is believed that the dorsal fairing and the lower portions of the vertical tail are in regions of adverse sidewash when the model is at combined angle-of-attack and -sideslip conditions.

Forward movement of the vapor screen to the midpoint of the body in figure 16(c) shows that at this position the center of rotation of one of the fuselage vortices is under the left wing and that of the other is above the fuselage. It is probable that the effect of Mach number in the supersonic range has little influence upon the induced flow patterns shown in figure 16 (ref. 2).

An estimate of the magnitude of the induced effect of the fuselage upon the vertical-tail effectiveness can be obtained by comparing directional stability of the body alone in figure 15(g) with that of the body-tail combination (fig. 15(f)). Note that at about 14° angle of attack the vertical tail has lost its effectiveness almost entirely, despite the fact that the area of the vertical tail is about 30 percent of the wing area. By comparing the directional stability of the body-tail combination with that of the complete model, it is evident that some improvement in directional stability occurs as a result of the addition of the wing. This result probably is caused by the wing downwash restricting to some extent the vertical movement with angle of attack of the fuselage vortex which passes near the vertical tail and by a decrease in the strength of the fuselage vortices. Tests of the model with vertical tails of higher aspect ratio and with lesser sweepback angle, figures 15(c) and 15(d), show only slight improvement in the directional characteristics, except at a Mach number of 1.9 where a small loss is shown. This decrease in directional stability occasioned by these vertical-tail modifications is believed to be the result of a loss of dynamic pressure when the

[redacted]

vertical tail was extended upward or forward since the shock waves emanating from the trailing edge of the wing at a Mach number of 1.9 cross the vertical tail in the region of the tip.

As noted in the "Procedure" section of this report, the lateral-directional data presented as functions of angle of attack have not been adjusted for the effects of air-stream irregularities. Hence, the level of the data may be slightly in error although the variation with angle of attack is believed to be correct.

The influence of horizontal-tail and vertical-tail interference on the lateral-directional characteristics of Model D, especially at higher angles of attack, was cursorily investigated in tests with the horizontal tail mounted at the tip of the vertical tail. A comparison of the characteristics of the model with an unswept vertical tail with the horizontal tail mounted low on the fuselage and on the tip of the vertical tail is shown in figures 15(d) and 15(e). The end-plate effect of the horizontal tail, when mounted at the tip of the vertical tail, is evident in these figures by the increased cross-wind-force and yawing-moment parameters at an angle of attack of 0°. A more significant effect of the high tail on the characteristics of this model is the improvement in the variation of directional stability with increasing angle of attack. This is the result of horizontal- and vertical-tail interference and so varies with horizontal-tail loads. Both the end-plate and interference effects of the high horizontal-tail position contribute a positive dihedral effect. Since the end-plate and interference effects of the horizontal tail exist only within the Mach cone of the horizontal tail, the gains in the directional characteristics of the model diminish with increasing Mach number.

Model E

The effect of horizontal-tail position on the longitudinal characteristics of aircraft has received considerable attention. Results for Model E (see fig. 18 for dimensional sketch) permits a study of the influence of a high horizontal-tail location on the lateral-directional stability characteristics. Figures 19(c) and 19(h) present yawing-moment, rolling-moment, and cross-wind-force coefficients as functions of sideslip angle for the model with and without the horizontal tail. A comparison of these two figures shows that the addition of the horizontal tail high on the vertical fin significantly increases the lateral-directional stability of the model, particularly at subsonic speeds. However, as the Mach number is changed from 0.9 to 1.45 and then to 1.9 the lateral-directional stabilizing contribution of the horizontal tail decreases. At supersonic speeds the area of the tail surfaces subject to the favorable mutual interference is confined to the area within the Mach cones of the horizontal and vertical tails. Therefore, as the Mach number is increased the interference decreases.

Results are presented which illustrate the effect of a dihedral angle change of from -5° to -10° on the lateral-directional stability characteristics of the complete model (figs. 19(a) and 19(c)) and the wing-body arrangement (figs. 19(b) and 19(d)). Also shown is a comparison of two tail arrangements on the model (figs. 19(c) and 19(f)). The model with the lowered horizontal tail (fig. 19(f)) shows a decrease in directional stability which is slightly greater than would be expected due to the decrease in vertical-tail area. The dihedral effect resulting from lowering the horizontal tail was equivalent to a -5° change in wing dihedral angle at a Mach number of 0.9 and decreased with speed to about -1° at a Mach number of 1.9.

In order to investigate the lateral-directional stability characteristics of the model with air entering the side inlets, another model was constructed which incorporated certain modifications to allow for internal air flow. Comparison of the lateral-directional characteristics of the model with an internal mass-flow ratio of 0.8 (fig. 19(j)) and with the inlets faired closed (fig. 19(i)) showed a slight decrease in directional stability for the case of internal air flow. This effect was apparently the result of the additional side loads carried by the inlets. This comparison was made with the rear duct fairing in place. The effect of the rear duct fairing on the aerodynamic characteristics of the model are shown by a comparison of figures 19(i) and 19(k). Side loads on the rear duct fairing contribute a stable restoring moment to the model.

The effect of angle of attack on the lateral-directional stability parameters of Model E with internal air flow is presented in figure 20. Results obtained at Mach numbers of 0.9 and 1.45 show a progressive increase in directional stability with angle of attack up to angles of 7° or 8°. This type of variation with angle of attack results from the horizontal-tail-vertical-tail interference, and appears to be a characteristic effect of the high-mounted horizontal tail. Similar variations of the lateral-directional stability parameters with angle of attack are shown in the data for Model D with the high-mounted horizontal tail. The decrease in directional stability with increasing angle of attack at a Mach number of 1.9 may be due to a combination of the decrease in end-plate effect at higher Mach numbers, and to the loss of vertical-tail effectiveness resulting from the air expansion over the wing. The latter phenomenon was observed to affect the directional characteristics of Models A, B, and D at those Mach numbers where portions of the vertical tail were ahead of the shock wave emanating from the trailing edge of the wing.

[redacted]

CONCLUDING REMARKS

Examination of the aerodynamic parameters for several models investigated show the following aerodynamic phenomena to be important in the determination of model characteristics:

1. The vorticity shed from the body may play a predominant part in the variation of directional stability with angle of attack at all Mach numbers for airplanes having a long slender body. In particular, the vorticity due to the side load on the body appears to be important in this respect.

2. The flow field generated by the upper surface of the wing, within which the air density is reduced, can influence the variation of directional stability with angle of attack. This effect was shown in these data as a decrease in directional stability with increasing angle of attack for those models with the vertical tail mounted close above the wing. This condition tends to become more severe as the Mach number increases.

3. The effect of the impingement of pressure disturbances from other portions of the airplane on the vertical surface appears important in determining directional stability and is a factor to be considered, particularly for airplanes with nacelles or external stores. It is found that use may be made of the shielding effect of the wing to improve this condition.

4. Large favorable end-plate effects of horizontal tails are found at transonic speeds but these favorable effects disappear at higher supersonic Mach numbers since the Mach cone of the horizontal tail does not envelope a sizable portion of the vertical tail.

Ames Aeronautical Laboratory
National Advisory Committee for Aeronautics
Moffett Field, Calif., Oct. 3, 1955

REFERENCES

1. Frick, Charles W., and Olson, Robert N.: Flow Studies in the Asymmetric Adjustable Nozzle of the Ames 6- by 6-Foot Supersonic Wind Tunnel. NACA RM A9E24, 1949.

[redacted]

2. Spahr, Richard J., and Dickey, Robert R.: Wind-Tunnel Investigation of the Vortex Wake and Downwash Field Behind Triangular Wings and Wing-Body Combinations at Supersonic Speeds. NACA RM A53D10, 1953.

3. Christensen, Frederik B.: An Experimental Investigation of Four Triangular-Wing-Body Combinations in Sideslip at Mach Numbers 0.6, 0.9, 1.4, and 1.7. NACA RM A53L22, 1954.

4. Jones, Arthur L., Spreiter, John R., and Alksne, Alberta: The Rolling Moment Due to Sideslip of Triangular, Trapezoidal, and Related Plan Forms in Supersonic Flow. NACA TN 1700, 1948.

5. Anderson, Adrien E.: An Investigation at Low Speed of a Large-Scale Triangular Wing of Aspect Ratio Two. - II. The Effect of Airfoil Section Modifications and the Determination of the Wake Downwash. NACA RM A7H28, 1947.

6. Jaquet, Byron M., and Brewer, Jack D.: Effects of Various Outboard and Central Fins on Low-Speed Static-Stability and Rolling Characteristics of a Triangular-Wing Model. NACA RM L9E18, 1949.

[redacted]

TABLE I.- PRIMARY GEOMETRIC CHARACTERISTICS OF THE WIND-TUNNEL MODELS

	Model A	Model B	Model C	Model D	Model E
Wing					
Plan form	Modified triangular	Modified triangular	Triangular	Sweptback	Unswept
Aspect ratio	2.1	2.02	3.0	3.4	2.5
Mean aerodynamic chord, $\bar{c}$, ft	2.13	1.278	1.207	0.495	0.799
Moment center, $\bar{c}$	0.25	0.25	0.35	0.287	0.25
Span, ft	3.343	2.34	2.699	1.493	1.89
Area, sq ft	5.338	2.728	2.425	0.662	1.406
Thickness ratio, percent chord	4.08	5 at root 3.2 at tip	3	6 at root 5 at tip	3.4
Camber	(1)	0	0	0	0 and leading-edge flap $\delta = -3^{\circ}$
Taper ratio	0	0.332	0	0.25	0.385
Sweepback of leading edge, deg	60	52.5	53.1	47.2	27.1
Dihedral, deg	0	0	0	-5	-5 & -10
Incidence, deg	3	0	0	0	0
[2]Vertical tail					
Area, sq ft	0.712	0.468	0.4188(total)	0.1758	0.421
Leading-edge sweep, deg	50	52.5	53	50.5	38
Length, percent $\bar{c}$	84.5	50.6	67.1	122.4	138.0
Span, ft	1.073	0.878	0.60	0.507	0.729
Aspect ratio	1.59	1.46	1.72	1.5	1.26
Body length, ft	5.14	3.278	3.910	2.121	3.783

Geometric characteristics of the alternate vertical tails of Models D and E

Characteristic	Model D				Model E	
	Basic vertical tail	Large area vertical tail	Unswept vertical tail	Tall vertical tail	Basic vertical tail	Small vertical tail
[2]Vertical tail						
Area, sq ft	0.1758	0.1958	0.1816	0.1805	0.421	0.413
Leading-edge sweep, deg	50.5	47.13	12.5	50.4	38	44
Length, percent $\bar{c}$	122.4	121.2	115.3	124.0	138.0	135.7
Span, ft	0.507	0.528	0.519	0.545	0.729	0.665
Aspect ratio	1.46	1.42	1.48	1.64	1.26	1.07

[1]Wing incorporates conical camber with the leading edge offset 0.0286 b/2. The camber line becomes tangent to the chord plane at 0.85 b/2.

[2]Area of the vertical tail obtained by extending the leading and trailing edges to the fuselage reference line.

[redacted]

TABLE II.- STREAM-IRREGULARITY CORRECTIONS

[These corrections apply only to the plots with β as the primary variable. They are to be added to the results for the complete model. Corrections to the results for the tail-off configurations are zero except for C_{l_β} where they are the same as for the complete model.]

Model	Mach number	Correction		
		C_{n_β}	C_{c_β}	C_{l_β}
A	1.50	0.0001	0.0001	0
	1.60	.0002	.0001	-.0001
	1.75	.0002	0	-.0002
	1.90	.0002	0	.0001
B	1.25	-.0002	-.0002	.0002
	1.40	-.0002	0	-.0001
	1.65	.0002	0	-.0001
	1.90	.0003	.0004	-.0003
D	1.20	-.0001	0	0
	1.40	-.0001	.0002	-.0001
	1.60	.0001	.0002	-.0001
	1.90	.0002	.0005	-.0001
E	1.45	-.0001	-.0002	.0001
	1.90	.0002	.0005	-.0001

[redacted]

TABLE III.- INDEX OF FIGURES

Figure number	Model	Subject material	α, deg	β, deg	Mach number
1		General arrangement of the five models			
2(a)	A	Dimensional sketch			
2(b)		Detail of basic nacelles			
2(c)		Detail of Siamese nacelles			
		C_c, C_l, and C_n vs. β			
3(a)		Basic model	3	-4 to 9	1.60, 1.75, 1.90
3(b)		Less vertical tail	3	-4 to 9	1.60, 1.75, 1.90
3(c)		Wing-chord-plane-mounted outboard nacelles	3	-4 to 9	0.90, 1.50, 1.60, 1.75, 1.90
3(d)		Wing-chord-plane-mounted outboard nacelles	8	-4 to 9	0.90, 1.60, 1.75, 1.90
3(e)		Less vertical tail	3	-4 to 9	0.90, 1.60, 1.75, 1.90
3(f)		Pitched down 5° about their bases	3	-4 to 9	1.50, 1.60, 1.75, 1.90
3(g)		Toed in 5°	3	-4 to 9	1.50, 1.60, 1.75, 1.90
3(h)		With outboard port nacelles plugged	3	-4 to 9	1.50, 1.60, 1.75, 1.90
3(i)		Less nacelles	3	-4 to 9	1.60, 1.90
3(j)		With Siamese nacelles	3	-4 to 9	0.90, 1.60, 1.75, 1.90
3(k)		With Siamese nacelles	8	-4 to 9	1.60, 1.90
3(l)		Less vertical tail	3	-4 to 9	1.60, 1.90
3(m)		Inboard nacelles moved forward; outboard nacelles pitched up 5° and moved forward and inward	3	-4 to 9	1.50, 1.60, 1.75, 1.90
3(n)		Inboard nacelles moved forward; outboard nacelles moved forward, inward, and downward	3	-4 to 9	1.50, 1.60, 1.75, 1.90
3(o)		Inboard nacelles moved forward; outboard nacelles moved forward, inward, and downward	7	-4 to 9	1.50, 1.60, 1.75, 1.90
3(p)		Less vertical tail	3	-4 to 9	1.50, 1.60, 1.75, 1.90
3(q)		Outboard port nacelle plugged	3	-4 to 9	1.50, 1.60, 1.75, 1.90
3(r)		Outboard nacelles pitched up 5°	3	-4 to 9	1.50, 1.60, 1.75, 1.90
3(s)		Outboard nacelles pitched up 5° and moved forward and inward	3	-4 to 9	0.90, 1.50, 1.60, 1.75, 1.90
3(t)		Inboard nacelles moved forward and upward; outboard nacelles pitched up 5° and moved forward, inward, and downward	3	-4 to 9	0.90, 1.60, 1.75, 1.90
		$\frac{C_l}{\beta}$, $\frac{C_c}{\beta}$, and $\frac{C_n}{\beta}$ vs. α			
4		With Siamese nacelles	-5 to 9	±5	1.60, 1.90
		C_{l_β}, C_{c_β}, and C_{n_β} vs. M			
5(a)		Complete model, less vertical tail, and less nacelles	3	0	1.60 to 1.90
5(b)		With wing-chord-plane-mounted nacelles, pitched down 5°, and toed in 5°	3	0	1.50 to 1.90
5(c)		With basic inboard nacelles, with inboard nacelles forward	3	0	1.50 to 1.90
5(d)		With wing-chord-plane-mounted nacelles at two angles of attack	3 and 8	0	0.90 and 1.50 to 1.90
5(e)		With outboard nacelles moved downward, forward, and inward at two angles of attack	3 and 7	0	1.50 to 1.90
5(f)		With Siamese nacelles at two angles of attack	3 and 8	0	0.90 and 1.60 to 1.90
6	B	Dimensional sketch			
		C_c, C_l, and C_n vs. β			
7(a)		Basic Model	0	-5 to 5	0.90, 1.25, 1.40, 1.65, 1.90
7(b)		Less vertical tail	0	-5 to 5	1.25, 1.40, 1.65
7(c)		Basic Model	5	-5 to 5	0.90, 1.25, 1.40, 1.65, 1.90
7(d)		Less vertical tail	5	-5 to 5	1.25, 1.40, 1.65
		$\frac{C_l}{\beta}$, $\frac{C_c}{\beta}$, and $\frac{C_n}{\beta}$ vs. α			
8(a)		Basic Model	-4 to 10	±5	0.90, 1.25, 1.40, 1.65, 1.90
8(b)		Less vertical tail	-4 to 8	±5	1.25, 1.40, 1.65
		C_{l_β}, C_{c_β}, and C_{n_β} vs. M			
9(a)		Basic Model With and without the vertical tail	0	0	0.70 to 0.90, 1.25 to 1.90
9(b)		With and without the vertical tail	5	0	0.70 to 0.90, 1.25 to 1.90

TABLE III.- INDEX OF FIGURES - Concluded

Figure number	Model	Subject material	α, deg	β, deg	Mach number
10	C	Dimensional sketch			
		C_c, C_l, and C_n vs. β			
11(a)		Basic Model	0	-6 to 8	0.60, 0.90, 1.40
11(b)		Basic Model	5	-6 to 8	0.60, 0.90, 1.40
11(c)		Basic Model	10	-6 to 8	0.60, 0.90
12	D	Dimensional sketch			
		C_c, C_l, and C_n vs. β			
13(a)		Basic Model	0	-4 to 10	0.90, 1.20, 1.40, 1.60, 1.90
13(b)		Less vertical and horizontal tail	0	-4 to 10	0.90, 1.20, 1.40, 1.60, 1.90
13(c)		With large-area vertical tail	0	-4 to 10	0.90, 1.20, 1.40, 1.60, 1.90
13(d)		With unswept vertical tail	0	-4 to 10	0.90, 1.20, 1.40, 1.60, 1.90
13(e)		Basic Model	10	-4 to 10	0.90, 1.20, 1.40, 1.60, 1.90
13(f)		Less vertical and horizontal tail	10	-4 to 10	0.90, 1.20, 1.40, 1.60, 1.90
		C_n vs. β			
14(a)		Basic Model	0 and 10	-4 to 10	0.90
14(b)		Basic Model	0 and 10	-4 to 10	1.20
14(c)		Basic Model	0 and 10	-4 to 10	1.40
14(d)		Basic Model	0 and 10	-4 to 10	1.60
14(e)		Basic Model	0 and 10	-4 to 10	1.90
		$\frac{C_l}{\beta}$, $\frac{C_c}{\beta}$, and $\frac{C_n}{\beta}$ vs. α			
15(a)		Basic Model	-4 to 18	±5	0.90, 1.20, 1.40, 1.60, 1.90
15(b)		Less vertical and horizontal tail	-4 to 18	±5	0.90, 1.20, 1.40, 1.60, 1.90
15(c)		With tall vertical tail	-4 to 18	±5	0.90, 1.20, 1.40, 1.60, 1.90
15(d)		With unswept vertical tail	-4 to 18	±5	0.90, 1.20, 1.40, 1.60, 1.90
15(e)		With high horizontal tail	-4 to 18	±5	0.90, 1.20, 1.40, 1.60, 1.90
15(f)		Less wing	-4 to 18	±5	0.90, 1.20, 1.40, 1.60, 1.90
15(g)		Less vertical and horizontal tail	-4 to 18	±5	0.90, 1.20, 1.40, 1.60, 1.90
		Vapor-Screen Study			
		Less vertical and horizontal tail model			
16(a)		Vapor screen at tail position	6	5	1.90
16(b)		Vapor screen at tail position	12	5	1.90
16(c)		Vapor screen at mid-fuselage	12	5	1.90
		C_{l_β}, C_{c_β}, and C_{n_β} vs. M			
17(a)		With basic vertical tail, large vertical tail, unswept vertical tail, and less vertical and horizontal tail	0	0	0.60 to 0.90 and 1.20 to 1.90
17(b)		With basic vertical tail, and less vertical and horizontal tail	10	0	0.60 to 0.90 and 1.20 to 1.90
18	E	Dimensional sketch			
		C_c, C_l, and C_n vs. β			
19(a)		Basic Model	0	-5 to 5	0.90, 1.45, 1.90
19(b)		Less vertical and horizontal tail	0	-5 to 5	0.90, 1.45, 1.90
19(c)		With 10° negative dihedral wing	0	-5 to 5	0.90, 1.45, 1.90
19(d)		Less vertical and horizontal tail	0	-5 to 5	0.90, 1.45, 1.90
19(e)		Less vertical and horizontal tail	5	-5 to 5	0.90, 1.45, 1.90
19(f)		With small vertical tail	0	-5 to 5	0.90, 1.45, 1.90
19(g)		With small vertical tail	5	-5 to 5	0.90, 1.45, 1.90
19(h)		Less horizontal tail	0	-5 to 5	0.90, 1.45, 1.90
19(i)		With rear duct fairing and -3° wing leading-edge flap deflection, $m/m_\infty = 0$	0	-5 to 5	0.90, 1.45, 1.90
19(j)		With internal air flow of $m/m_\infty = 0.8$	0	-5 to 5	0.90, 1.45, 1.90
19(k)		Less rear duct fairing, $m/m_\infty = 0$	0	-5 to 5	0.90, 1.45, 1.90
		$\frac{C_l}{\beta}$, $\frac{C_c}{\beta}$, and $\frac{C_n}{\beta}$ vs. α			
20		With 10° negative dihedral wing, small vertical tail, -3° wing leading-edge flap deflection; $m/m_\infty = 0.8$	-3 to 15	0 and 5	0.90, 1.45, 1.90

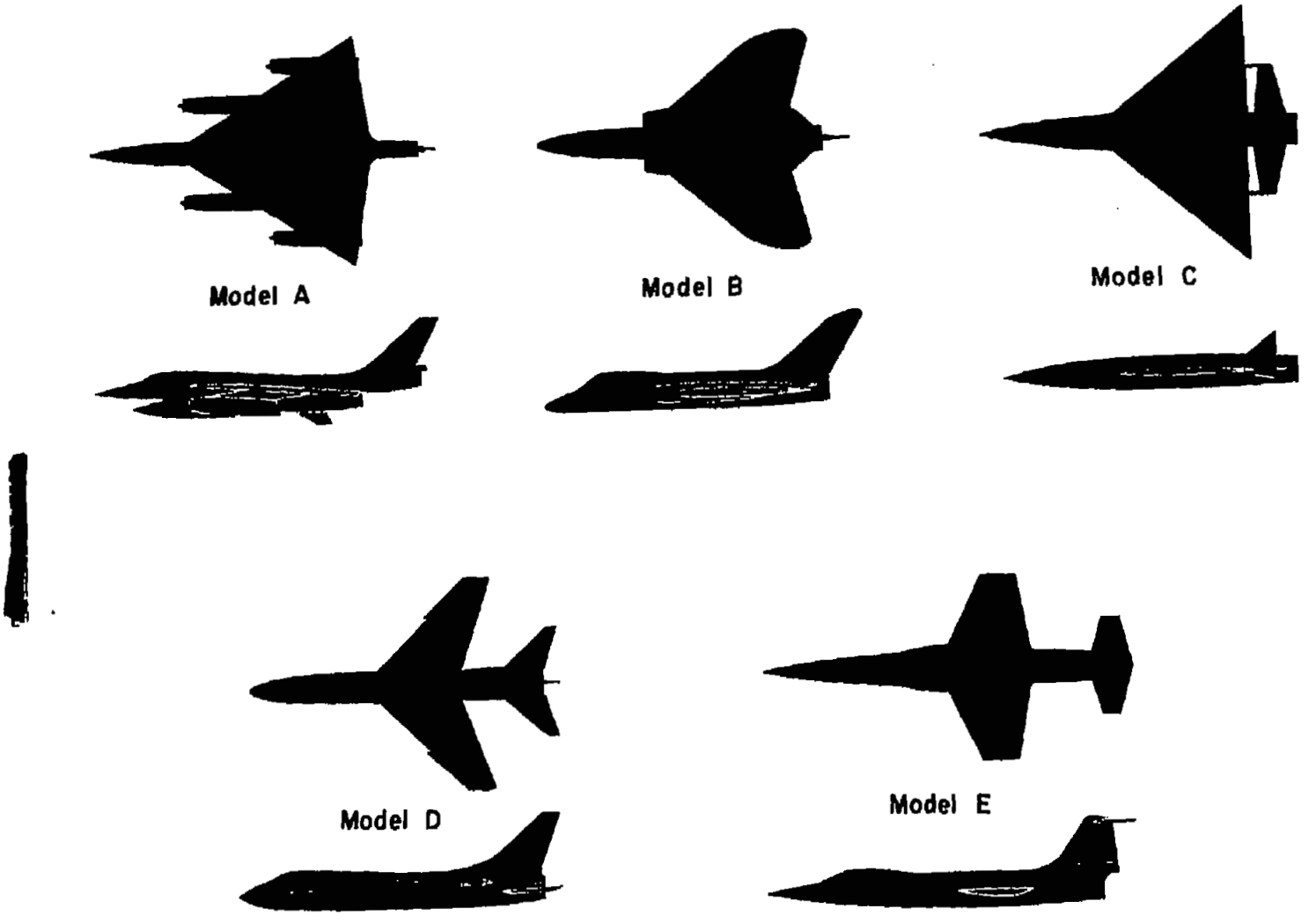

Figure 1.- General arrangement of the five models.

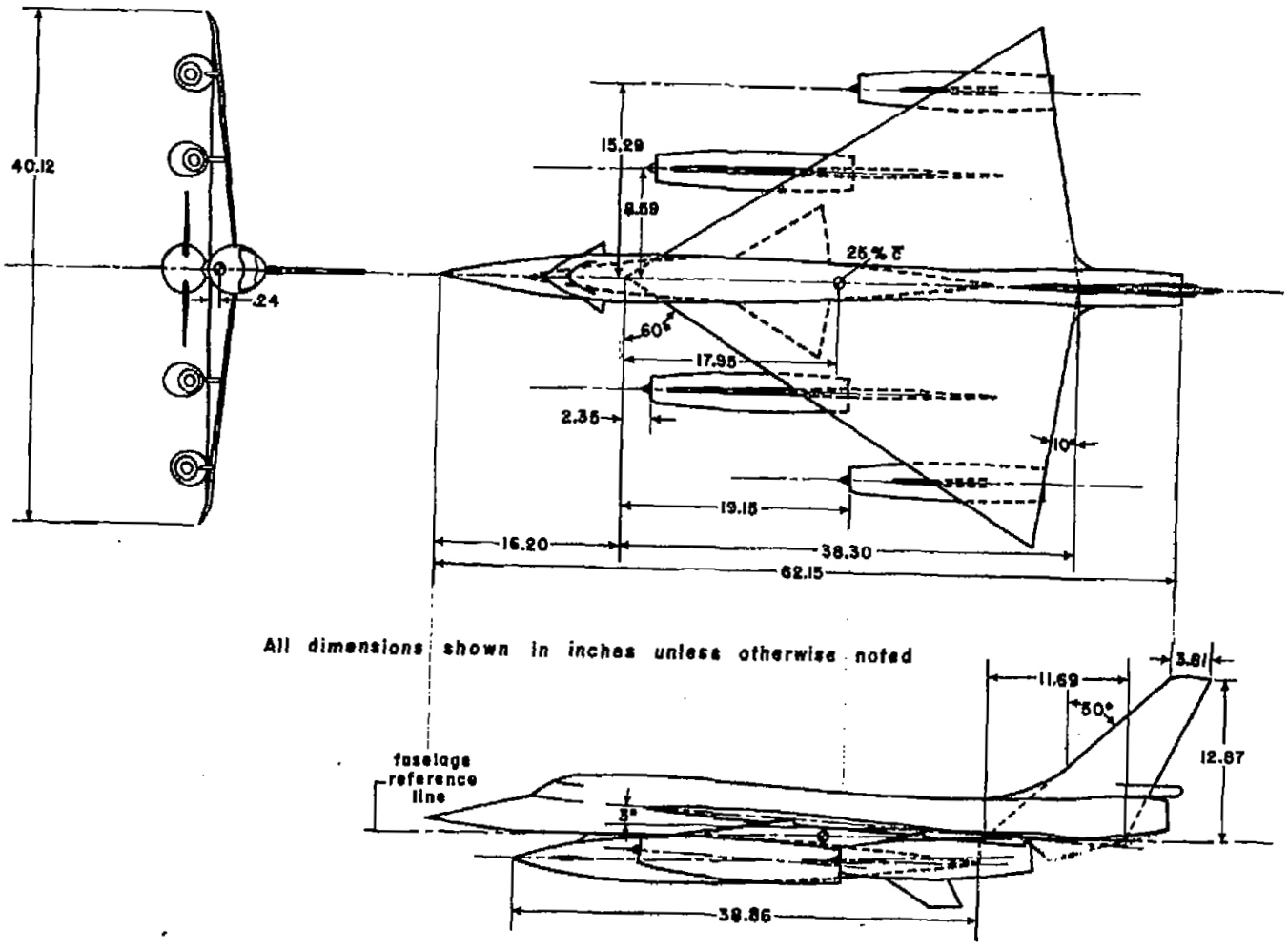

(a). Basic model.

Figure 2.- Dimensional sketch of Model A.

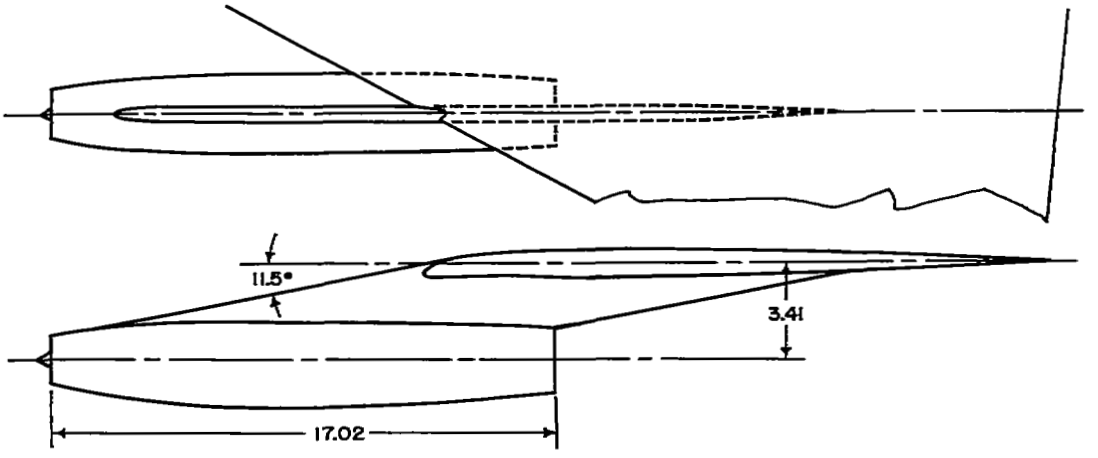

Inboard nacelle

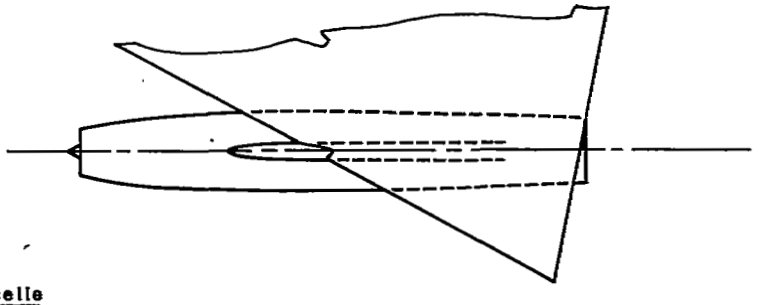

Outboard nacelle

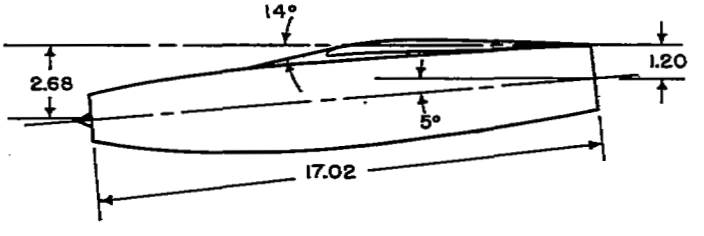

(b) Detail of basic nacelles.

Figure 2.- Continued.

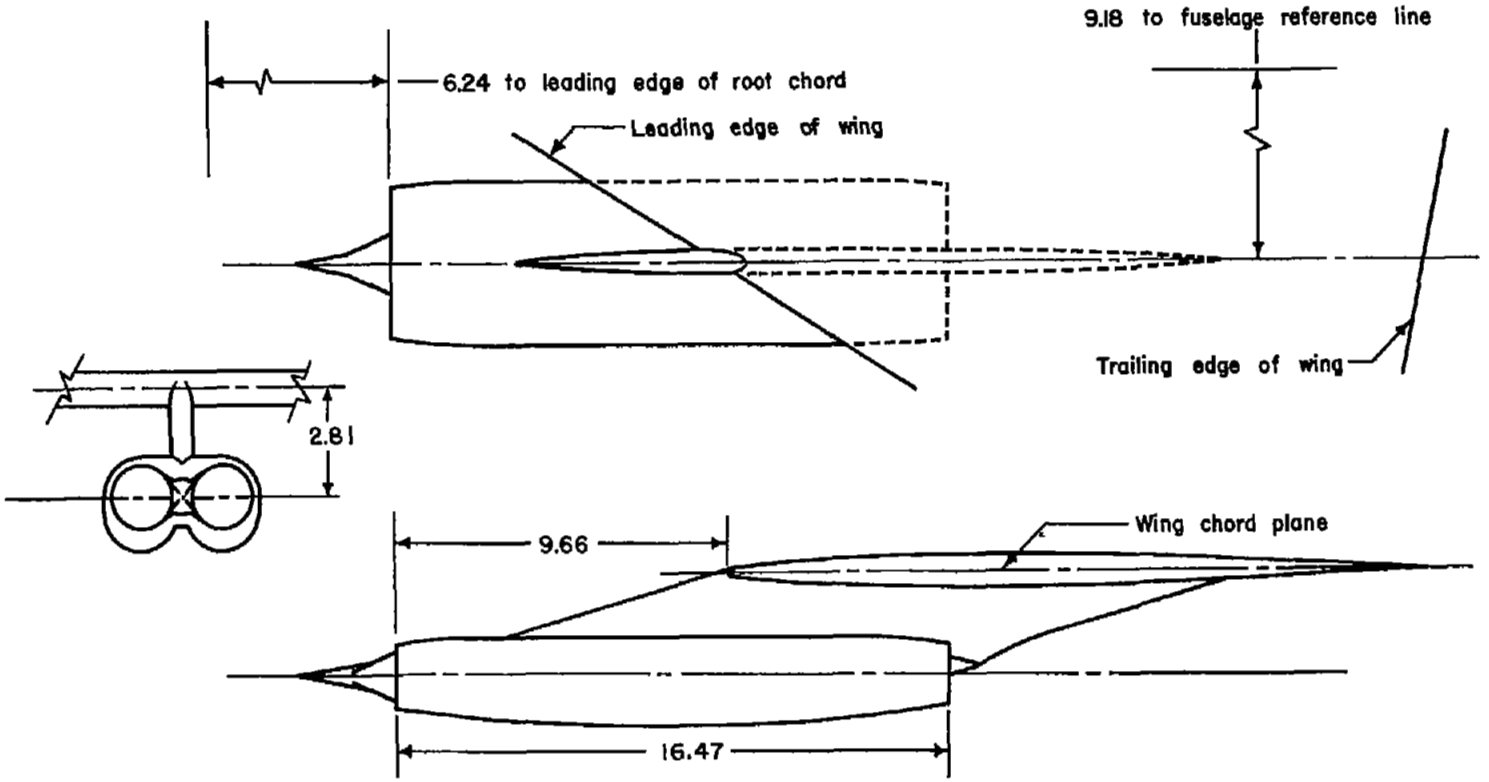

(c) Detail of Siamese nacelles.

Figure 2.- Concluded.

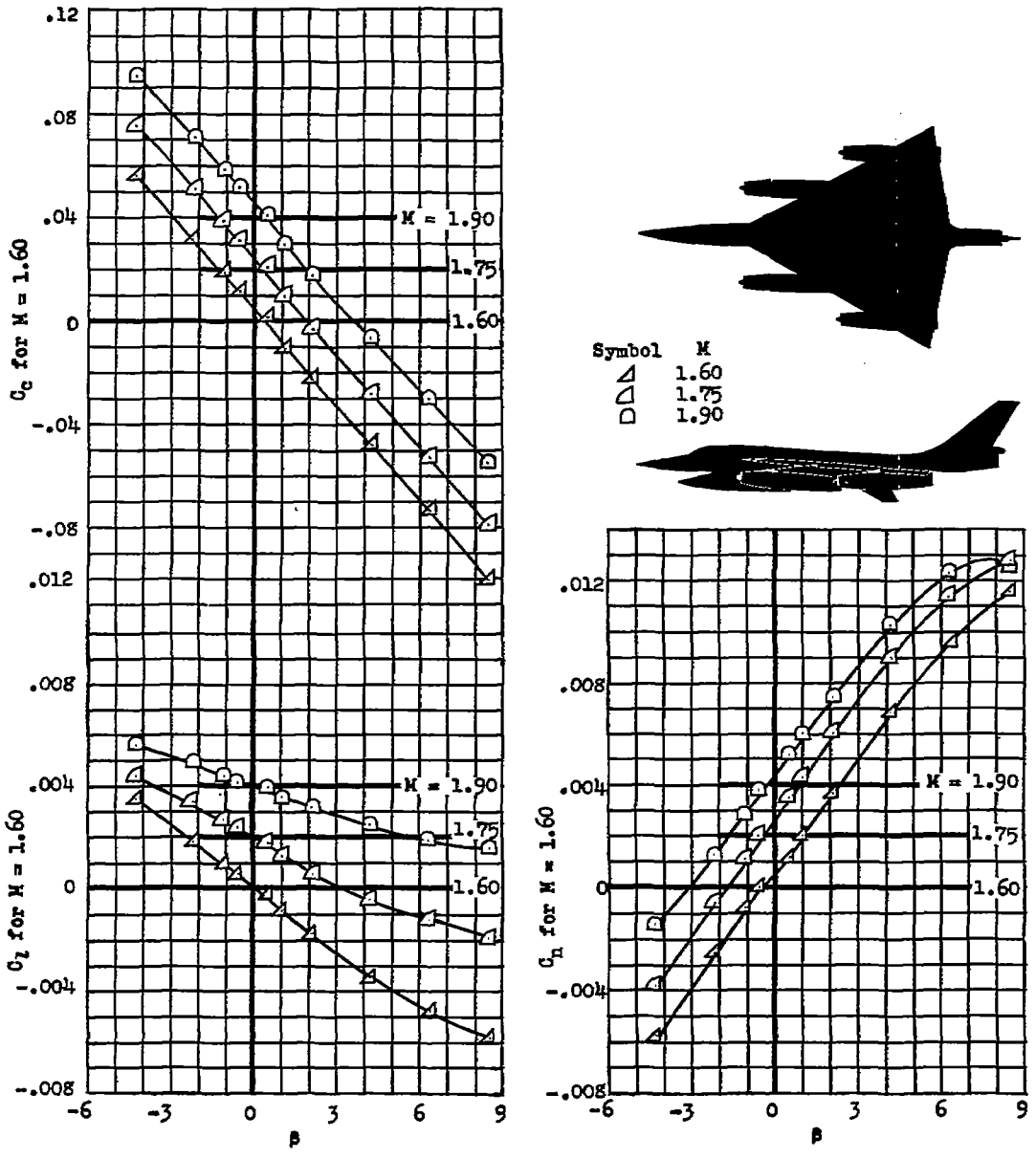

(a) Basic model; $\alpha = 3^{\circ}$.

Figure 3.- Variation of lateral-directional stability characteristics with angle of sideslip for Model A with various modifications.

[redacted]

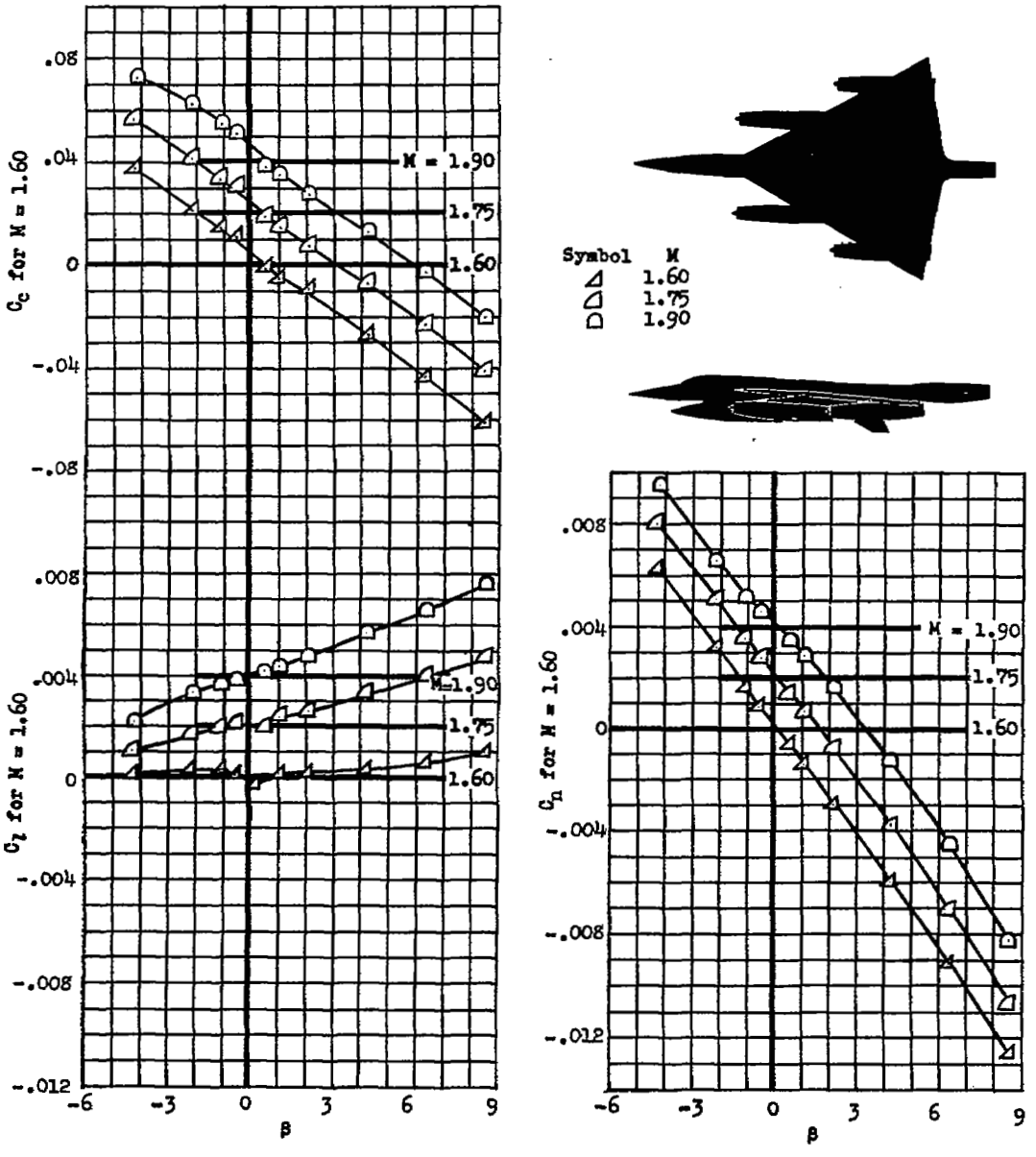

(b) Model without vertical tail; $\alpha = 3^{\circ}$.

Figure 3.- Continued.

[redacted]

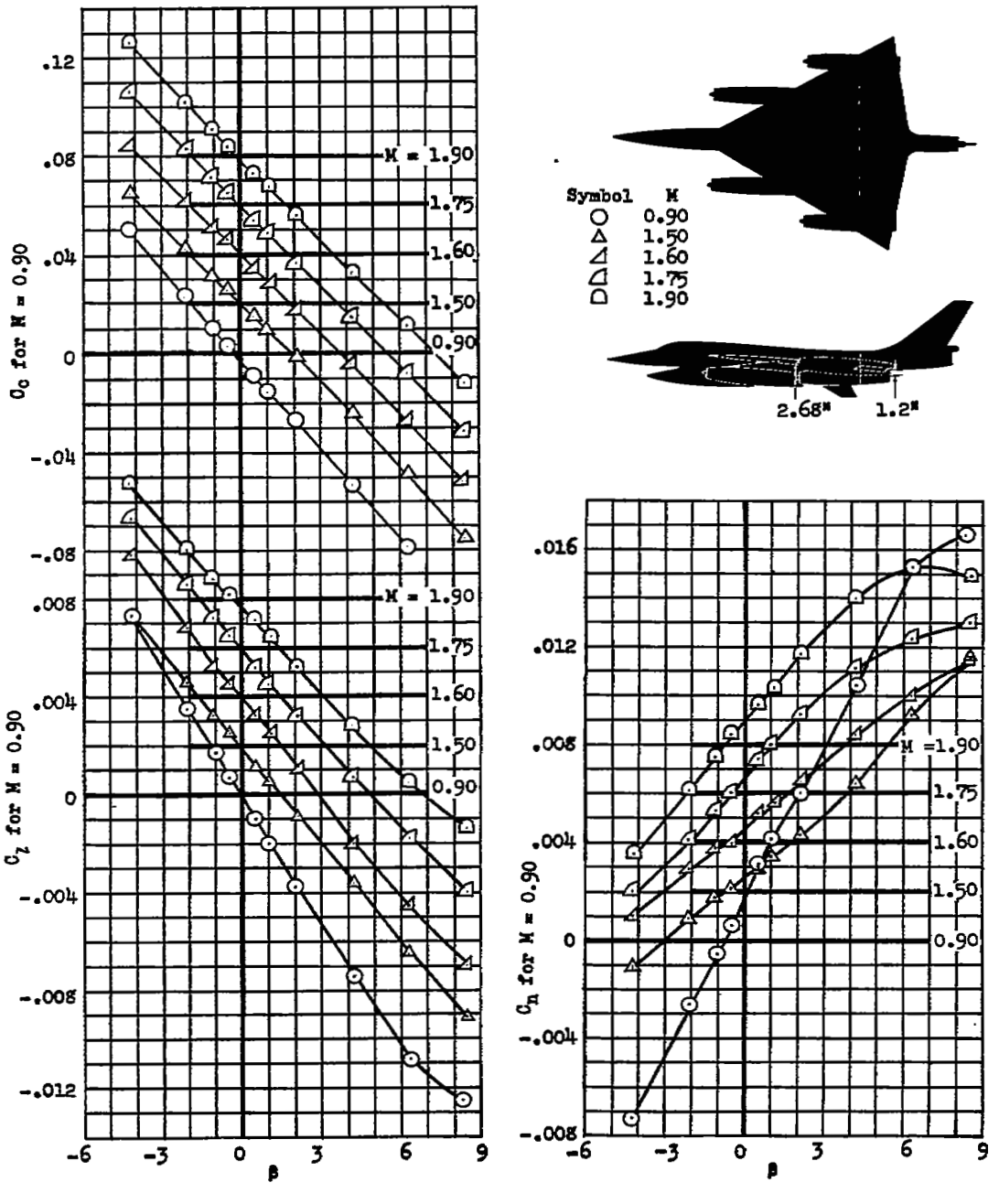

(c) Outboard nacelles mounted with their center lines in the chord plane of the wing; $\alpha = 3^{\circ}$.

Figure 3.- Continued.

[redacted]

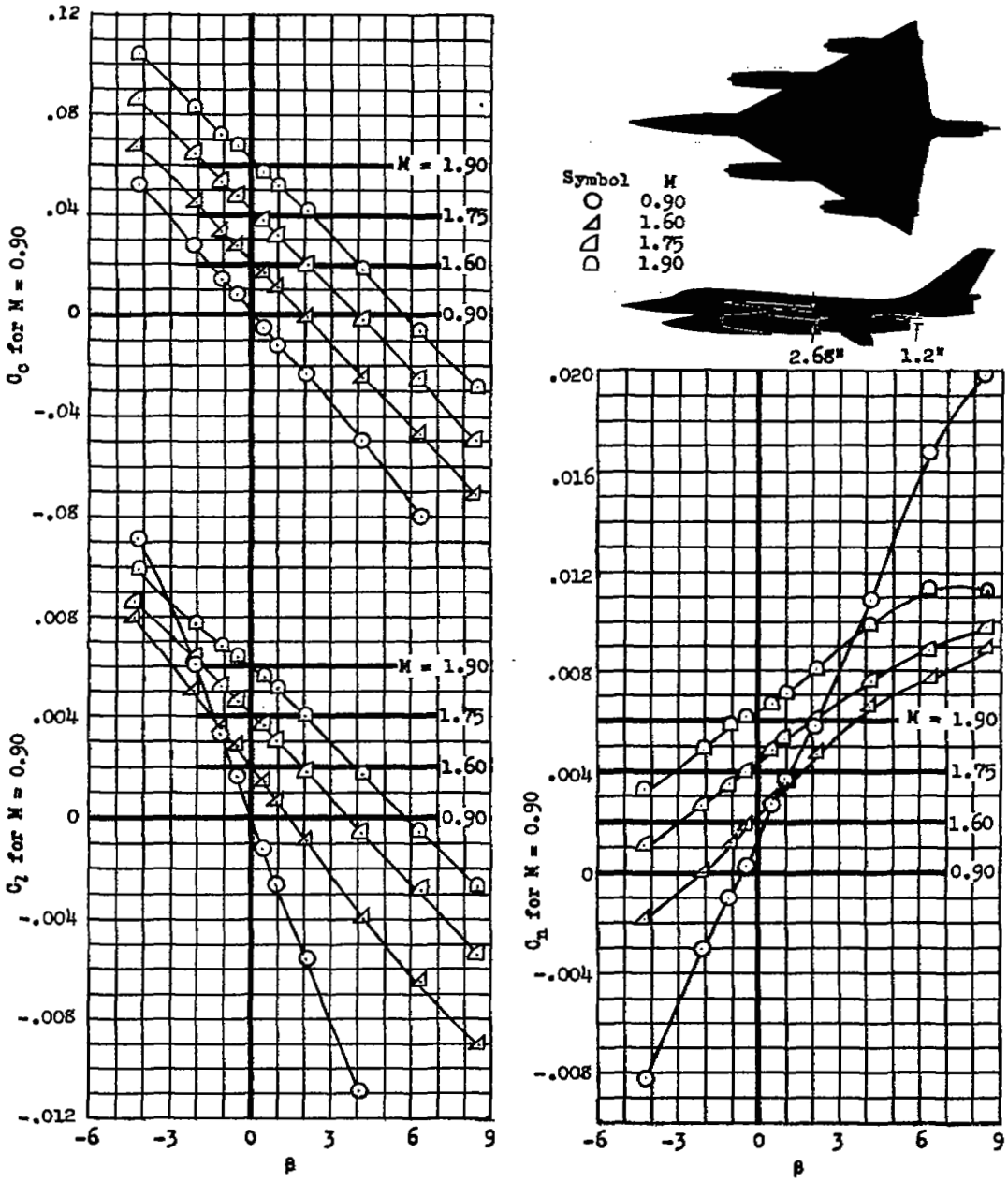

(d) Outboard nacelles mounted with their center lines in the chord plane of the wing; $\alpha = 8^{\circ}$.

Figure 3.- Continued.

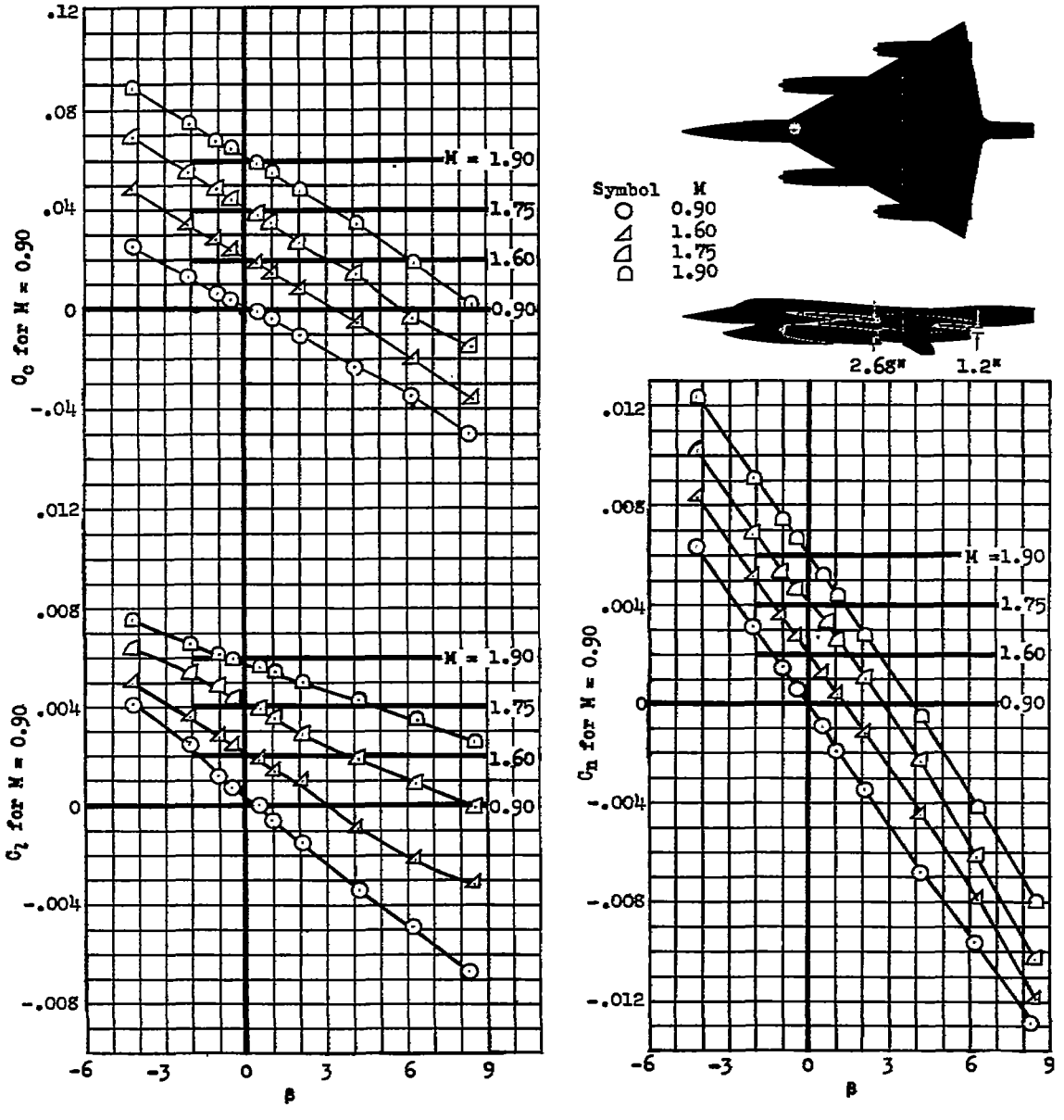

(e) Outboard nacelles mounted with their center lines in the chord plane of the wing; without vertical tail; $\alpha = 3^{\circ}$.

Figure 3.- Continued.

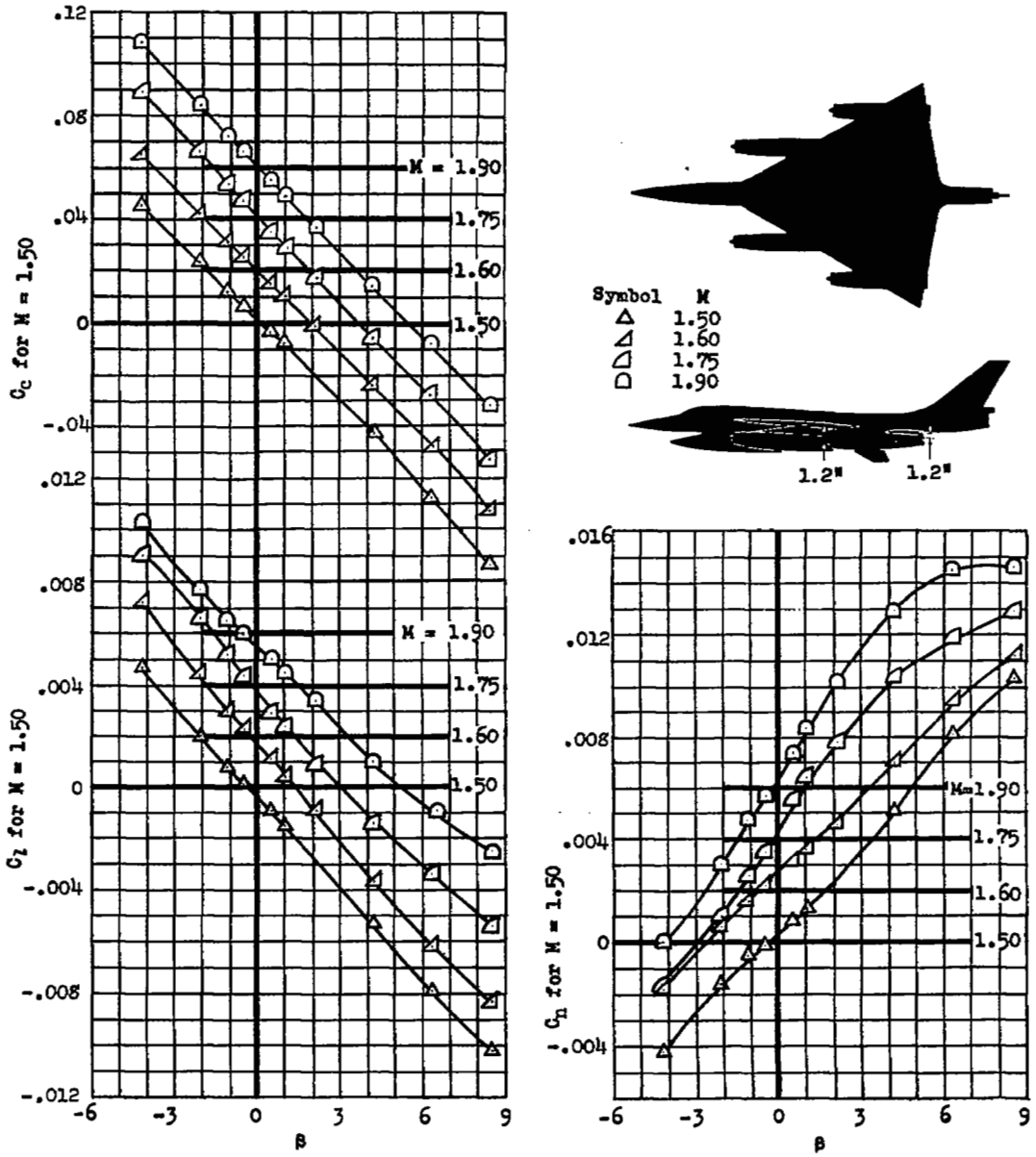

(f) Outboard nacelles mounted in the chord plane location but pitched down 5° about their bases; $\alpha = 3°$.

Figure 3.- Continued.

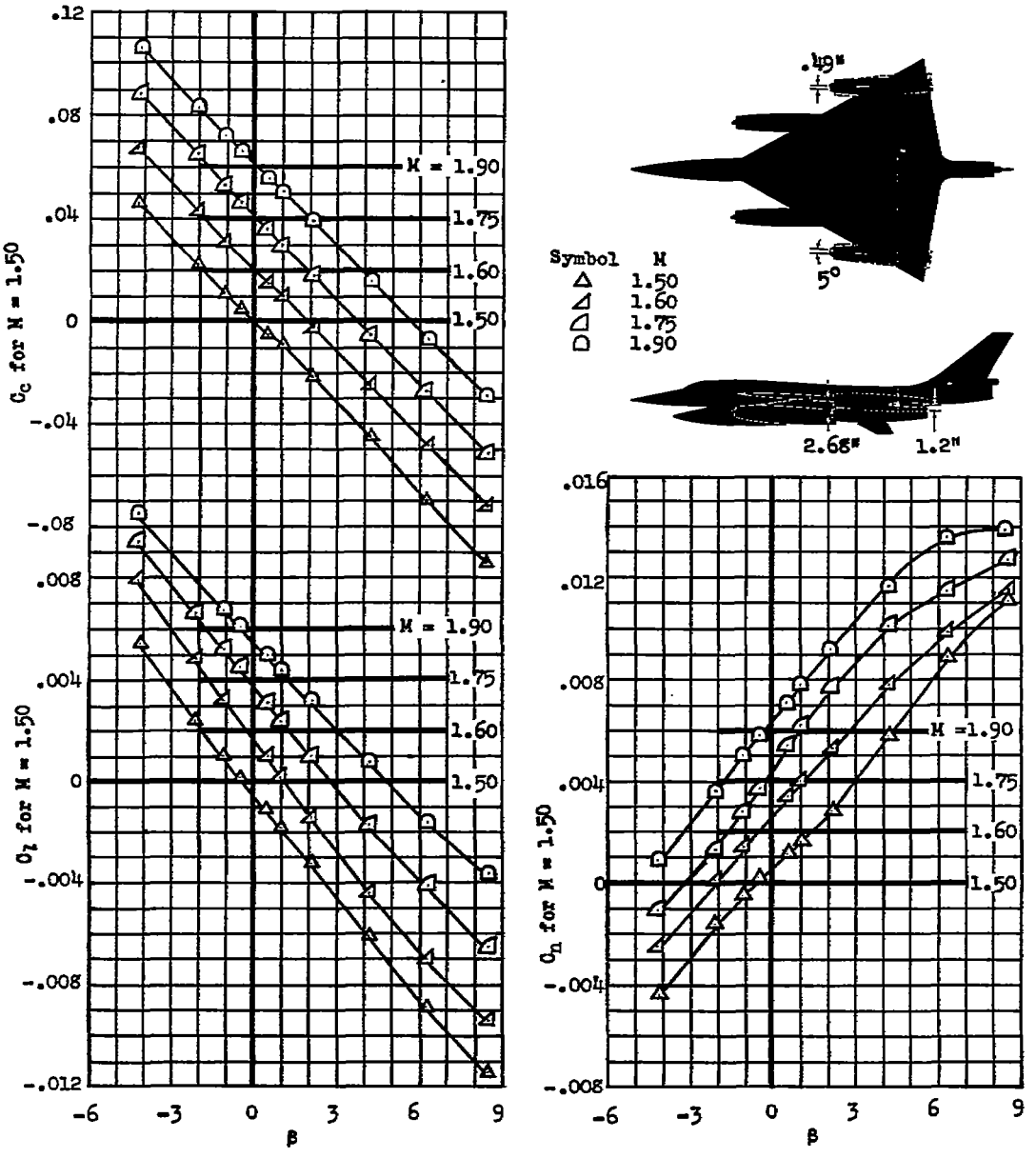

(g) Outboard nacelles mounted in the chord plane location and toed in 5°; $\alpha = 3°$.

Figure 3.- Continued.

[redacted]

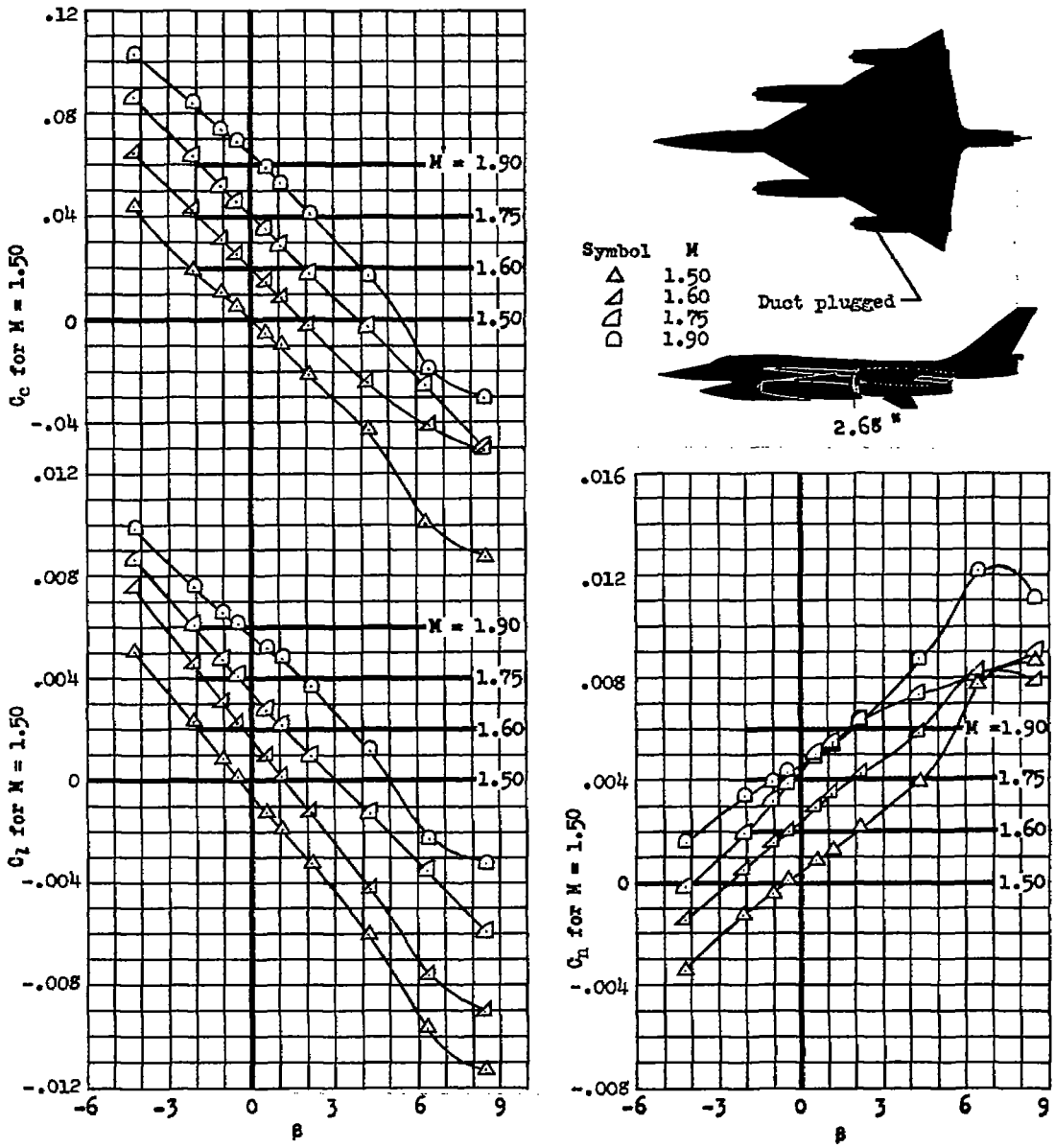

(h) Outboard nacelles mounted in the chord plane location with the outboard port nacelle plugged; $\alpha = 3^{\circ}$.

Figure 3.- Continued.

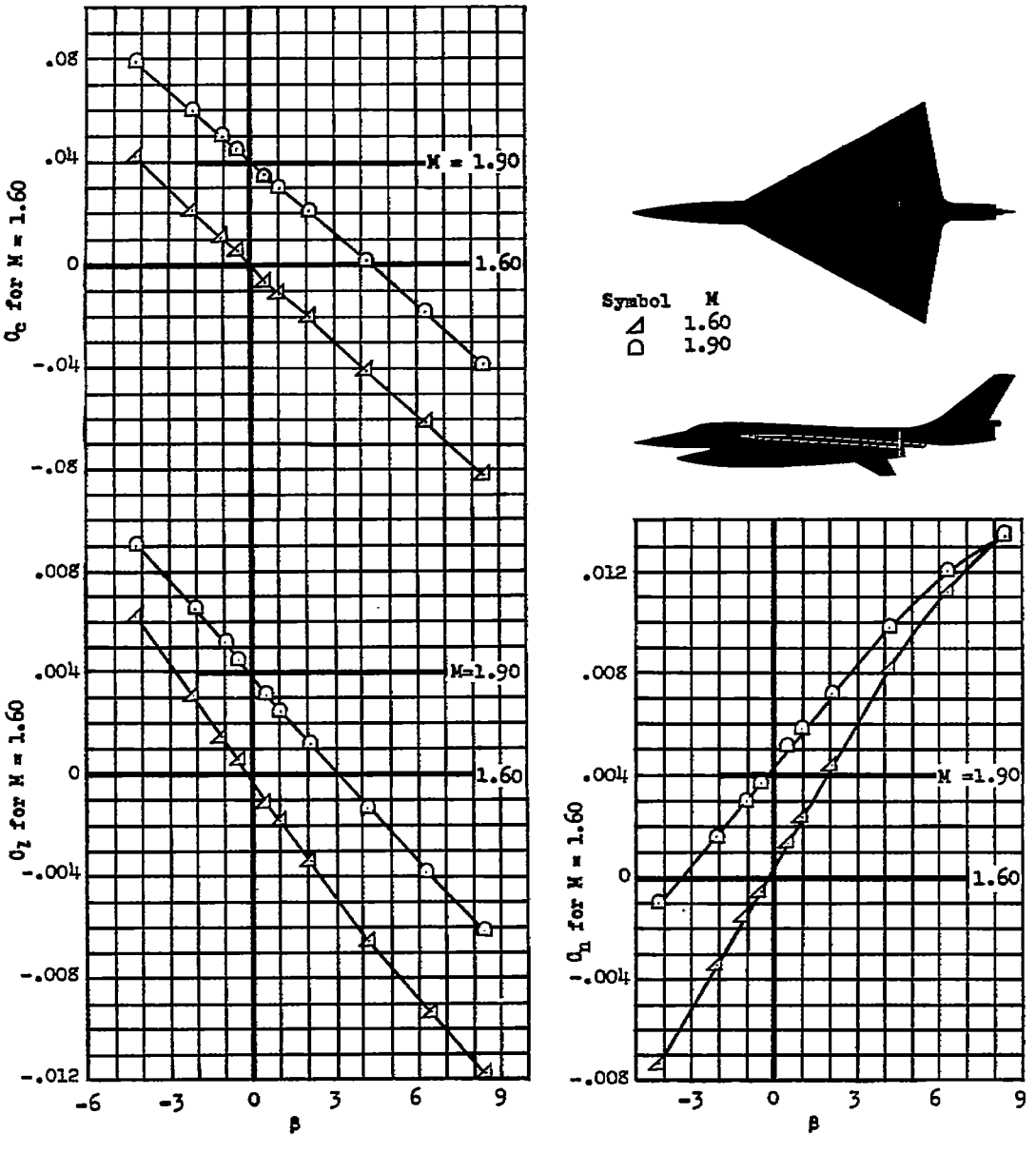

(i) Model without nacelles; $\alpha = 3^{\circ}$.

Figure 3.- Continued.

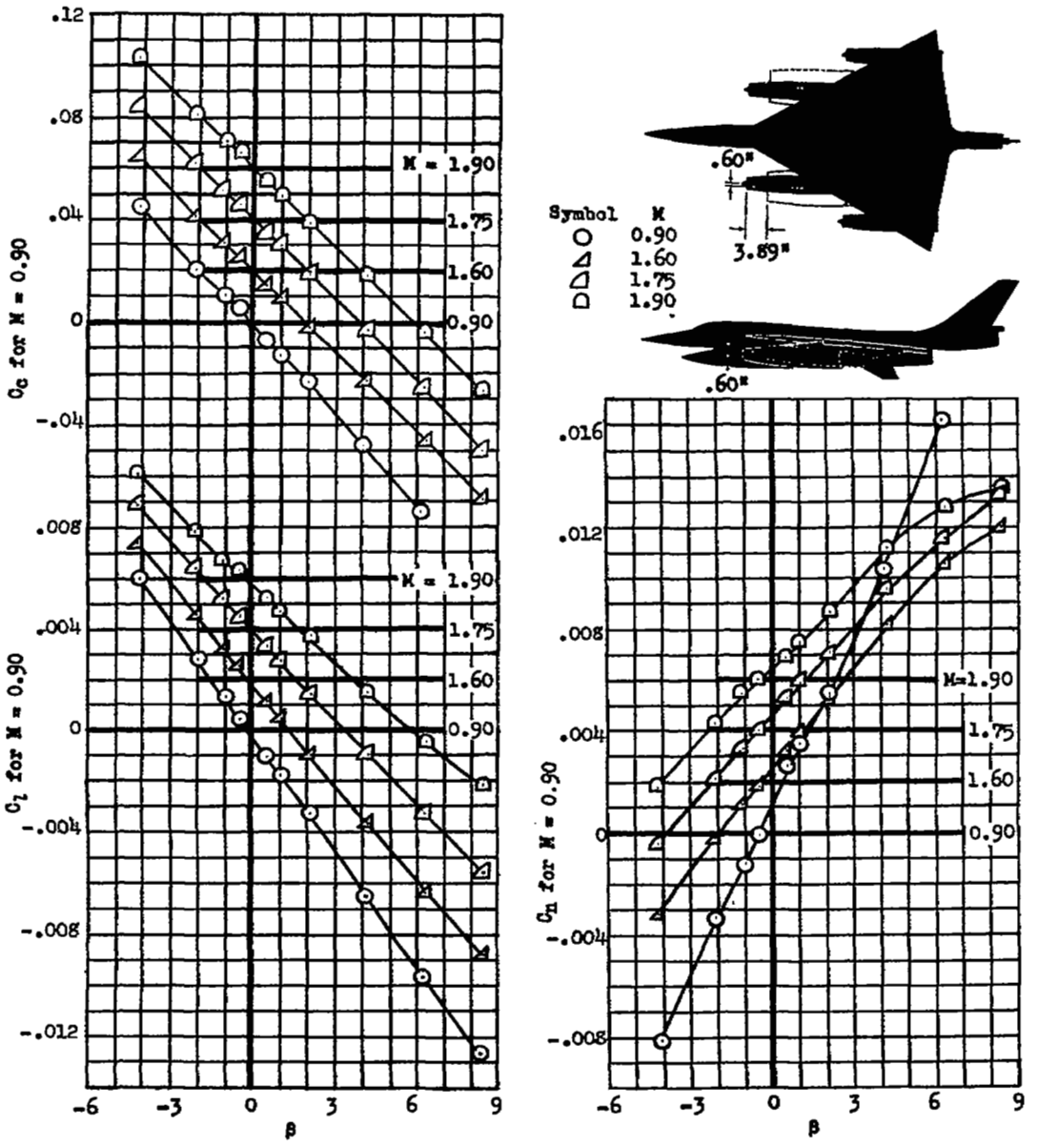

(j) Model with Siamese nacelles; $\alpha = 3^{\circ}$.

Figure 3.- Continued.

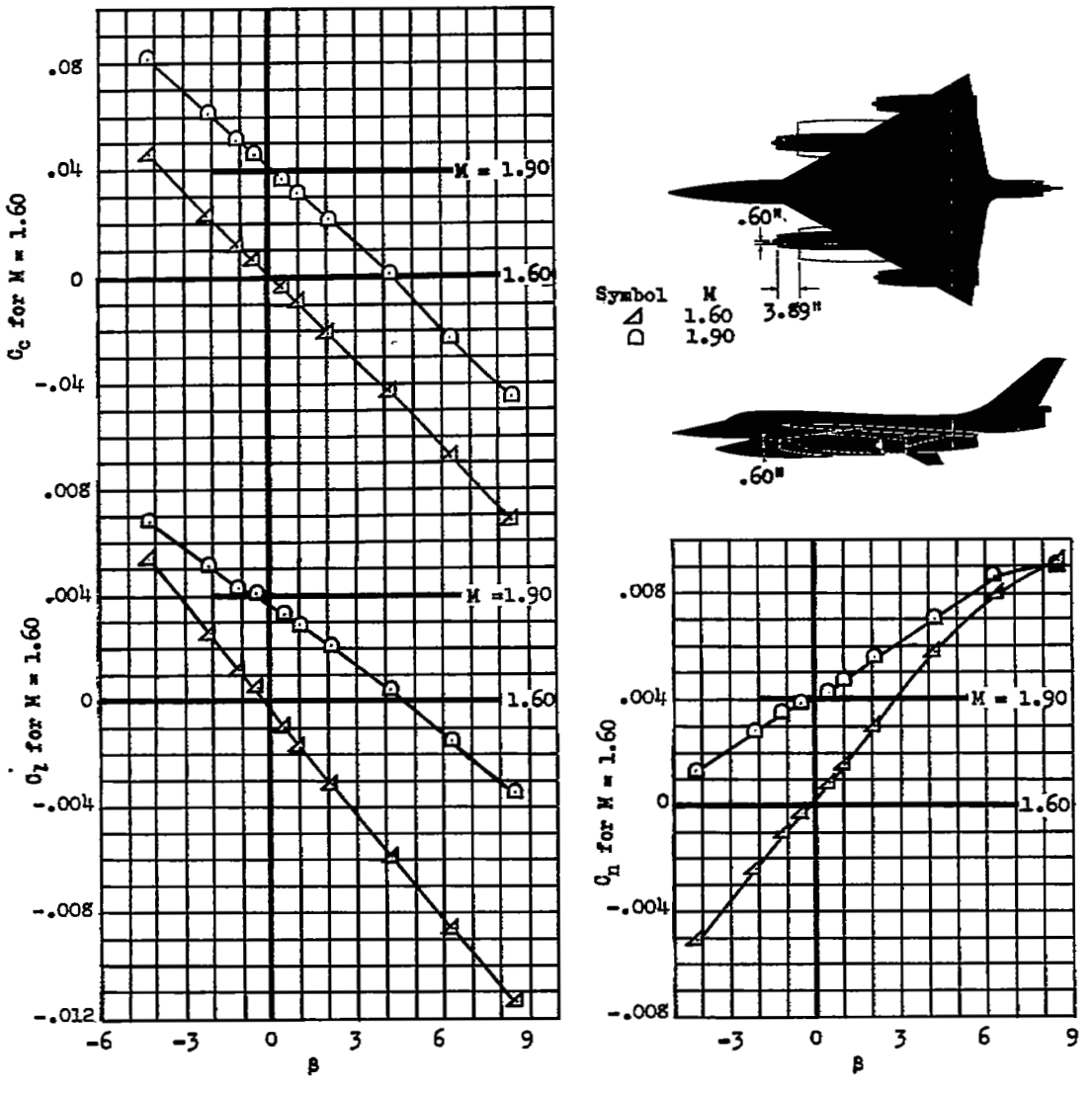

(k) Model with Siamese nacelles; $\alpha = 8^{\circ}$.

Figure 3.- Continued.

[redacted]

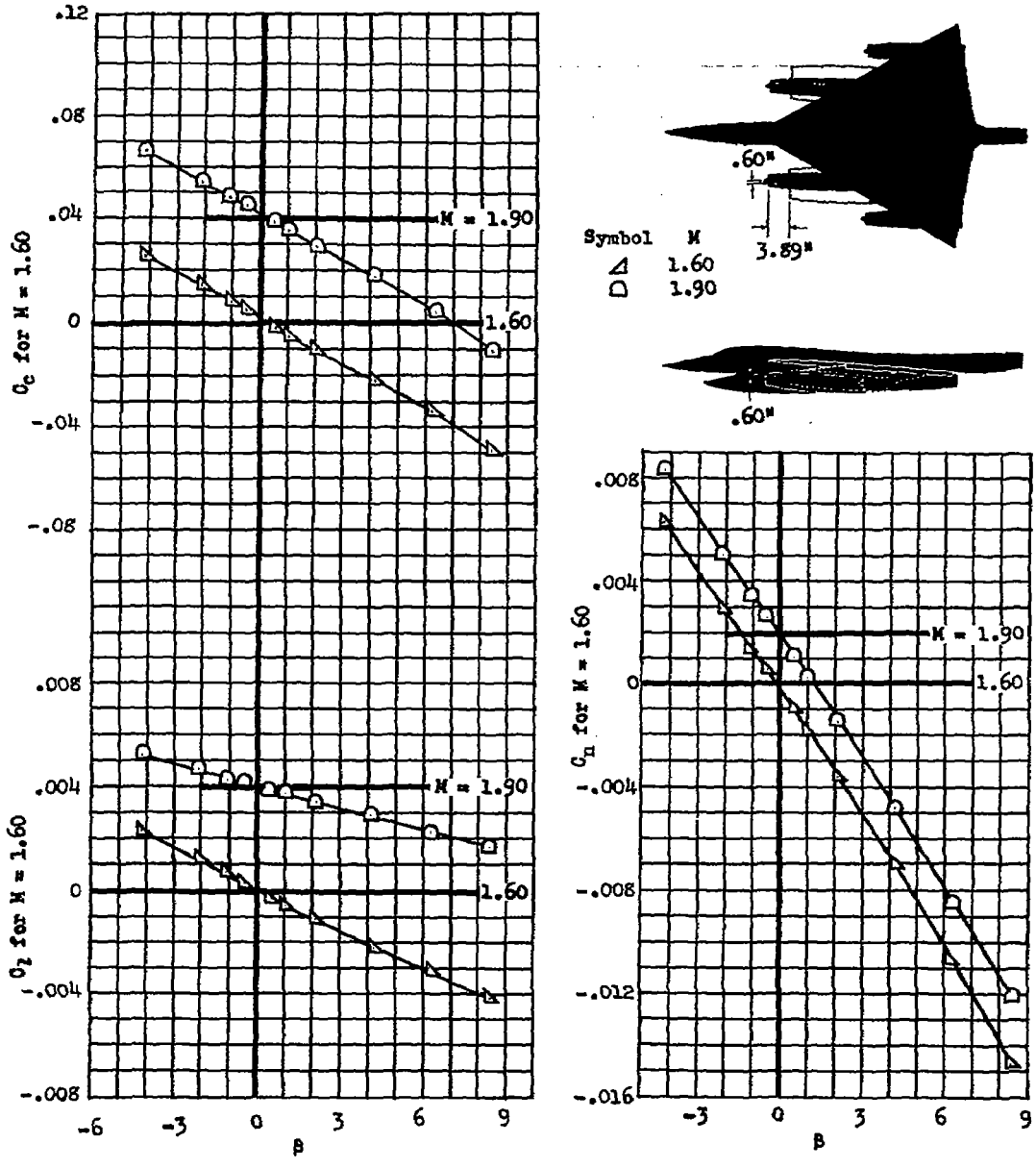

(1) Model with Siamese nacelles; without vertical tail; $\alpha = 3^{\circ}$.

Figure 3.- Continued.

[redacted]

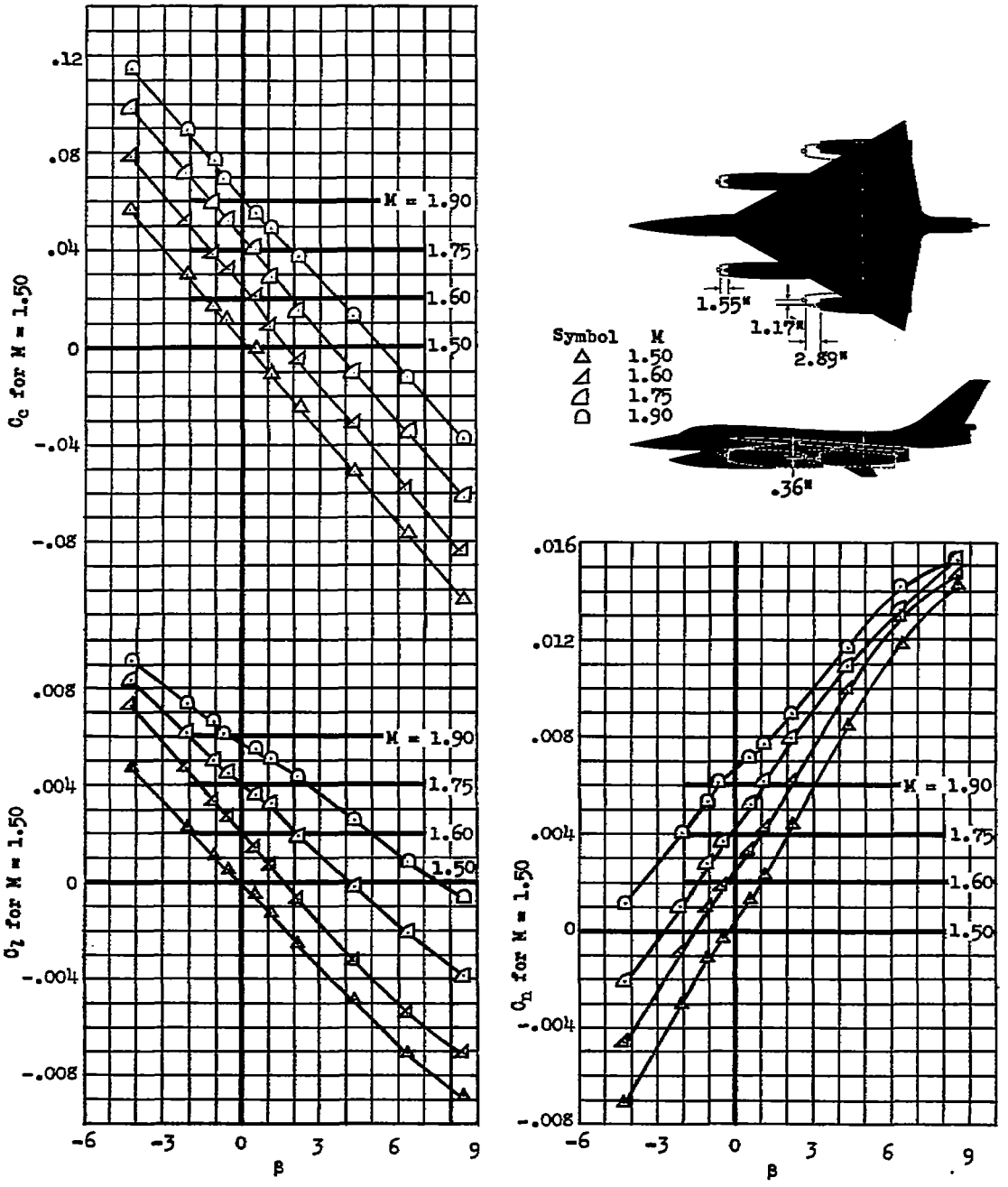

(m) Inboard nacelles moved forward; outboard nacelles pitched up 5°, and moved forward and inward; $\alpha = 3°$.

Figure 3.- Continued.

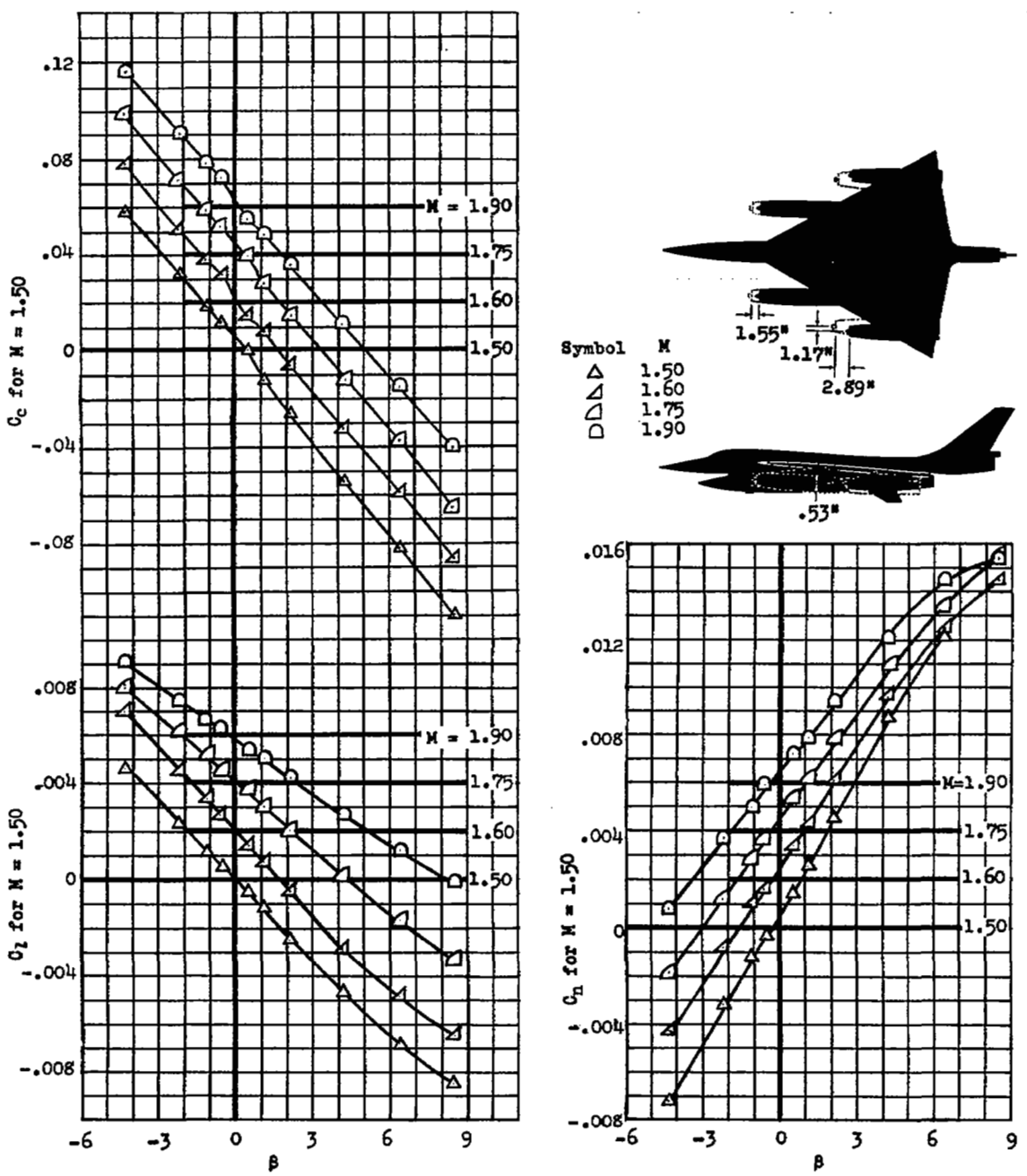

(n) Inboard nacelles moved forward; outboard nacelles moved forward, inward, and downward; $\alpha = 3^{\circ}$.

Figure 3.- Continued

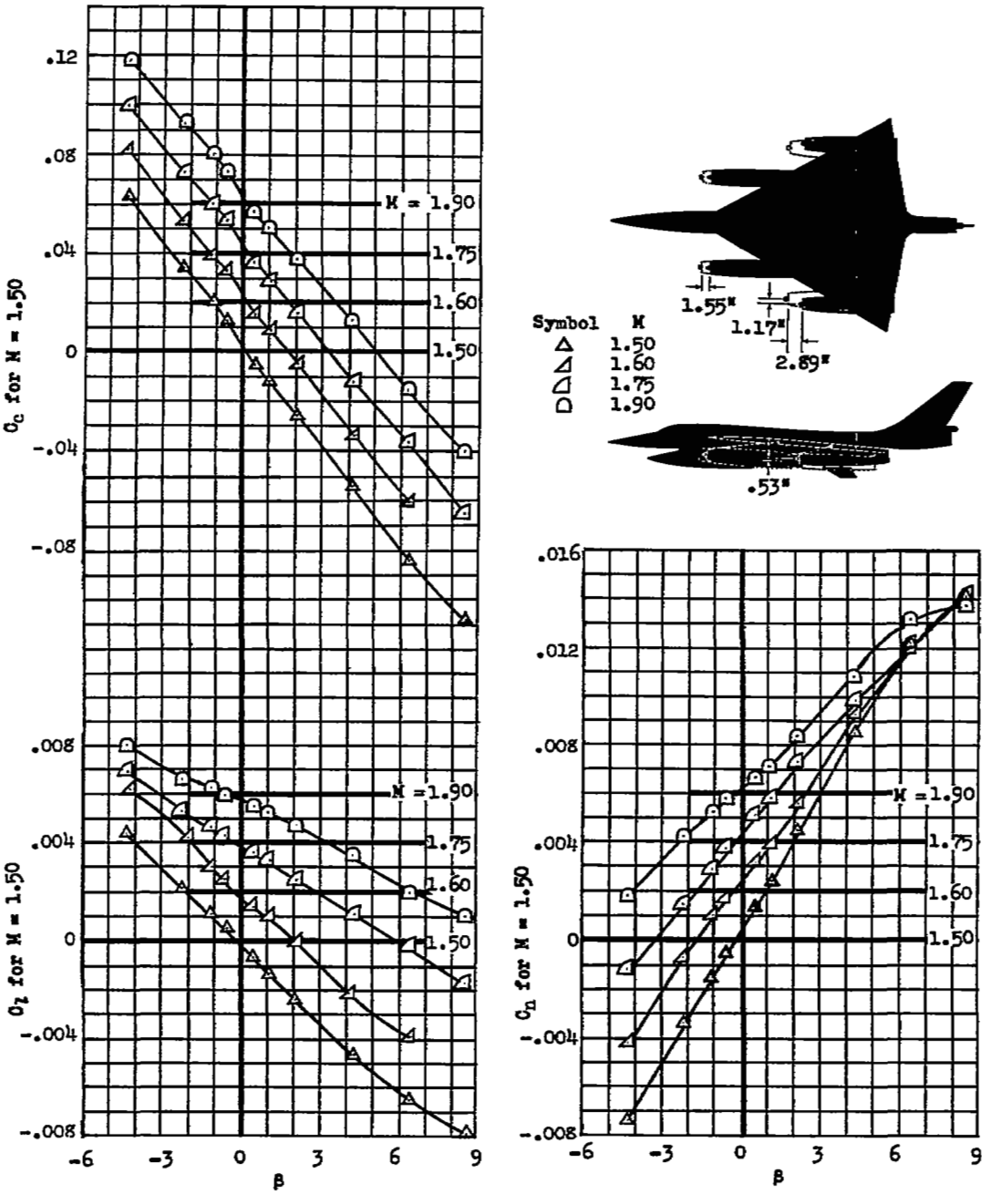

(o) Inboard nacelles moved forward; outboard nacelles moved forward, inward, and downward; $\alpha = 7^{\circ}$.

Figure 3.- Continued.

[redacted]

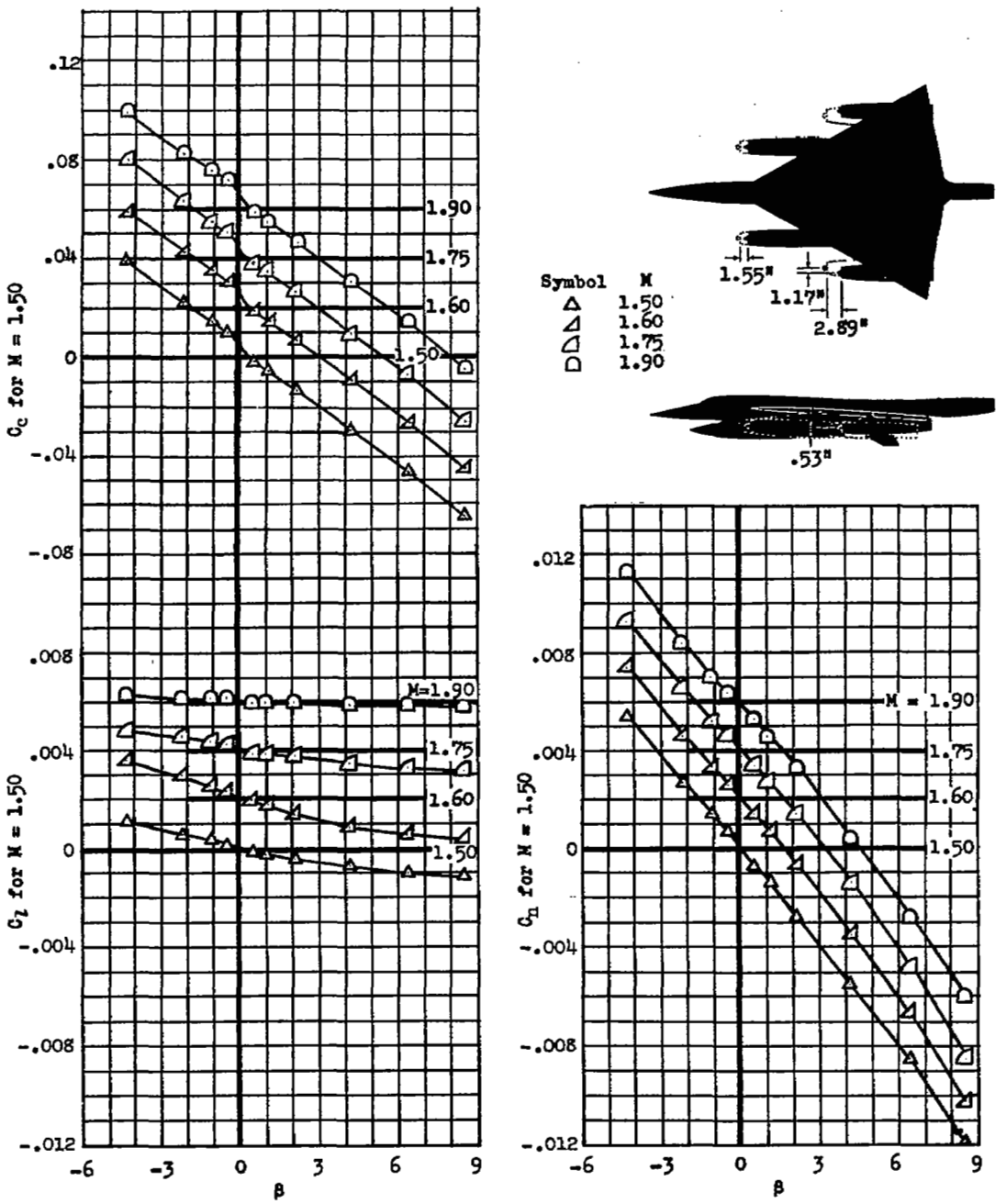

(p) Inboard nacelles moved forward; outboard nacelles moved forward, inward, and downward; without vertical tail; $\alpha = 3^{\circ}$.

Figure 3.- Continued.

[redacted]

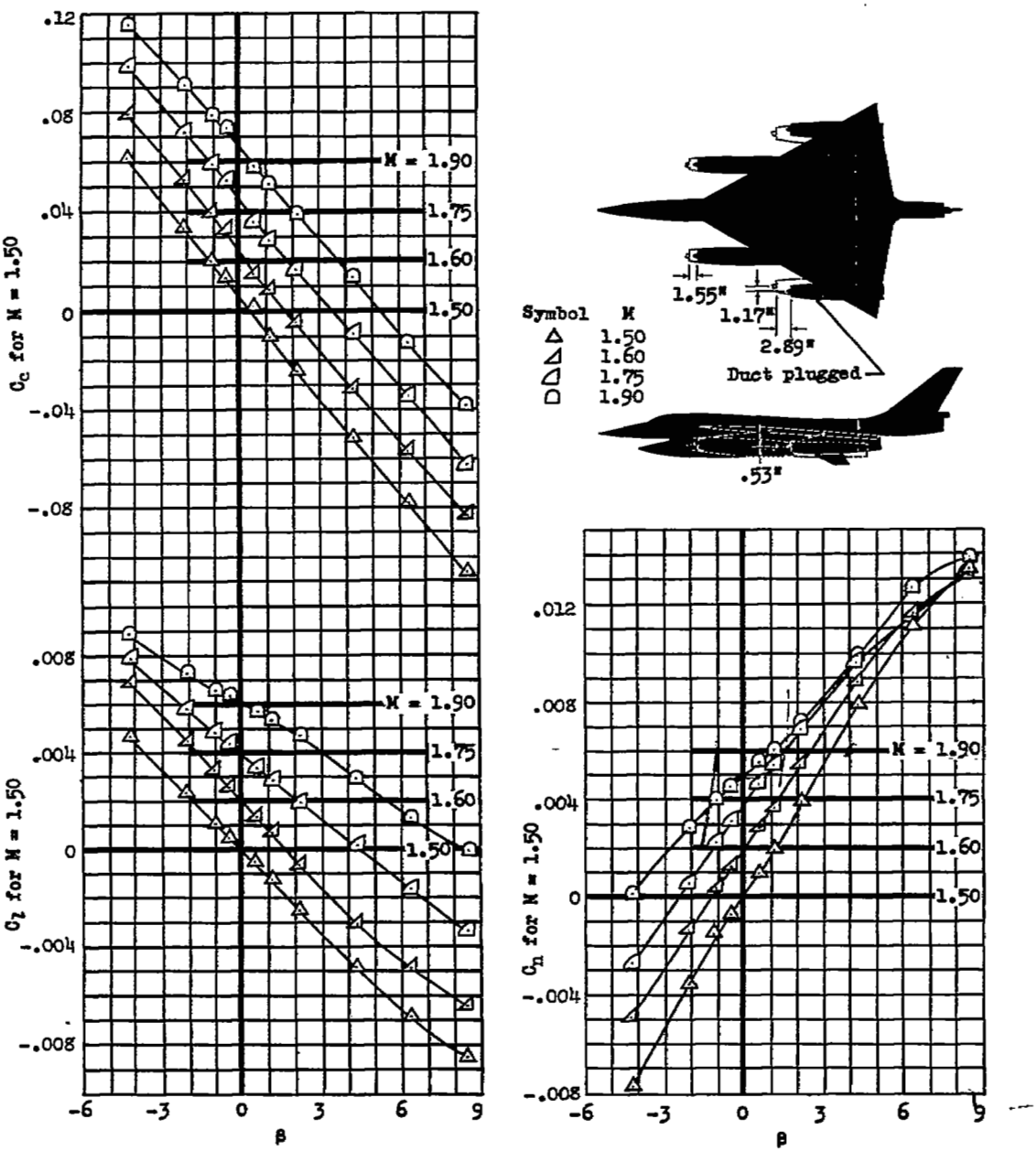

(q) Inboard nacelles moved forward; outboard nacelles moved forward, inward, and downward; outboard port nacelle plugged; $\alpha = 3^{\circ}$.

Figure 3.- Continued.

[redacted]

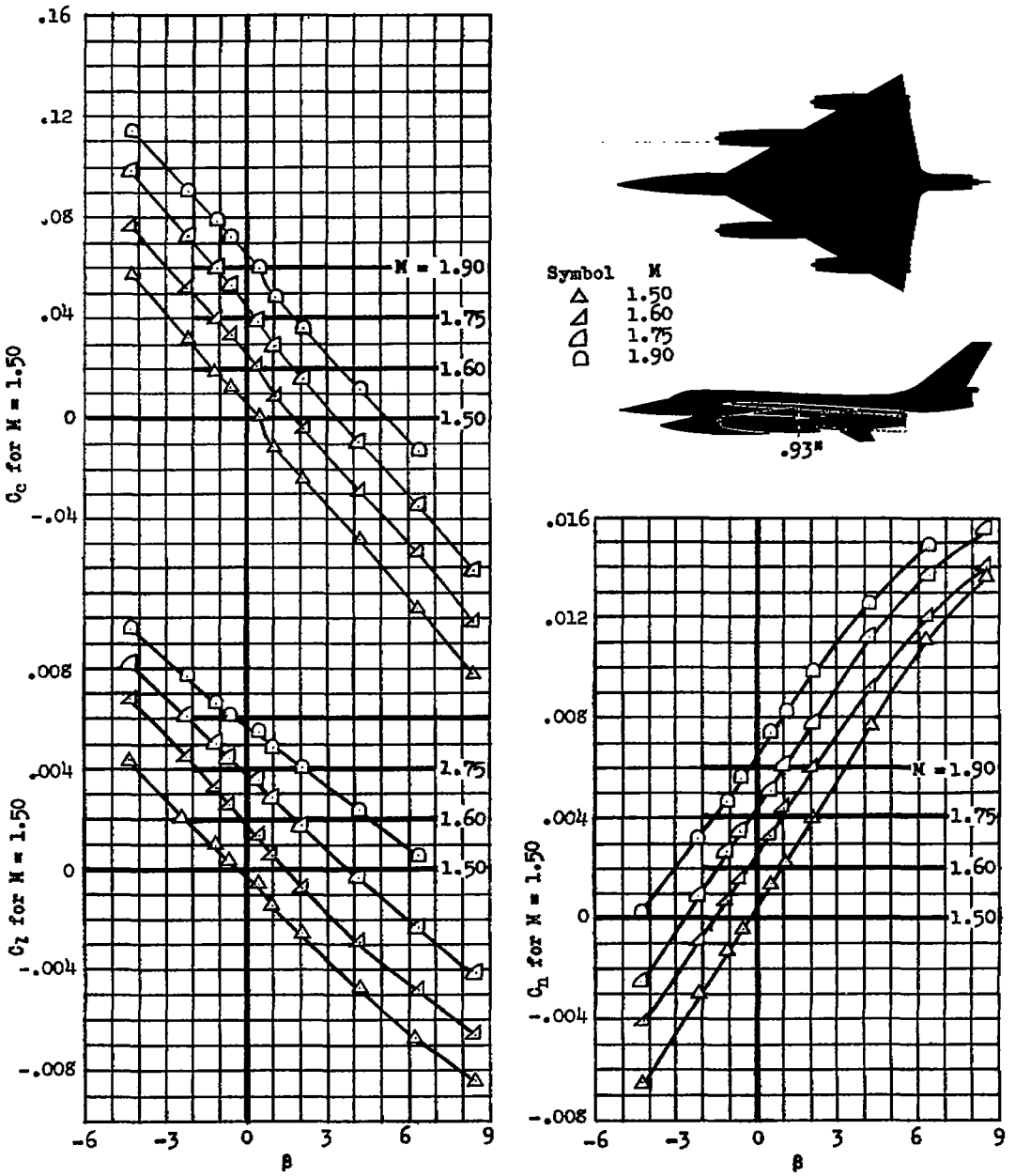

(r) Outboard nacelles pitched up 5°; $\alpha = 3°$.

Figure 3.- Continued.

[redacted]

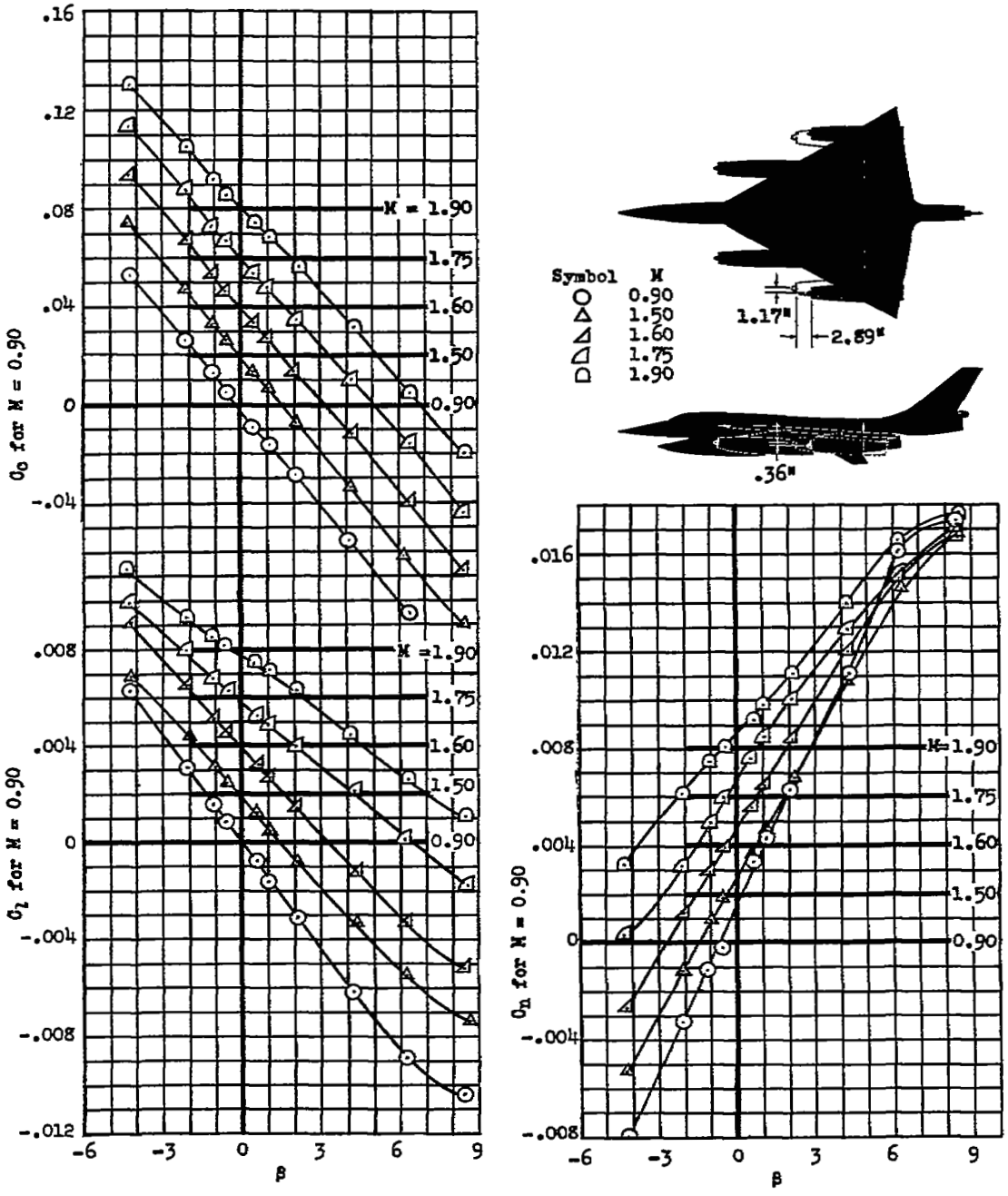

(s) Outboard nacelles pitched up 5° and moved forward and inward; $\alpha = 3°$.

Figure 3.- Continued.

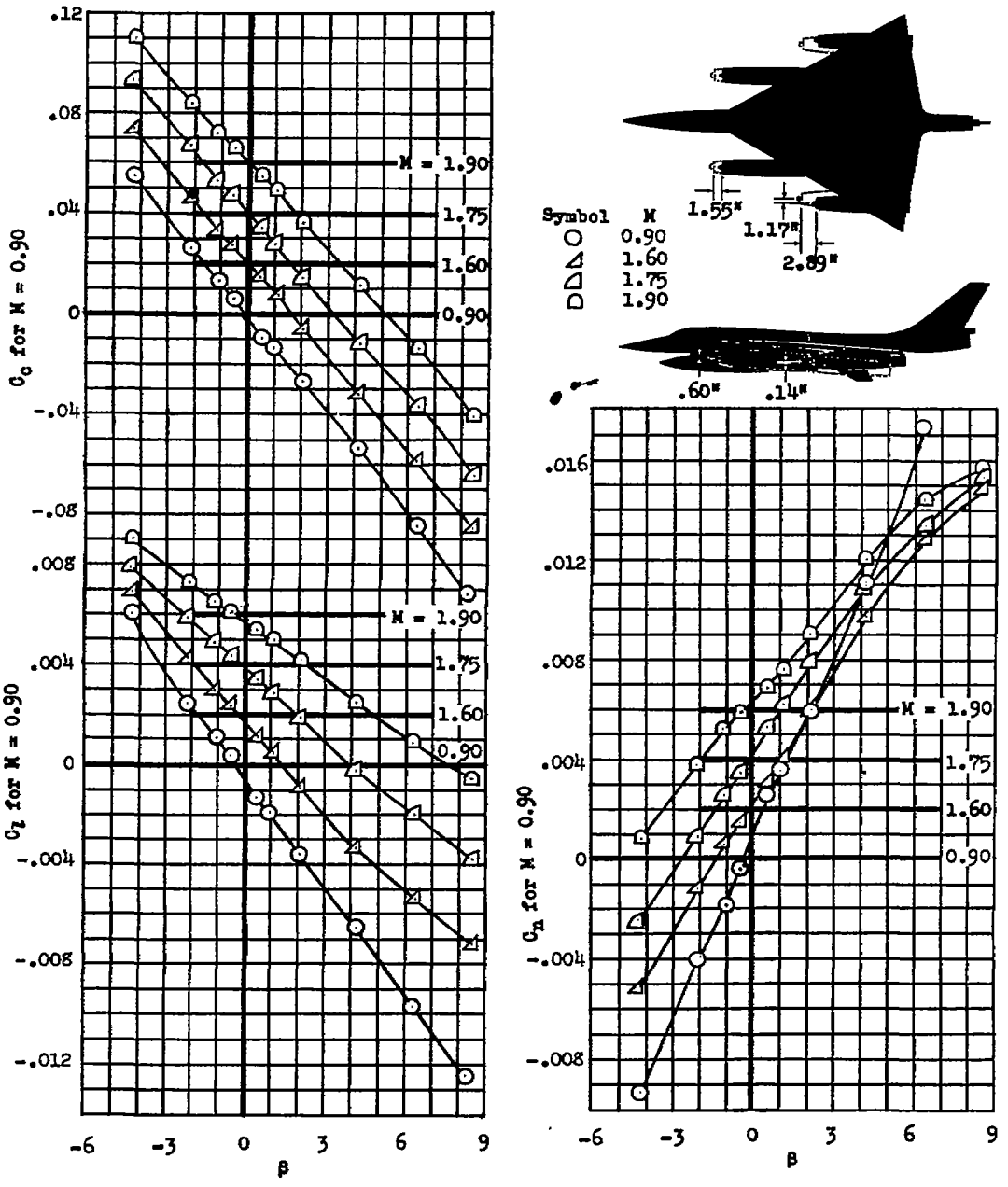

(t) Inboard nacelles moved forward and upward; outboard nacelles pitched up 5° and moved forward, inward, and downward; $\alpha = 3°$.

Figure 3.- Concluded.

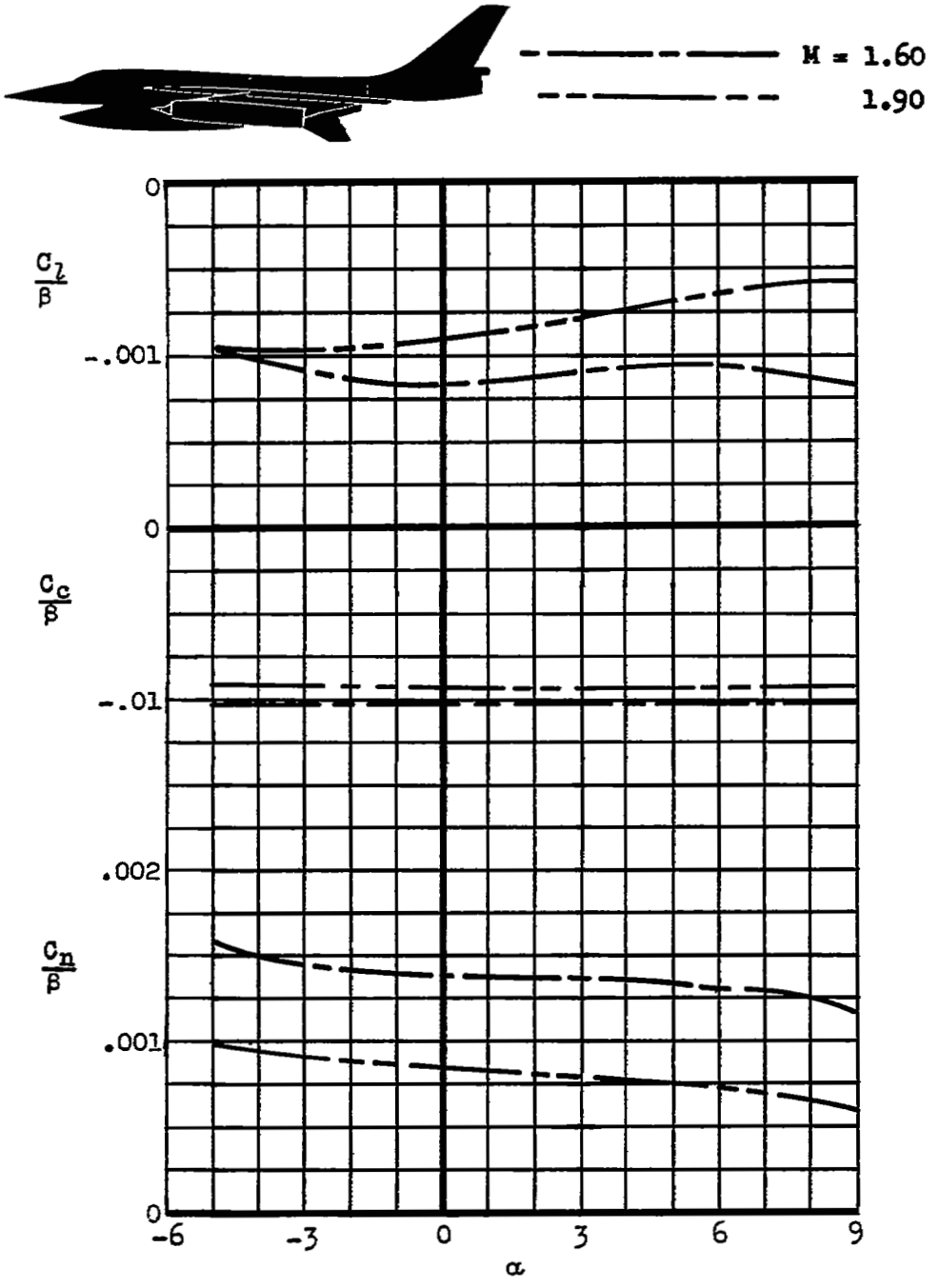

Figure 4.- Variation of lateral-directional stability parameters C_l/β, C_c/β, and C_n/β with angle of attack for Model A with Siamese nacelles.

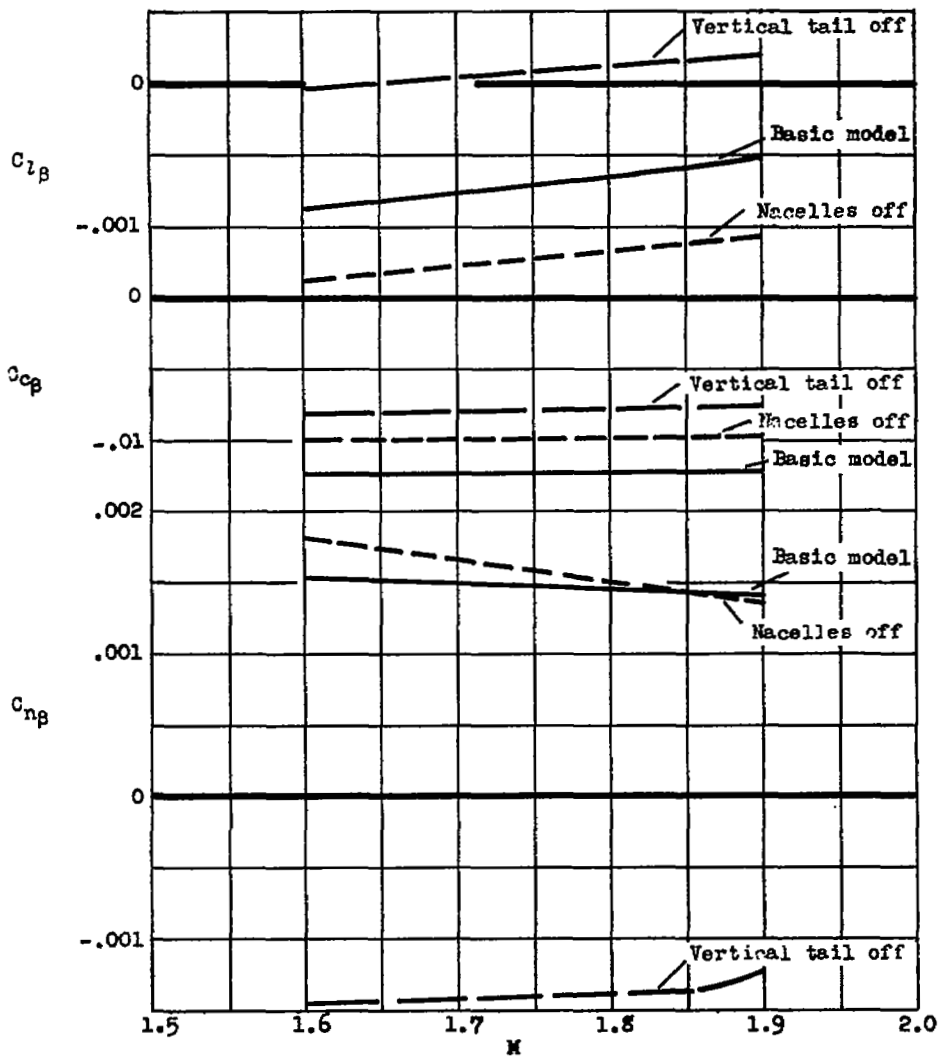

(a) Complete model, model less vertical tail, and model less nacelles; $\alpha = 3^{\circ}$.

Figure 5.- Variation of lateral-directional stability derivatives with Mach number for Model A.

[redacted]

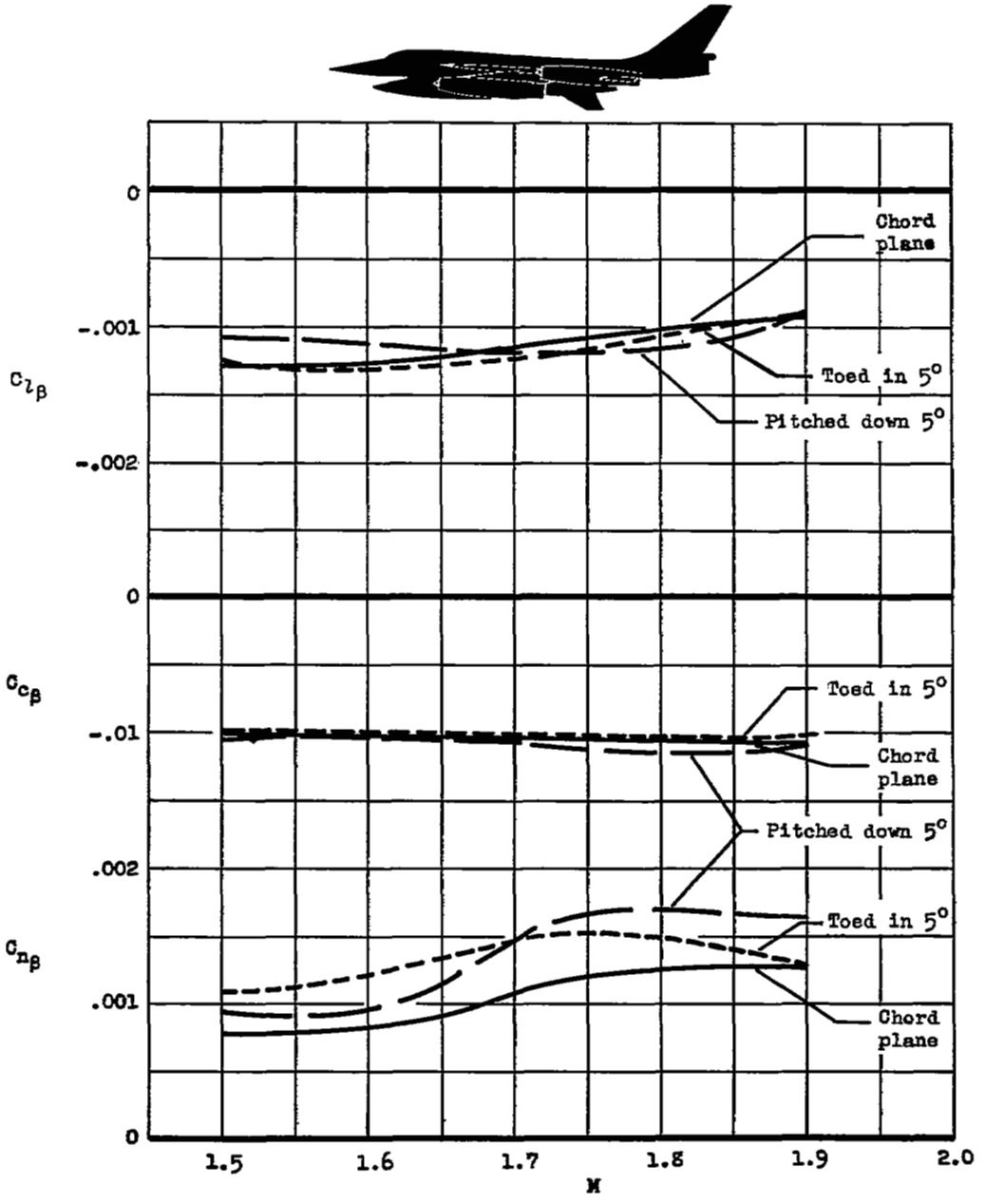

(b) Outboard nacelles mounted in the wing chord plane, showing the effects of modifications to the outboard nacelles; $\alpha = 3^\circ$.

Figure 5.- Continued.

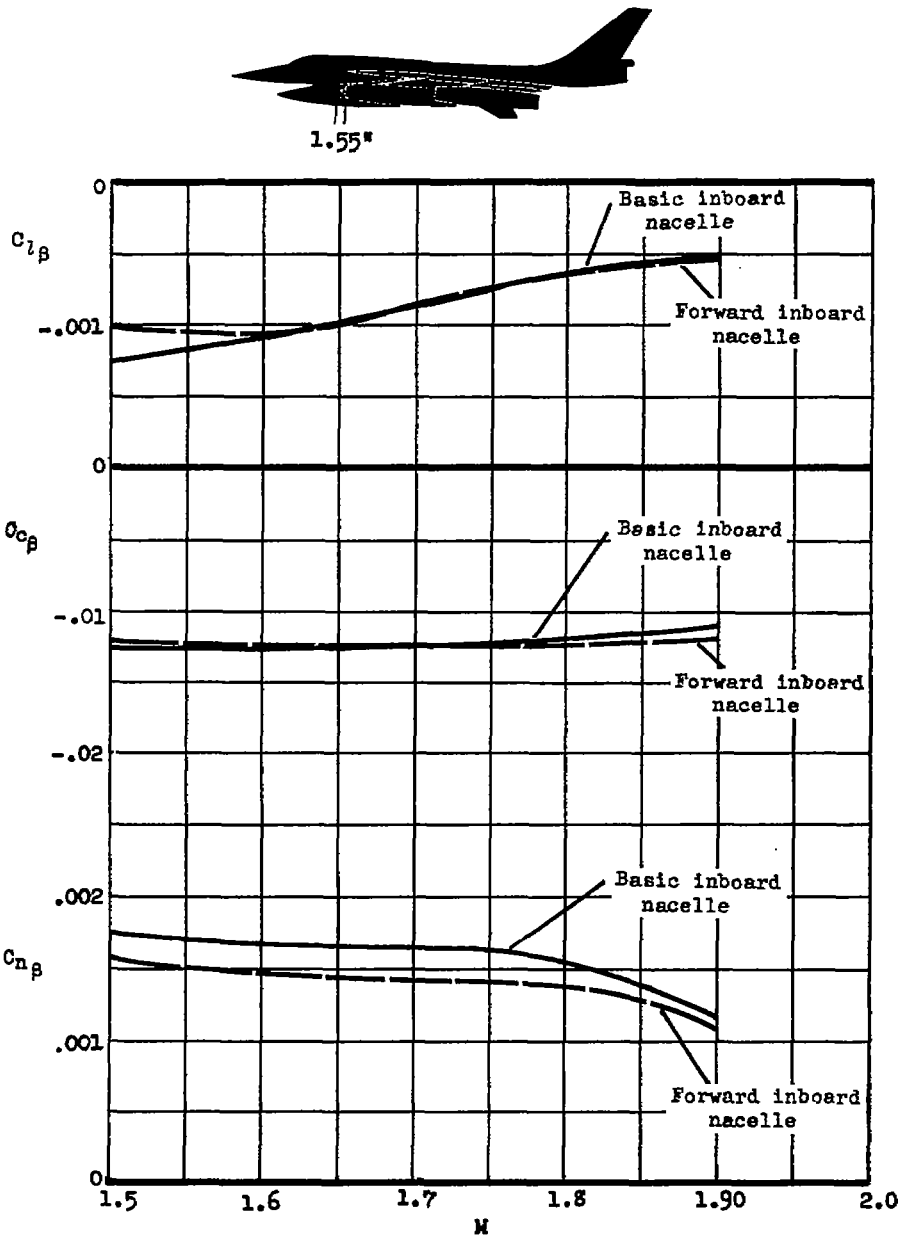

(c) Outboard nacelles pylon mounted under the wing, showing the effects of a chordwise shift of the inboard nacelles; $\alpha = 3^{\circ}$.

Figure 5.- Continued.

[redacted]

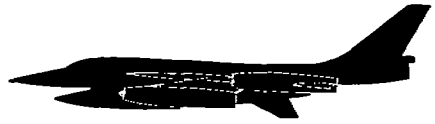

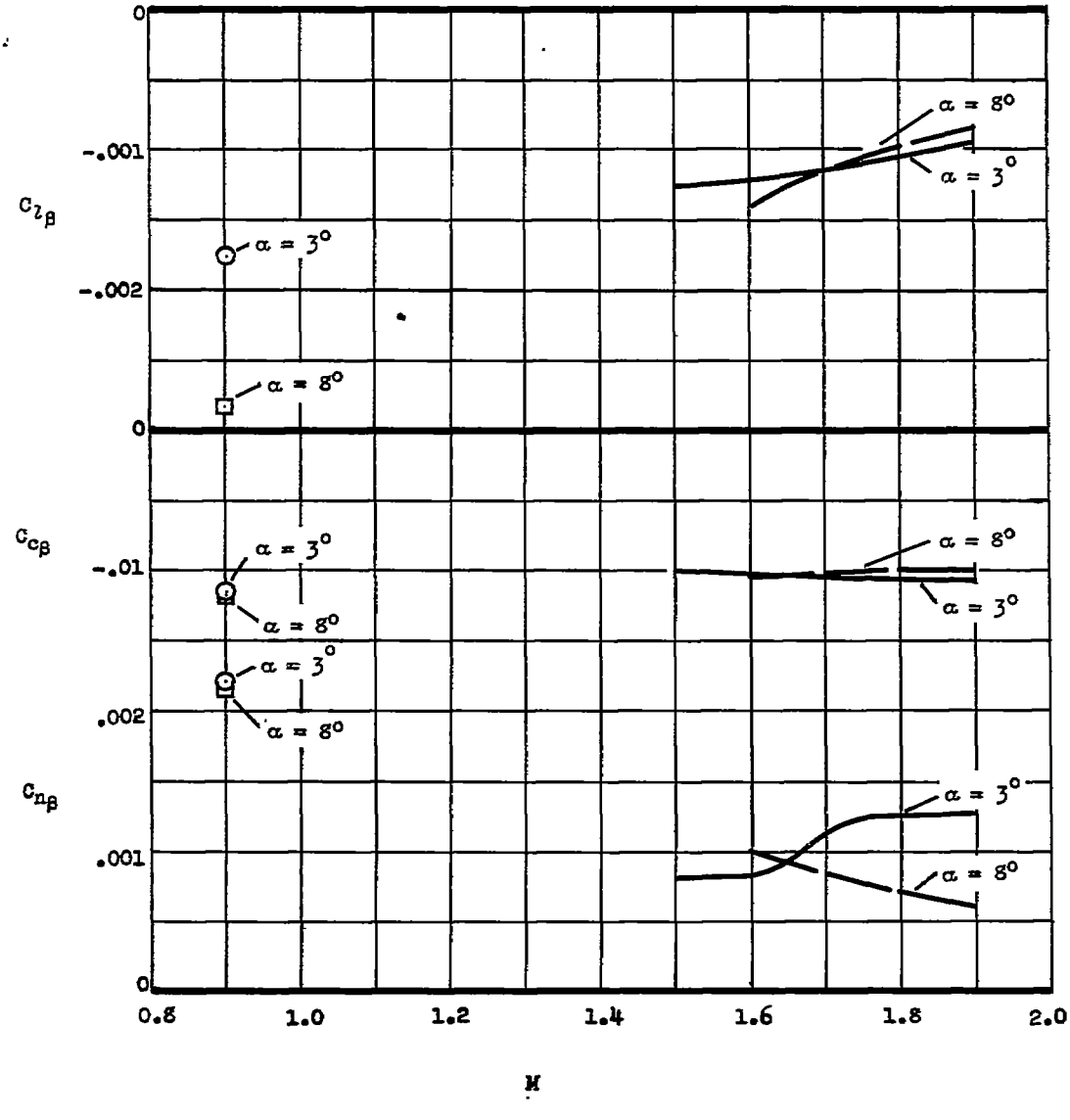

(d) Outboard nacelles mounted in the wing chord plane; $\alpha = 3^\circ$ and 8°.

Figure 5.- Continued.

[redacted]

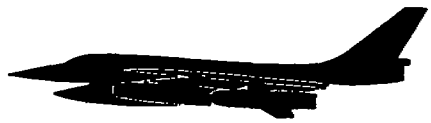

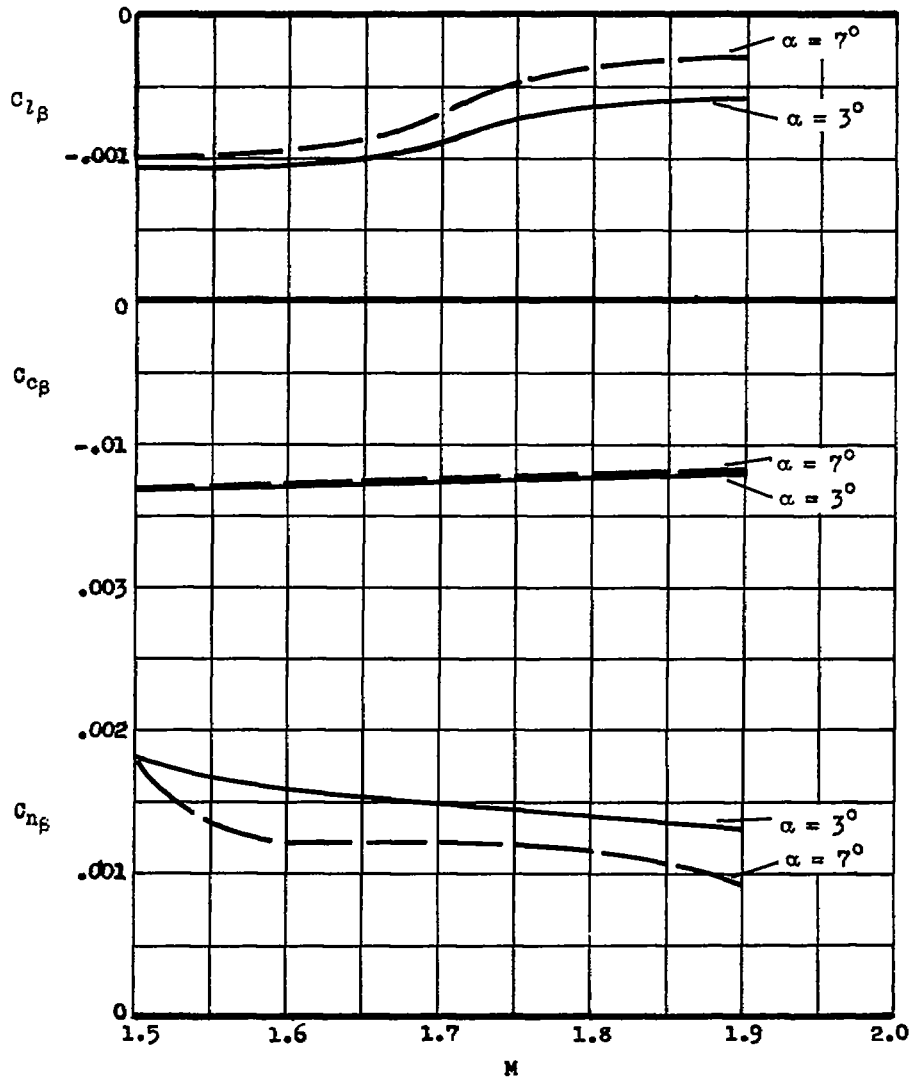

(e) Inboard nacelles moved forward; outboard nacelles moved downward, forward, and inward; $\alpha = 3^\circ$ and 7°.

Figure 5.- Continued.

[redacted]

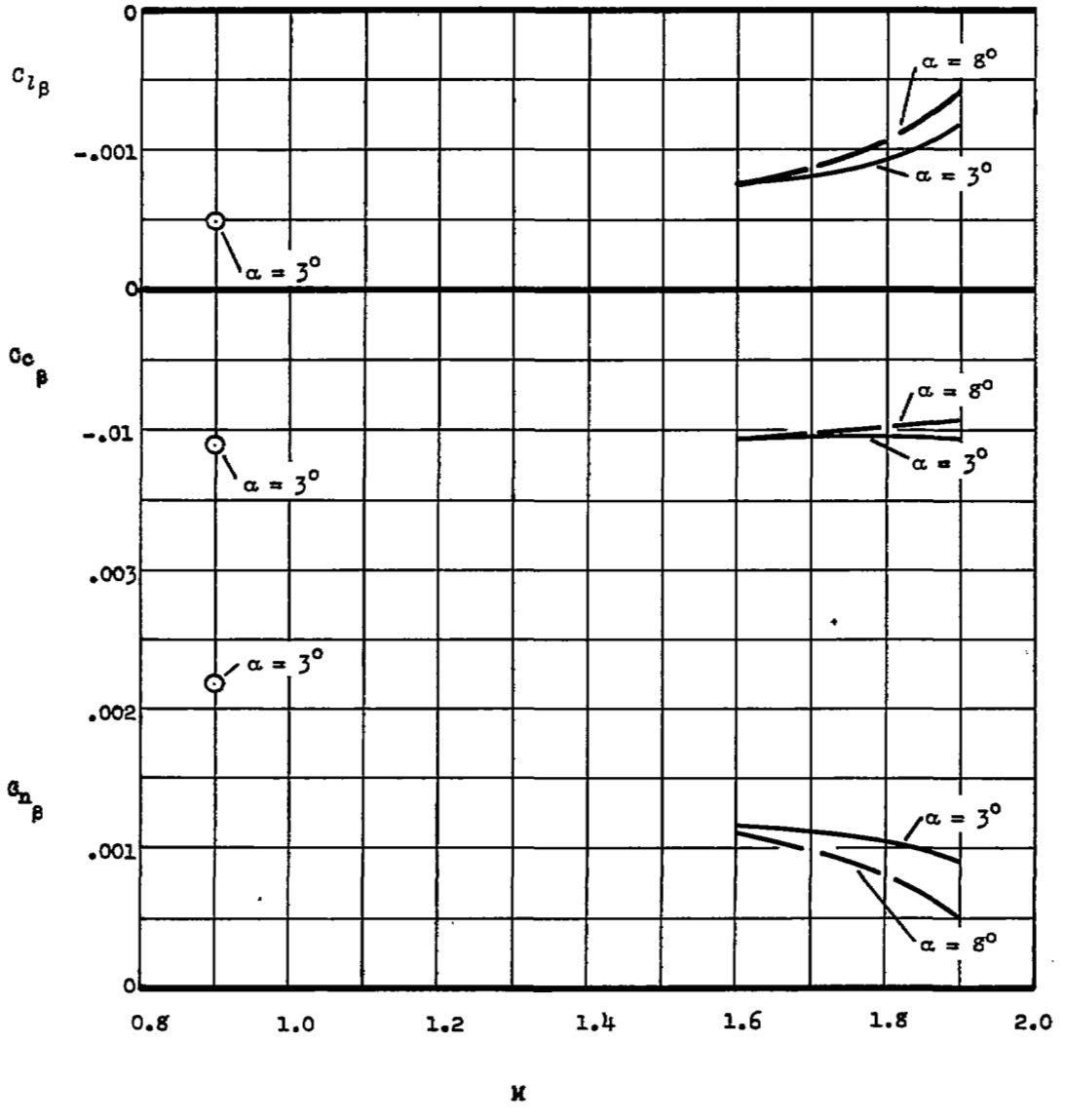

(f) Model with Siamese nacelles; $\alpha = 3^\circ$ and 8°.

Figure 5.- Concluded.

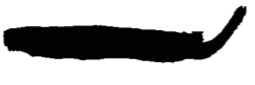

All dimensions shown in inches unless otherwise noted

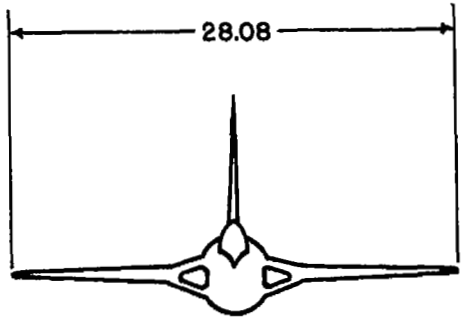

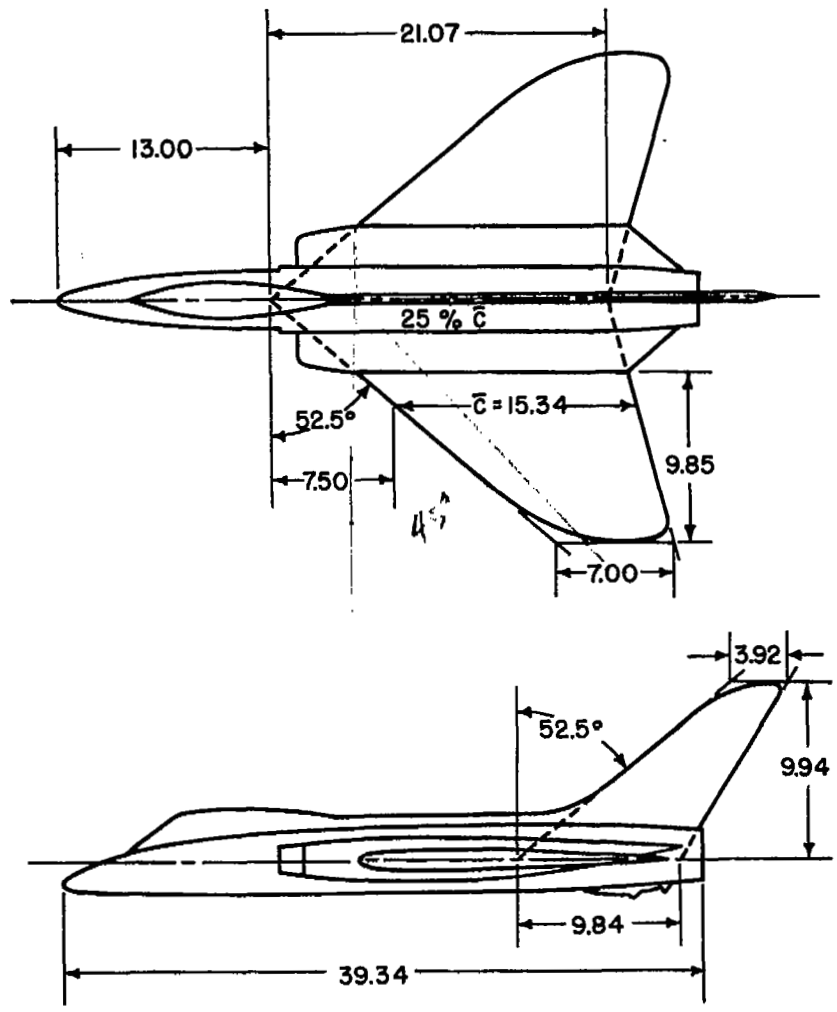

Figure 6.- Dimensional sketch of Model B.

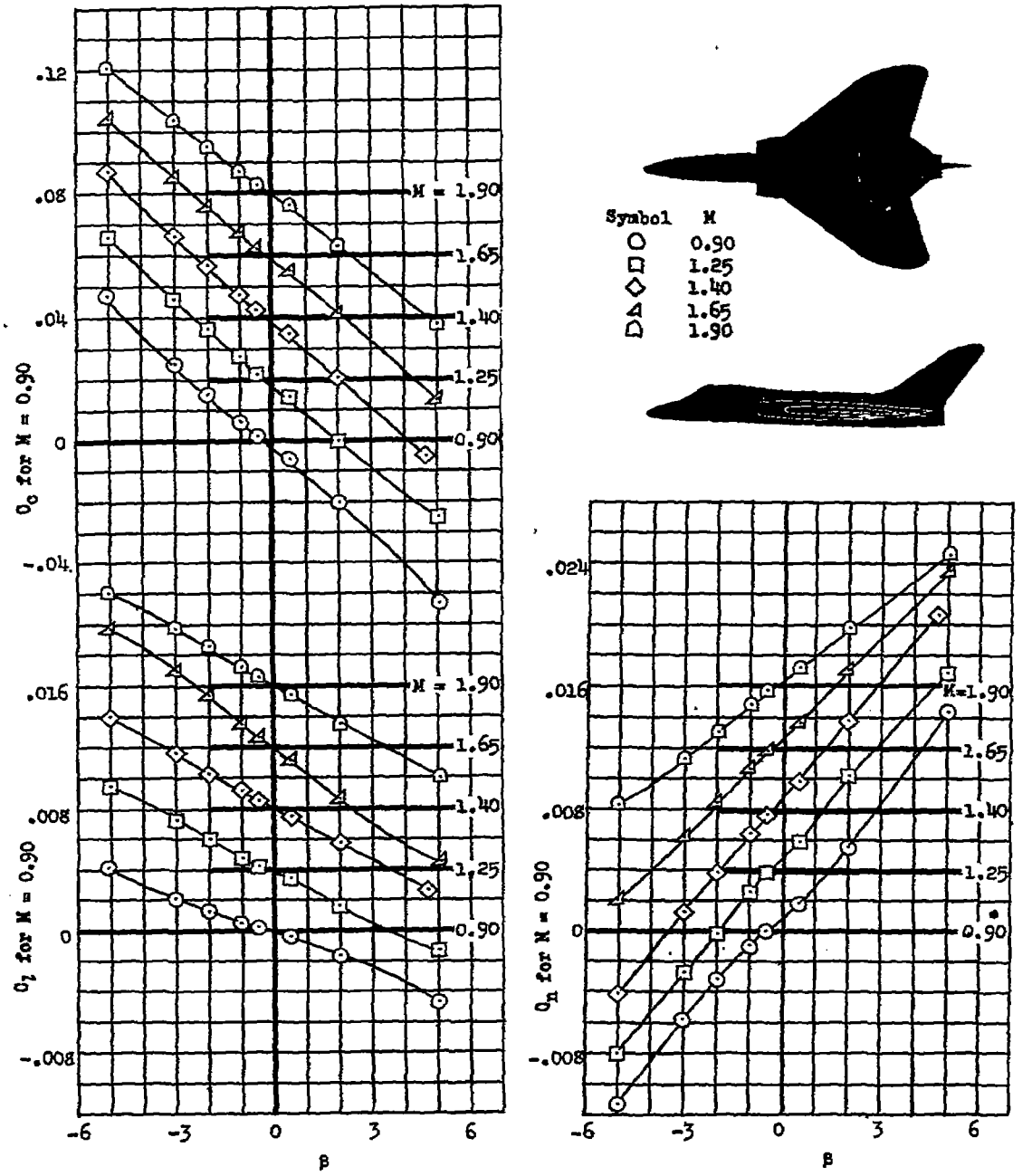

(a) Basic model; $\alpha = 0^{\circ}$.

Figure 7.- Variation of lateral-directional stability characteristics with angle of sideslip for Model B.

[redacted]

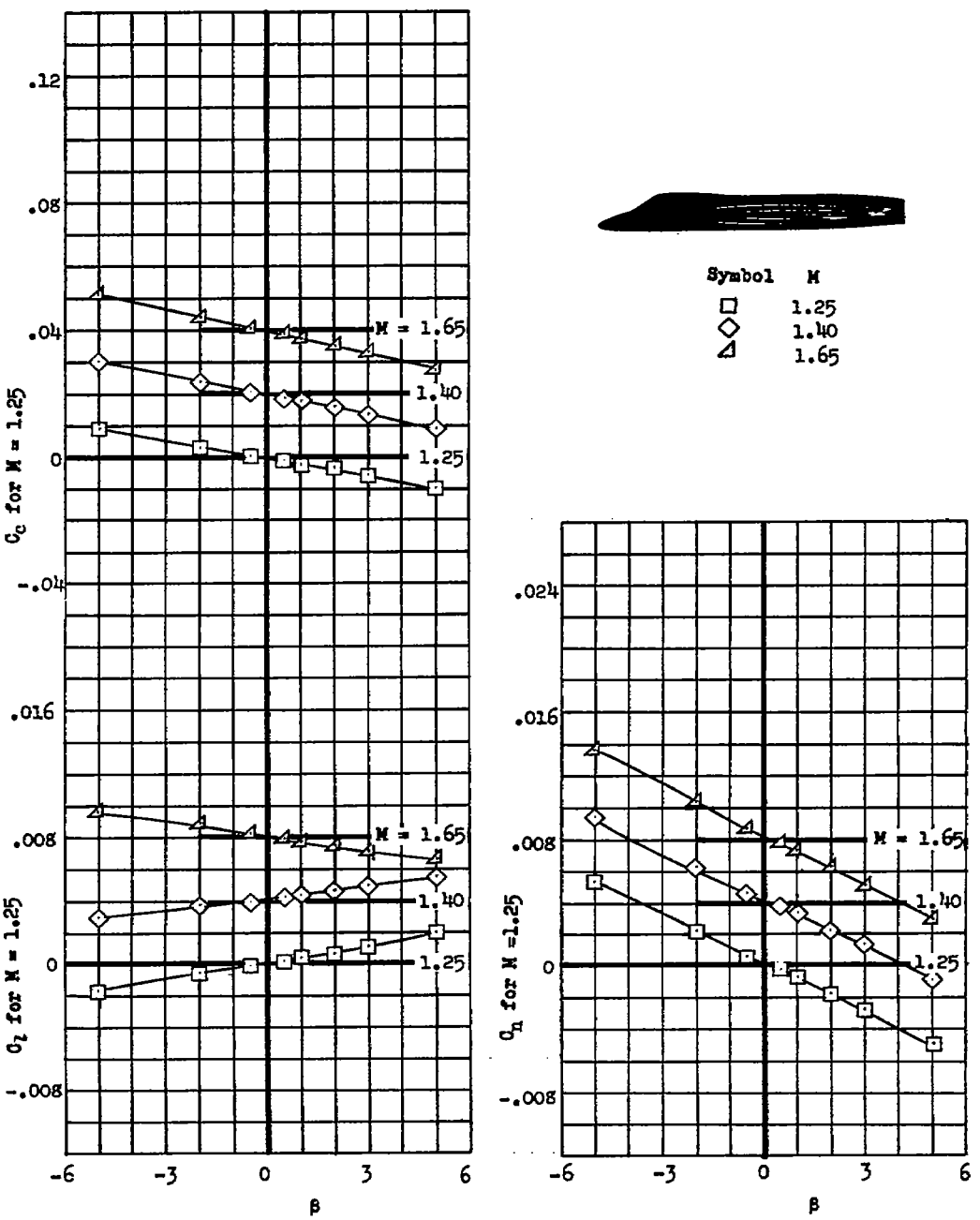

(b) Model without vertical tail; $\alpha = 0^{\circ}$.

Figure 7.- Continued.

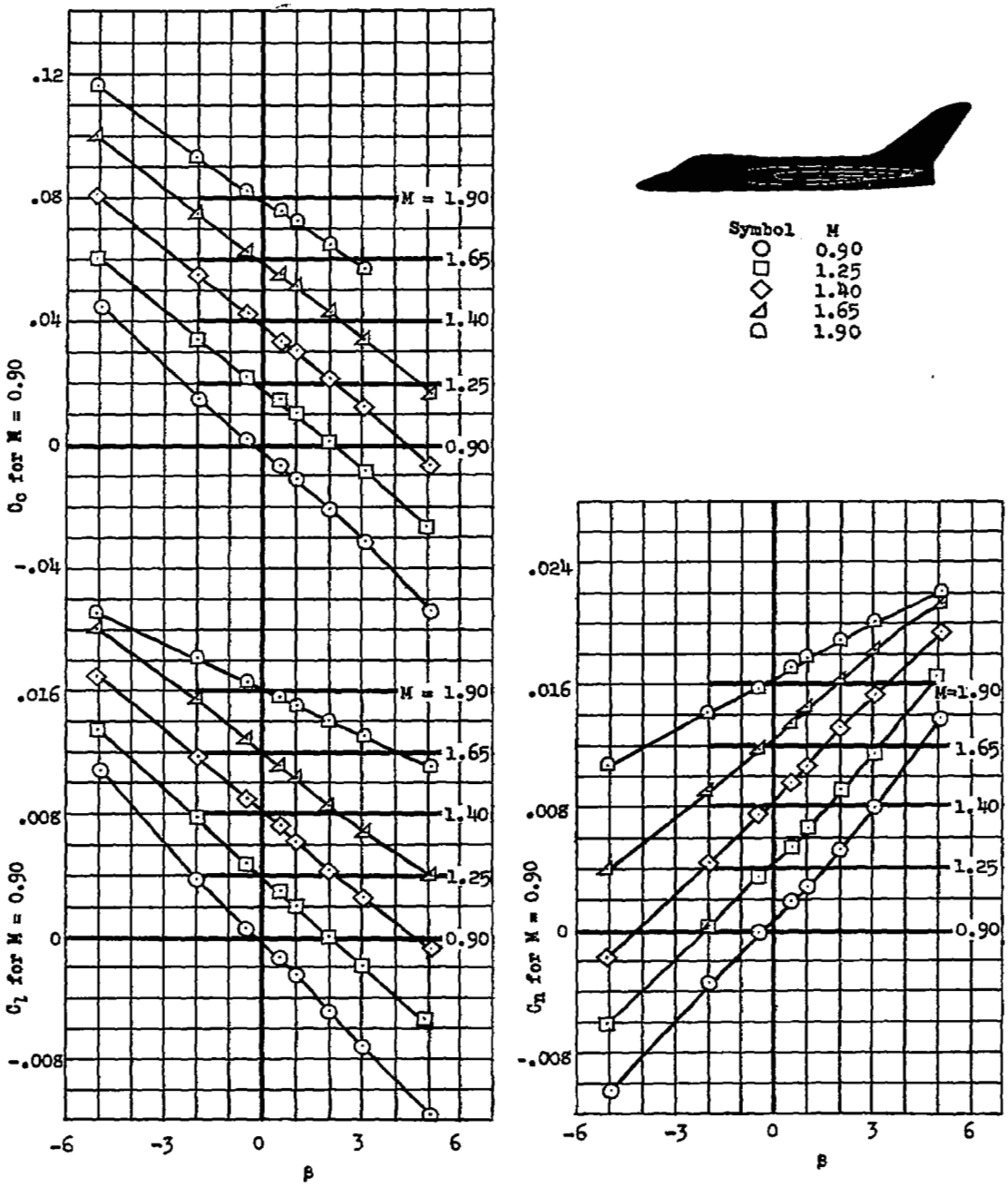

(c) Basic model; $\alpha = 5^{\circ}$.

Figure 7.- Continued.

[redacted]

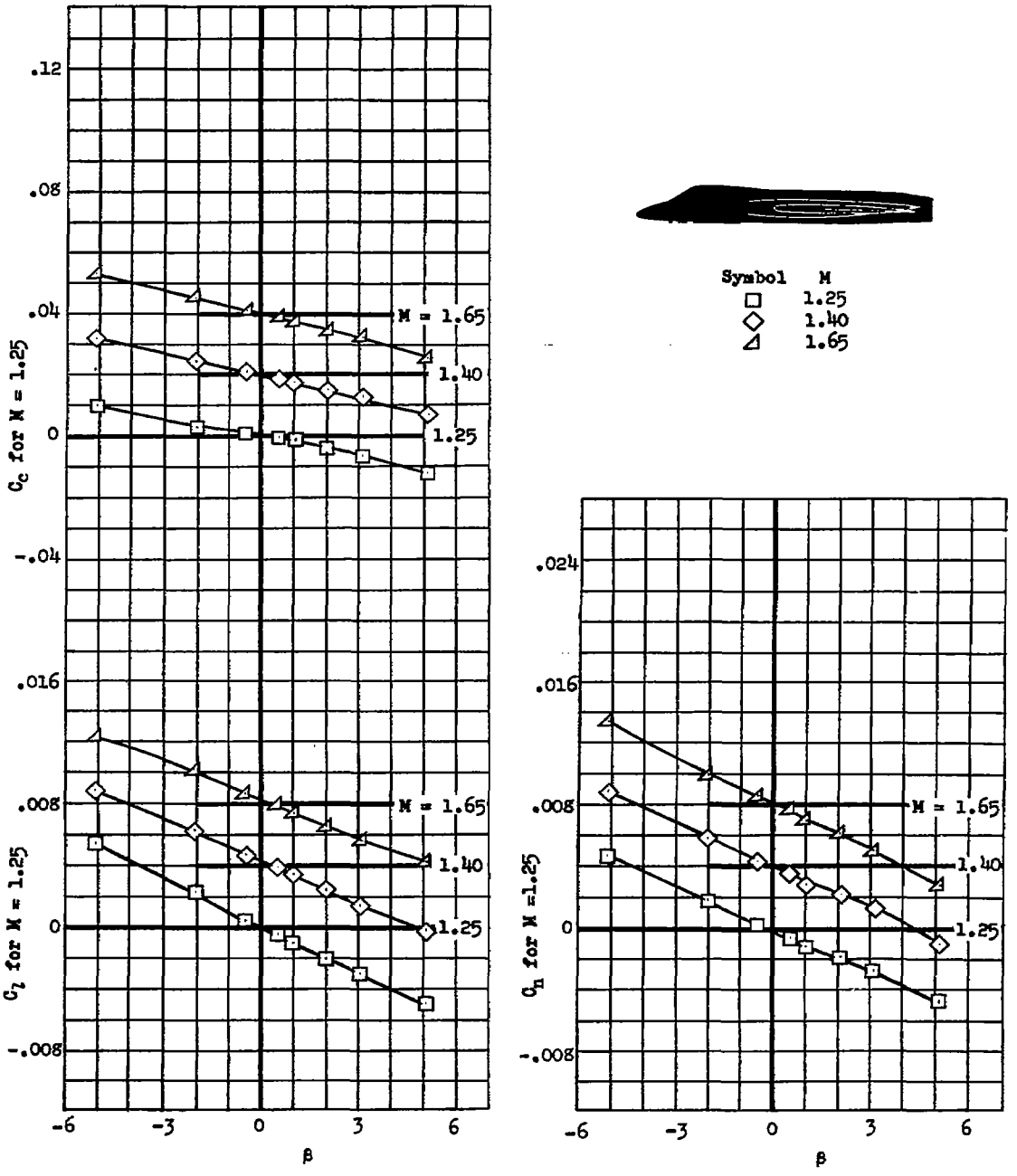

(d) Model without vertical tail; $\alpha = 5°$.

Figure 7.- Concluded.

[redacted]

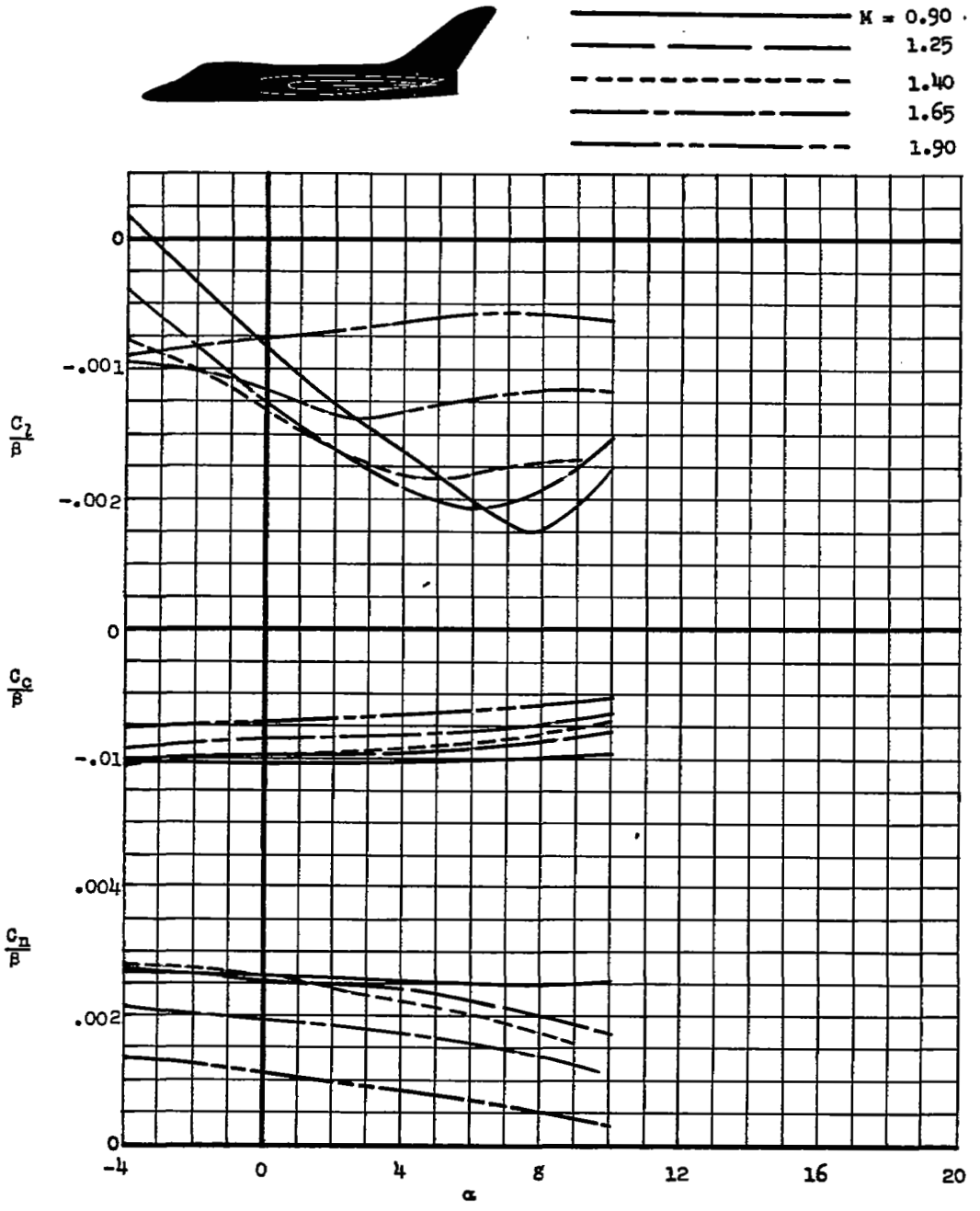

(a) Basic model.

Figure 8.- Variation of lateral-directional stability parameters C_l/β, C_c/β, and C_n/β with angle of attack for Model B.

[redacted]

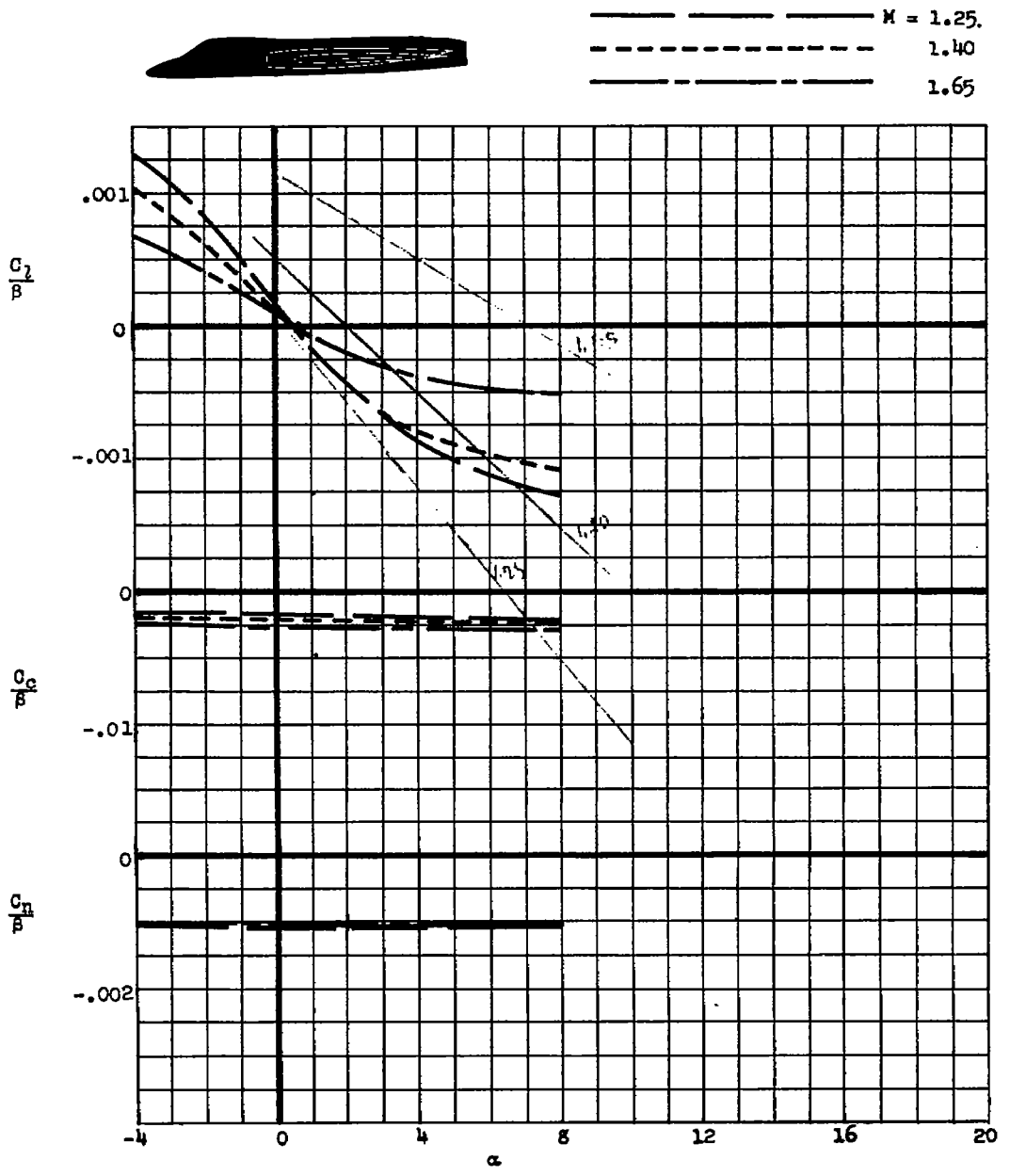

(b) Model without the vertical tail.

Figure 8.- Concluded.

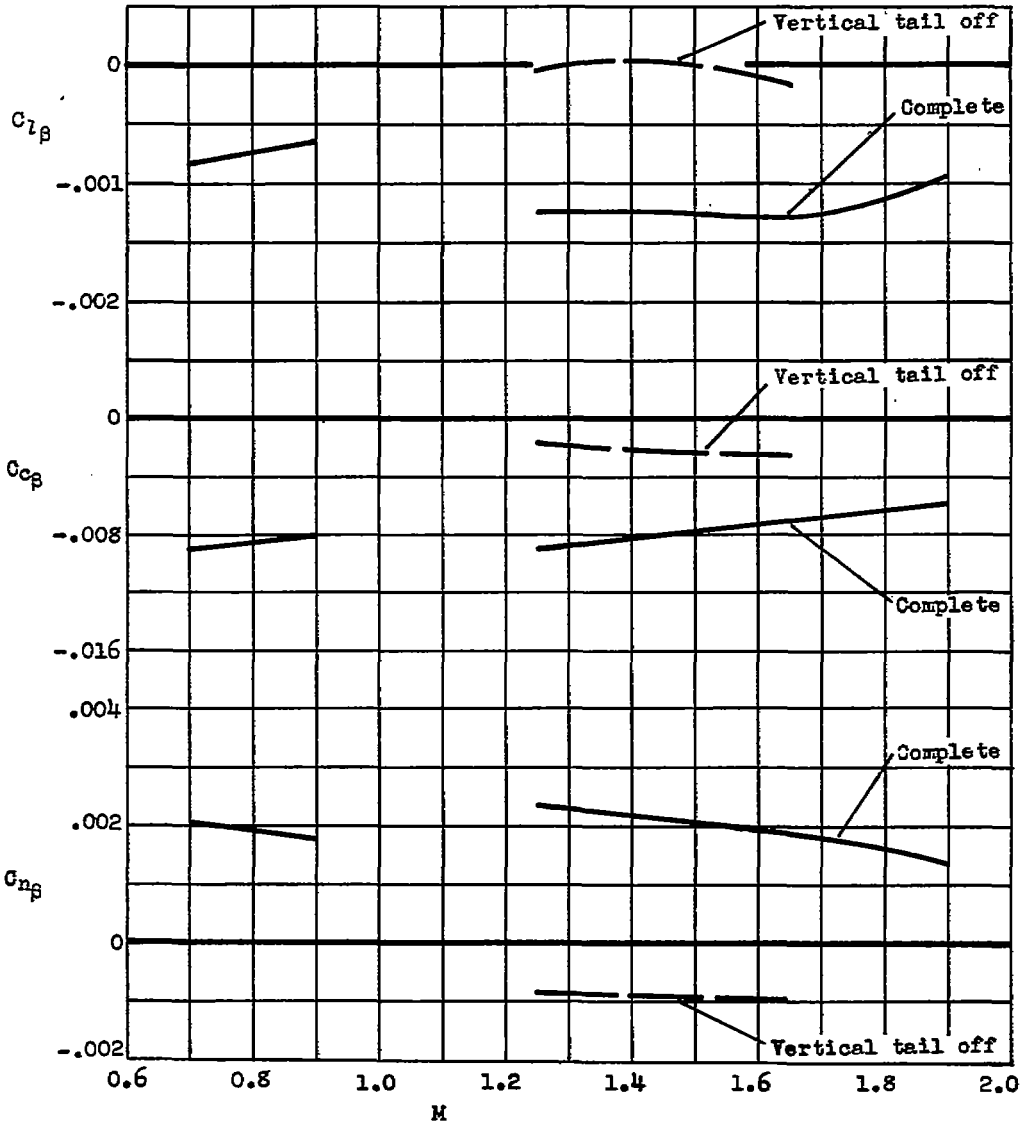

(a) $\alpha = 0^\circ$.

Figure 9.- Comparison of the lateral-directional stability derivatives of Model B with and without the vertical tail as functions of Mach number.

[redacted]

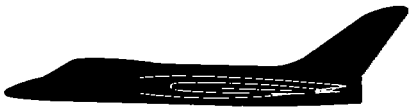

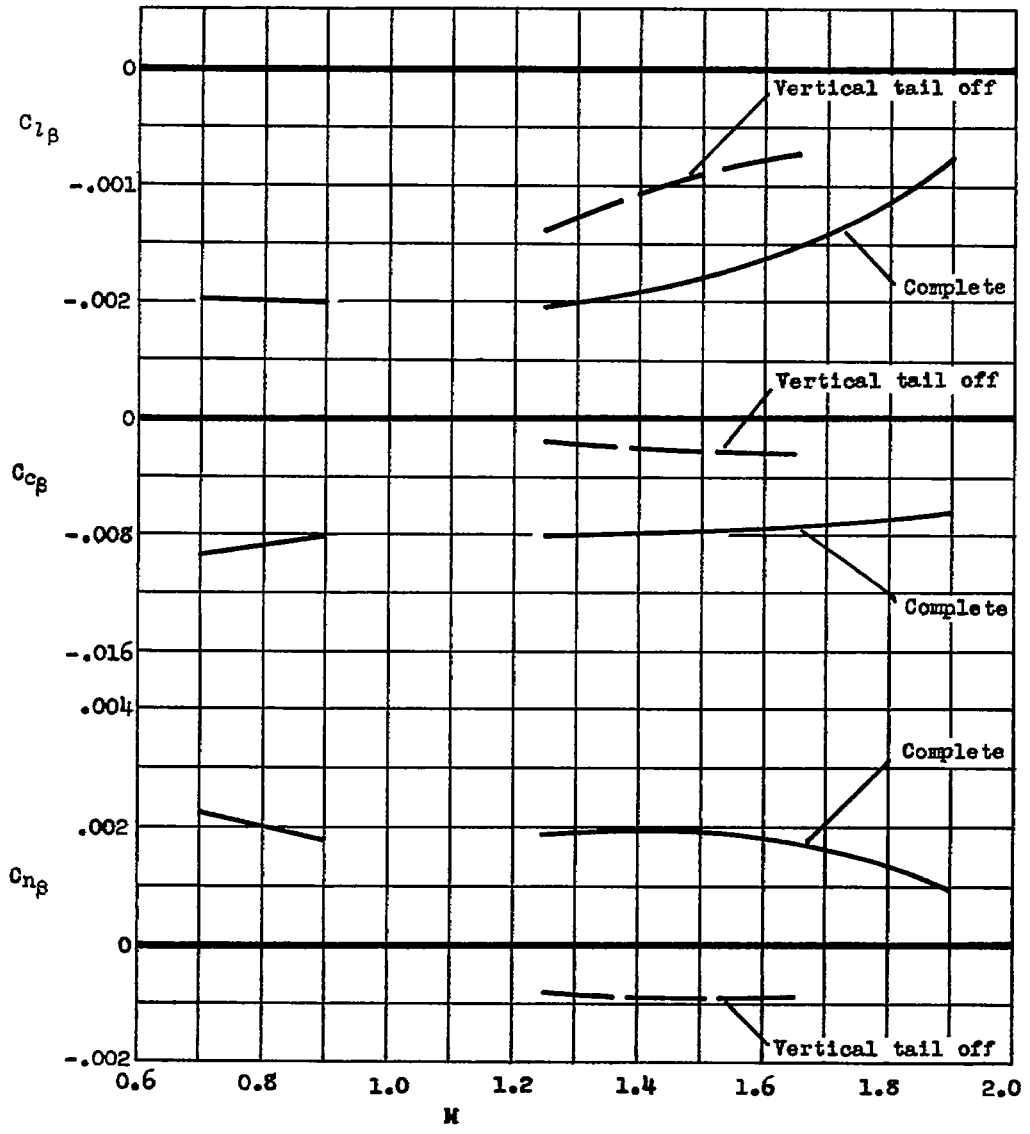

(b) $\alpha = 5^\circ$.

Figure 9.- Concluded.

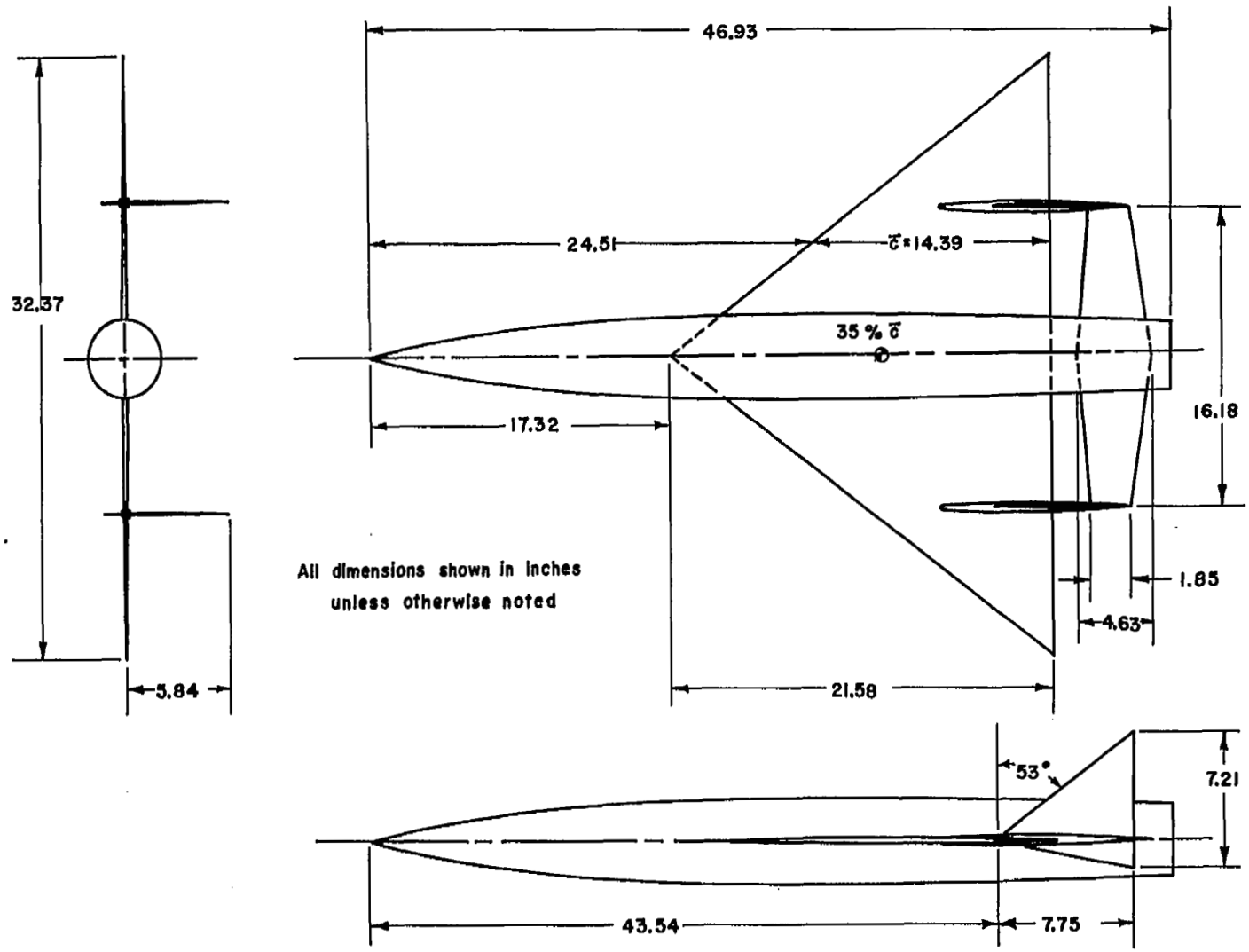

Figure 10.- Dimensional sketch of Model C.

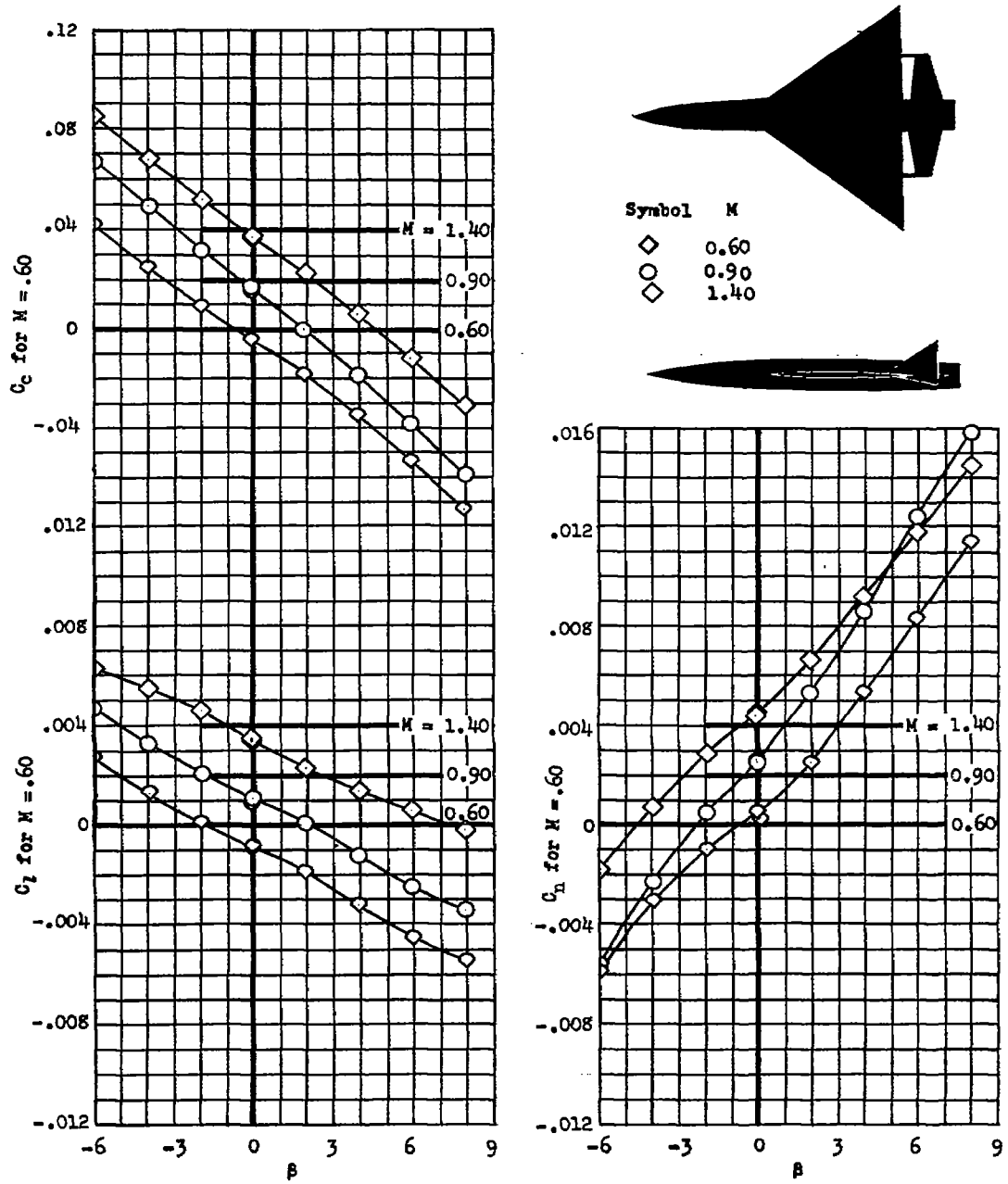

(a) $\alpha = 0^{\circ}$.

Figure 11.- Variation of lateral-directional stability characteristics with angle of sideslip for Model C at different angles of attack.

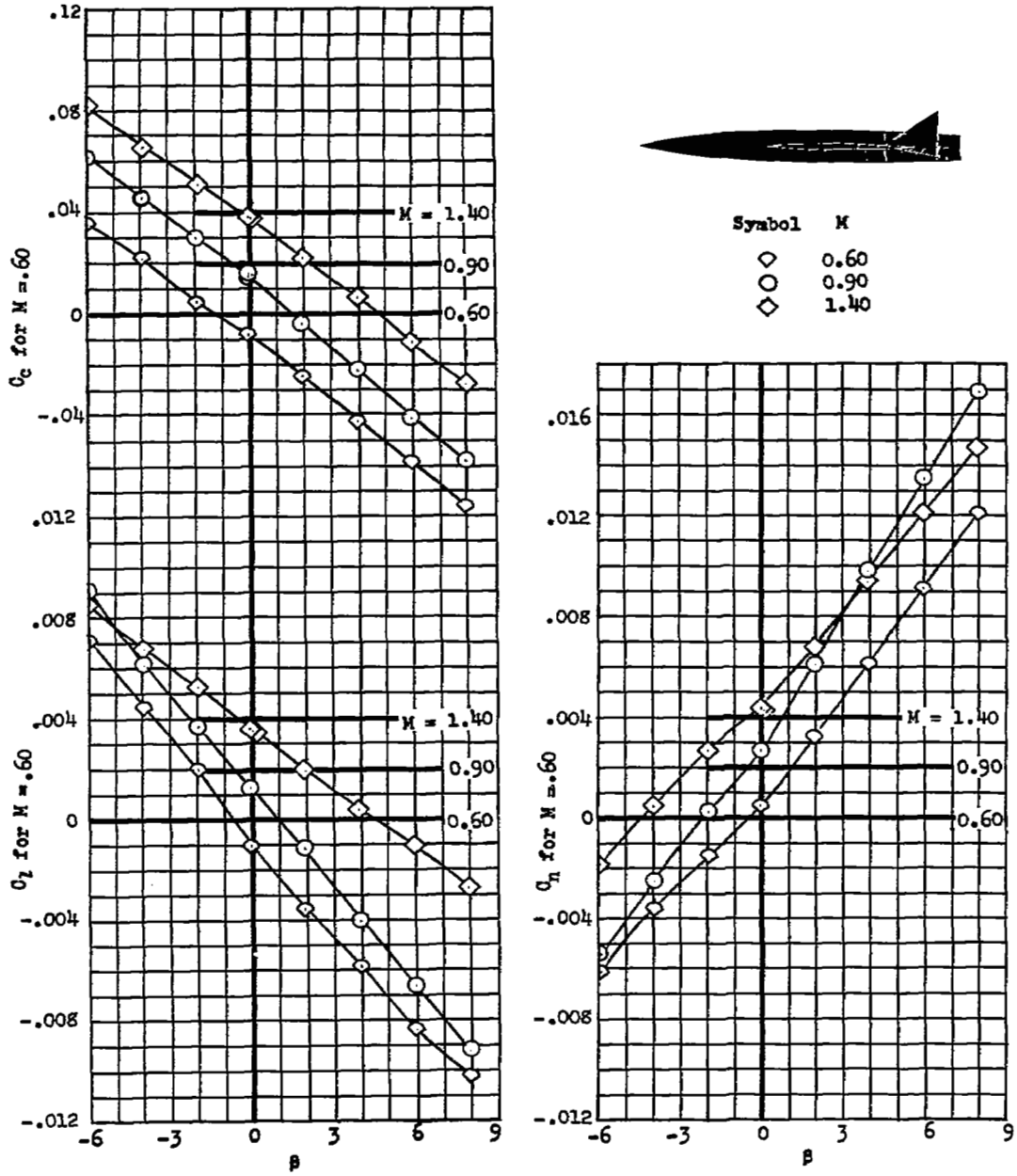

(b) $\alpha = 5^{\circ}$.

Figure 11.- Continued.

[redacted]

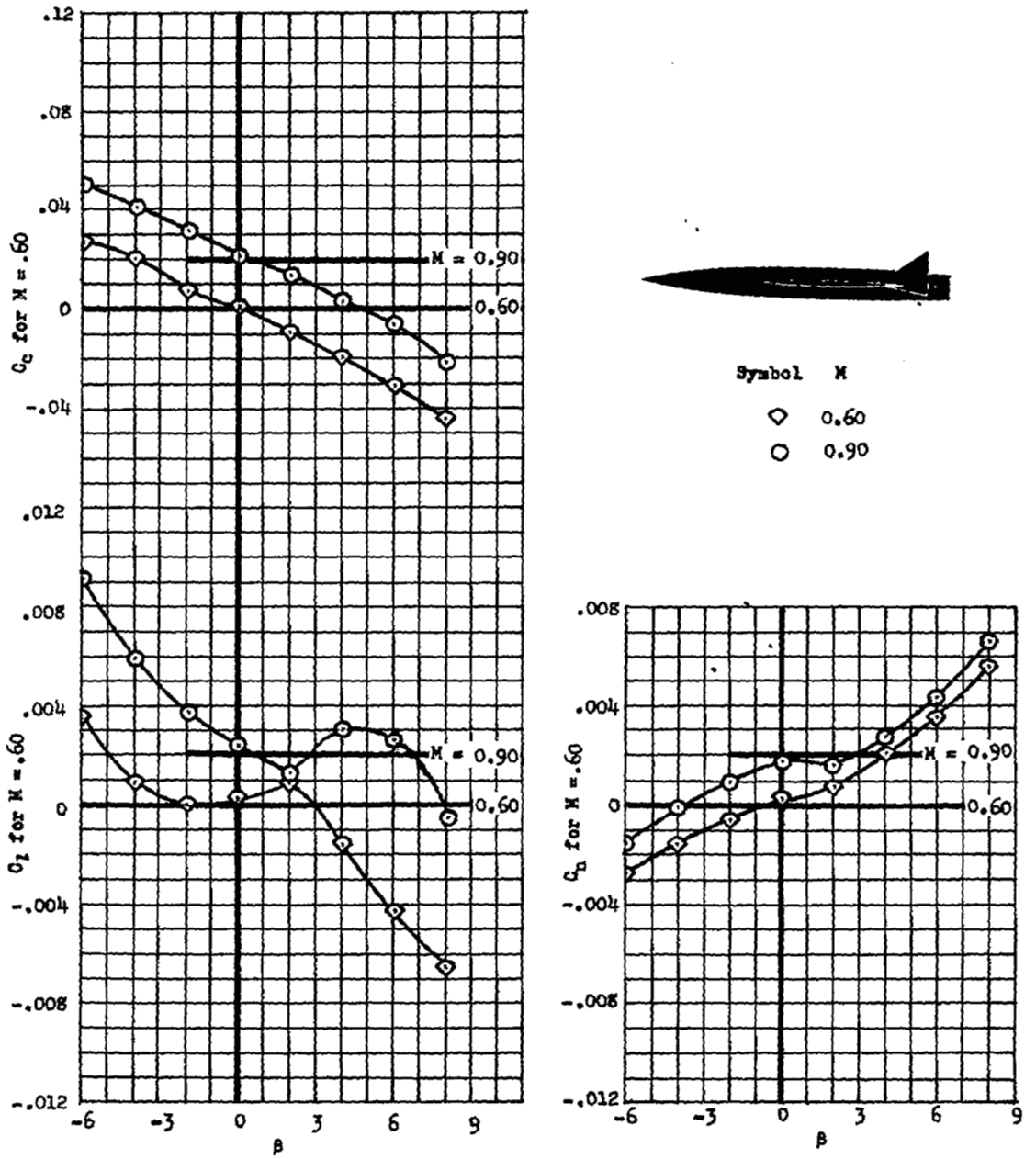

(c) $\alpha = 10^{\circ}$.

Figure 11.- Concluded.

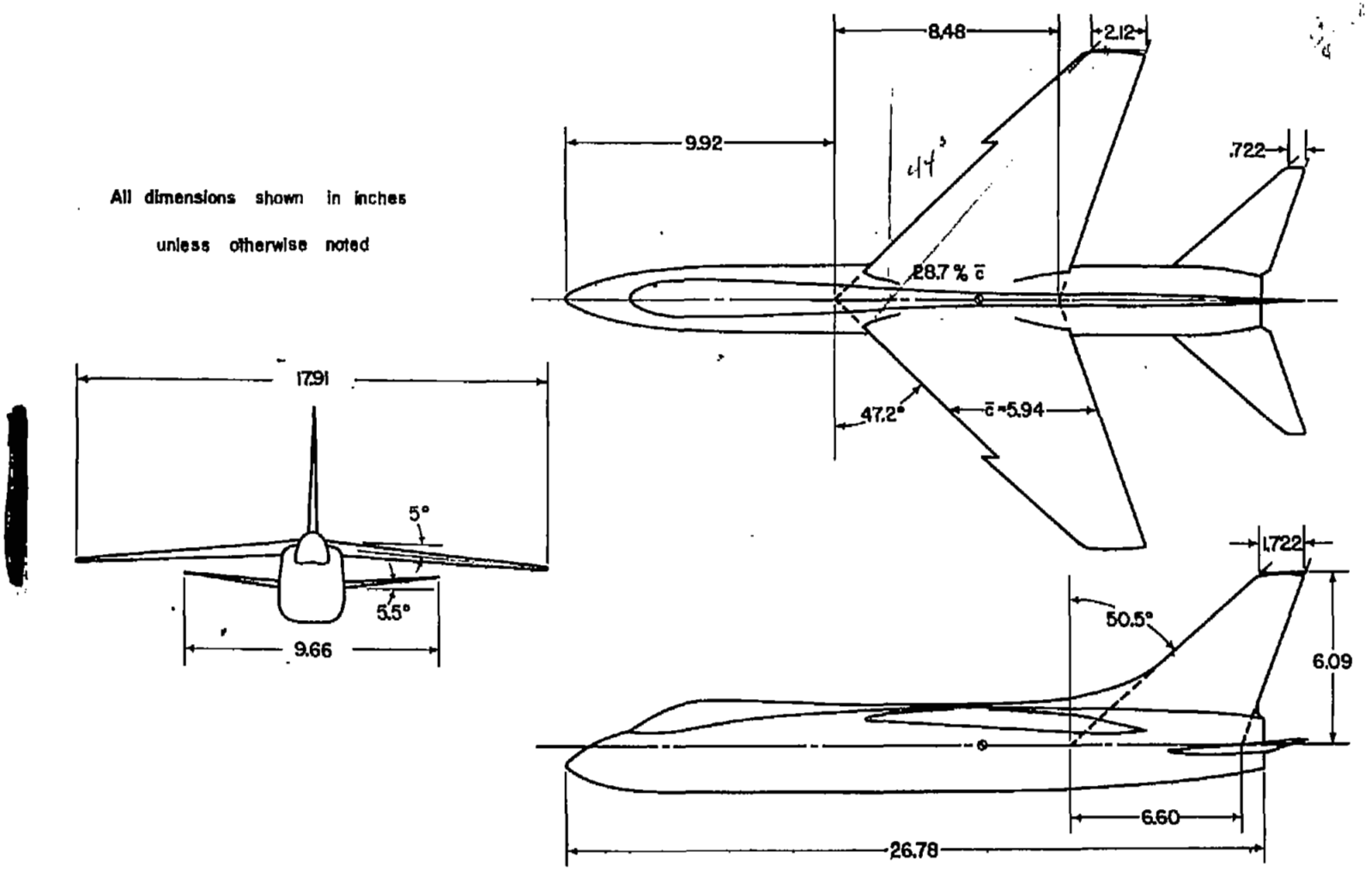

Figure 12.- Dimensional sketch of Model D.

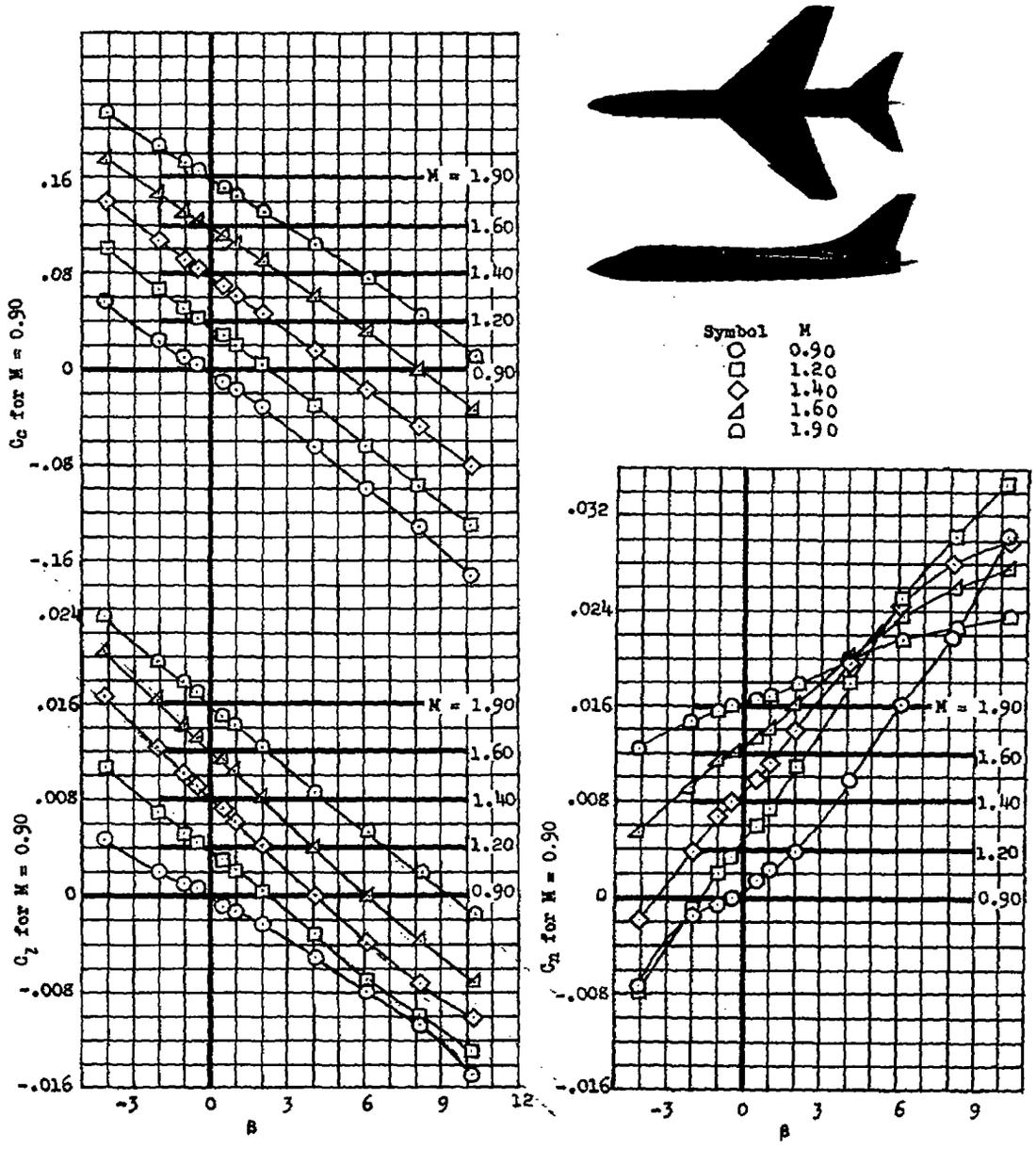

(a) Basic model; $\alpha = 0^{\circ}$.

Figure 13.- Variation of lateral-directional stability characteristics with angle of sid slip for Model D with various modifications.

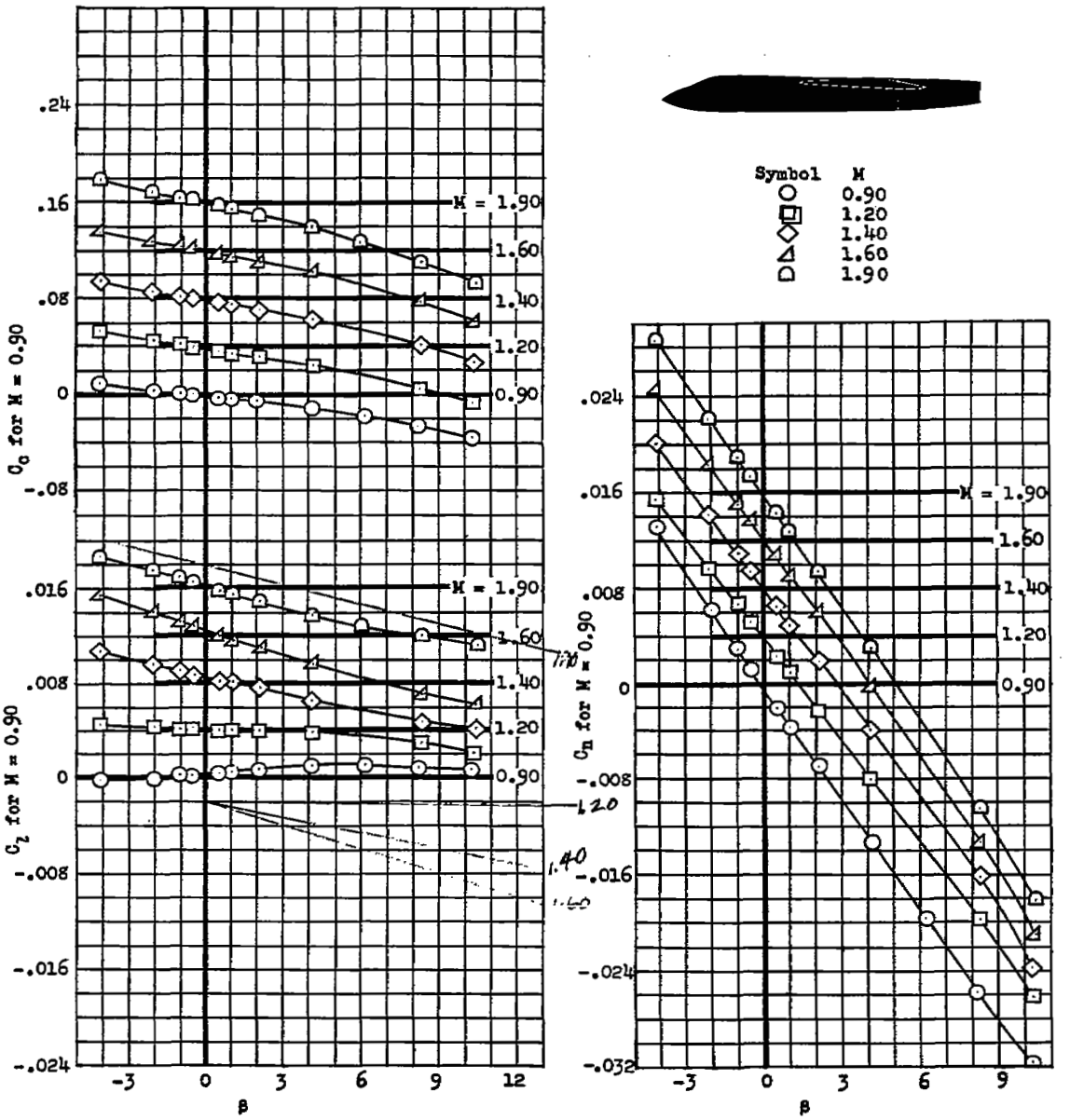

(b) Model without vertical or horizontal tail; $\alpha = 0^{\circ}$.

Figure 13.- Continued.

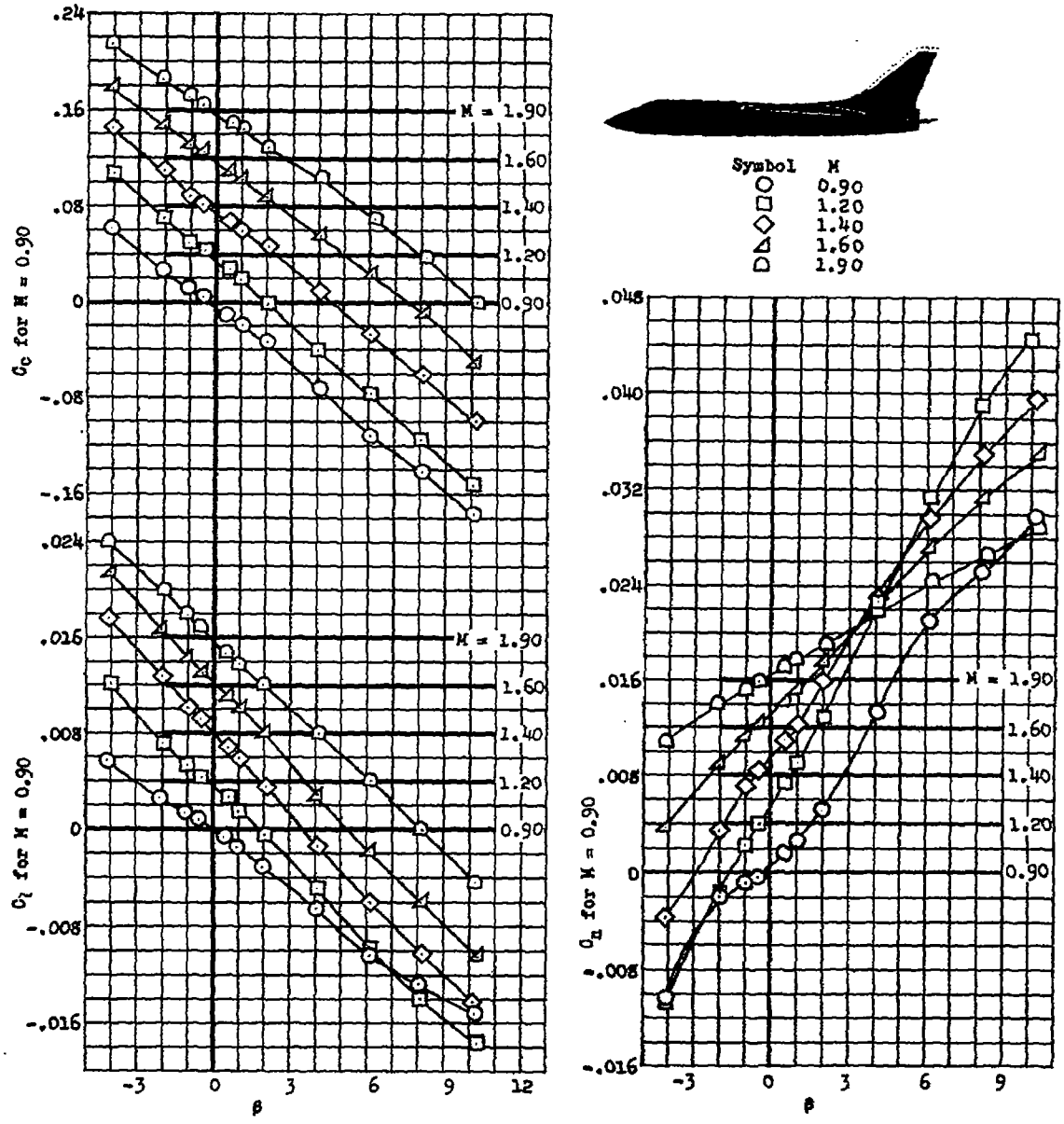

(c) Model with large area vertical tail; $\alpha = 0^{\circ}$.

Figure 13.- Continued.

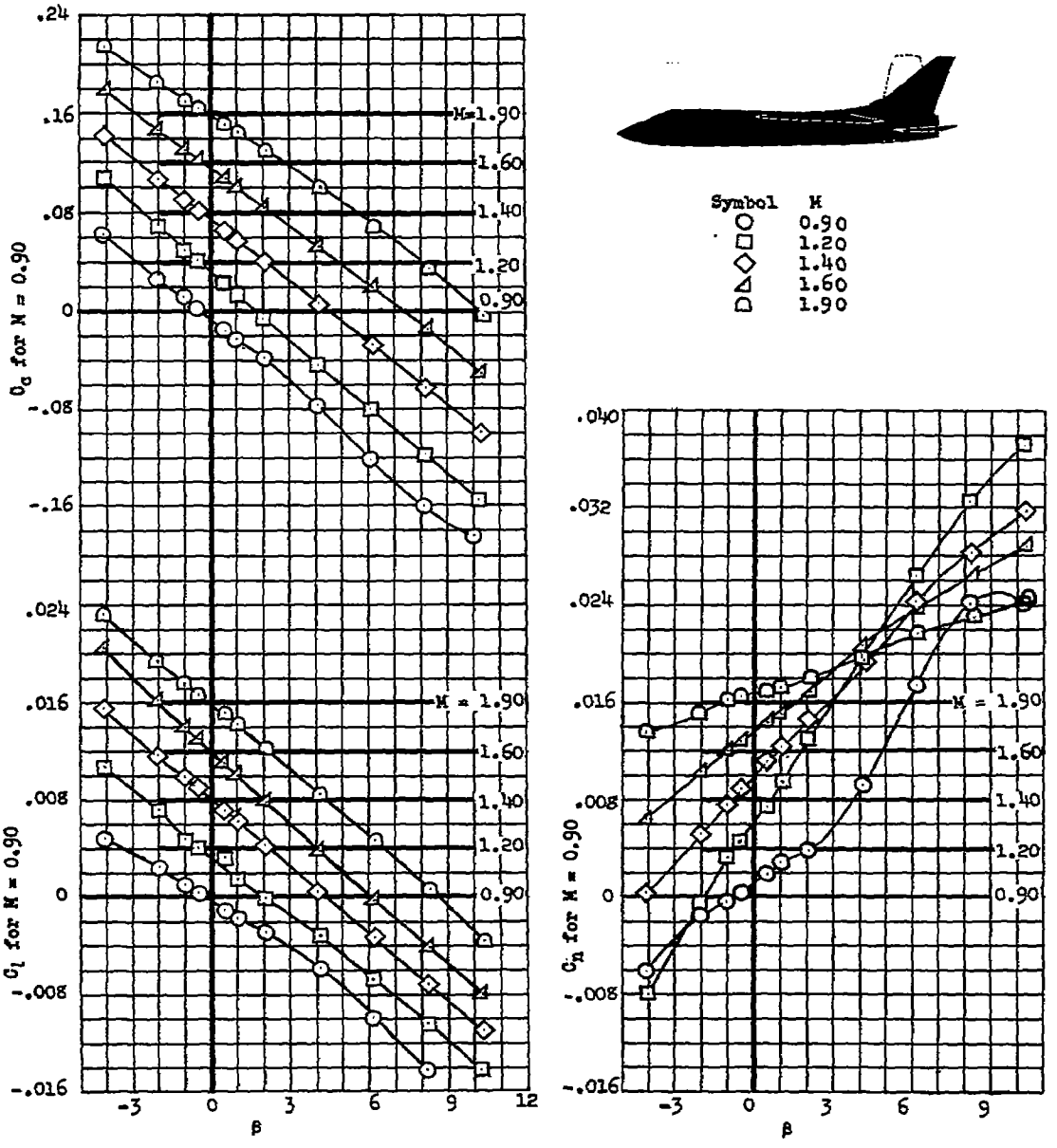

(d) Model with unswept vertical tail; $\alpha = 0^{\circ}$.

Figure 13.- Continued.

[redacted]

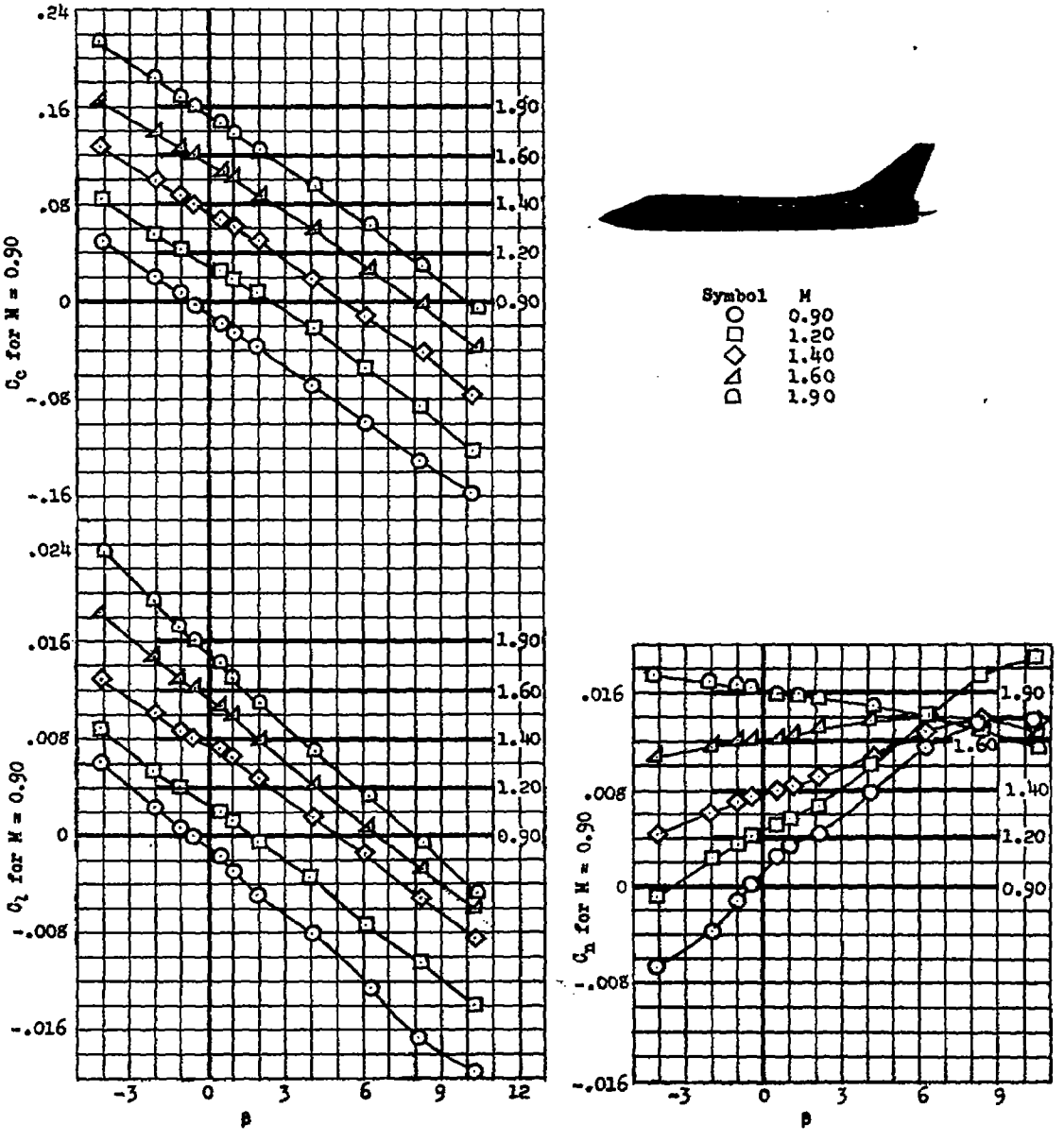

(e) Basic model; $\alpha = 10^{\circ}$.

Figure 13.- Continued.

[redacted]

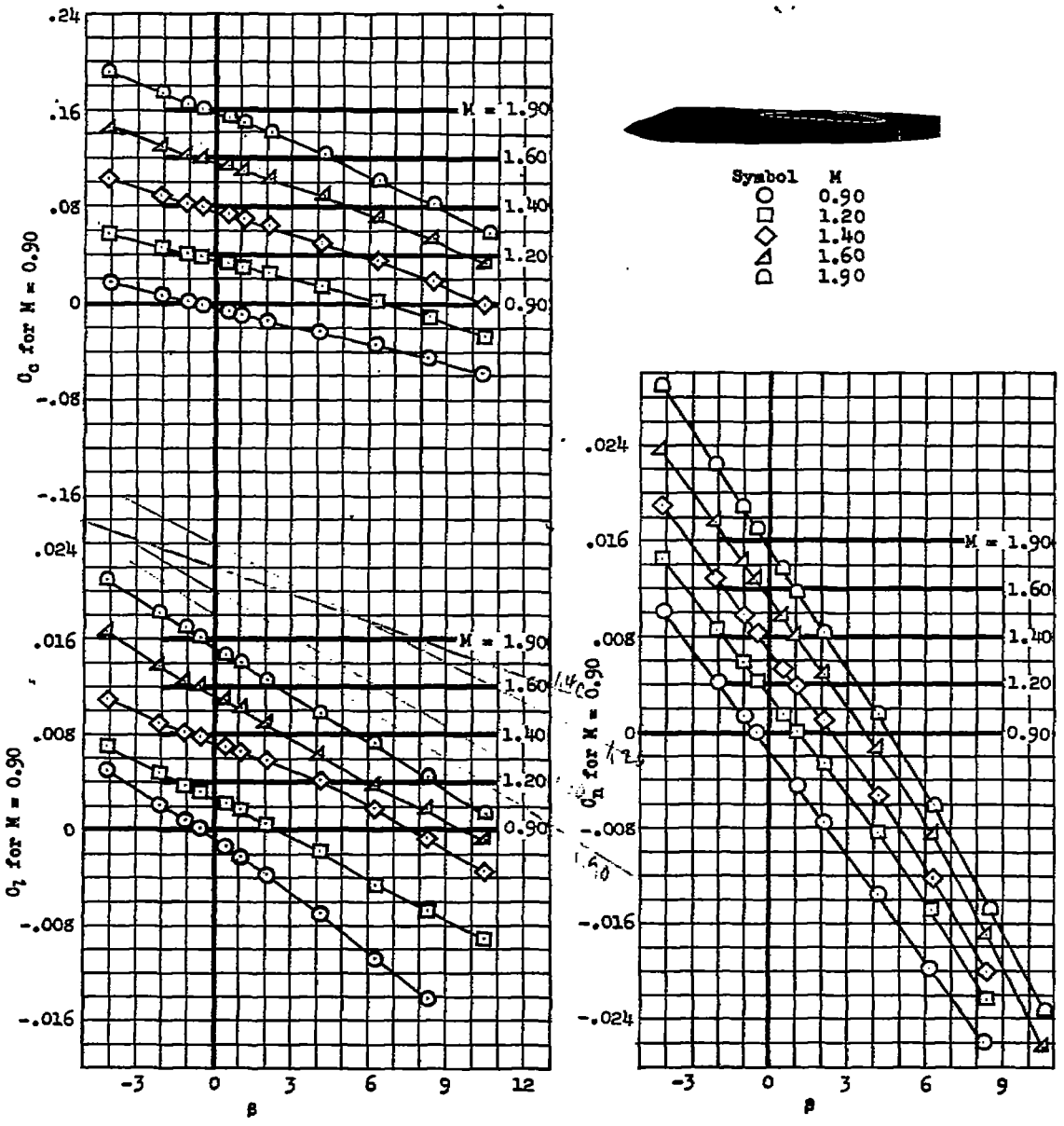

(f) Model without vertical or horizontal tail; $\alpha = 10^{\circ}$.

Figure 13.- Concluded.

[redacted]

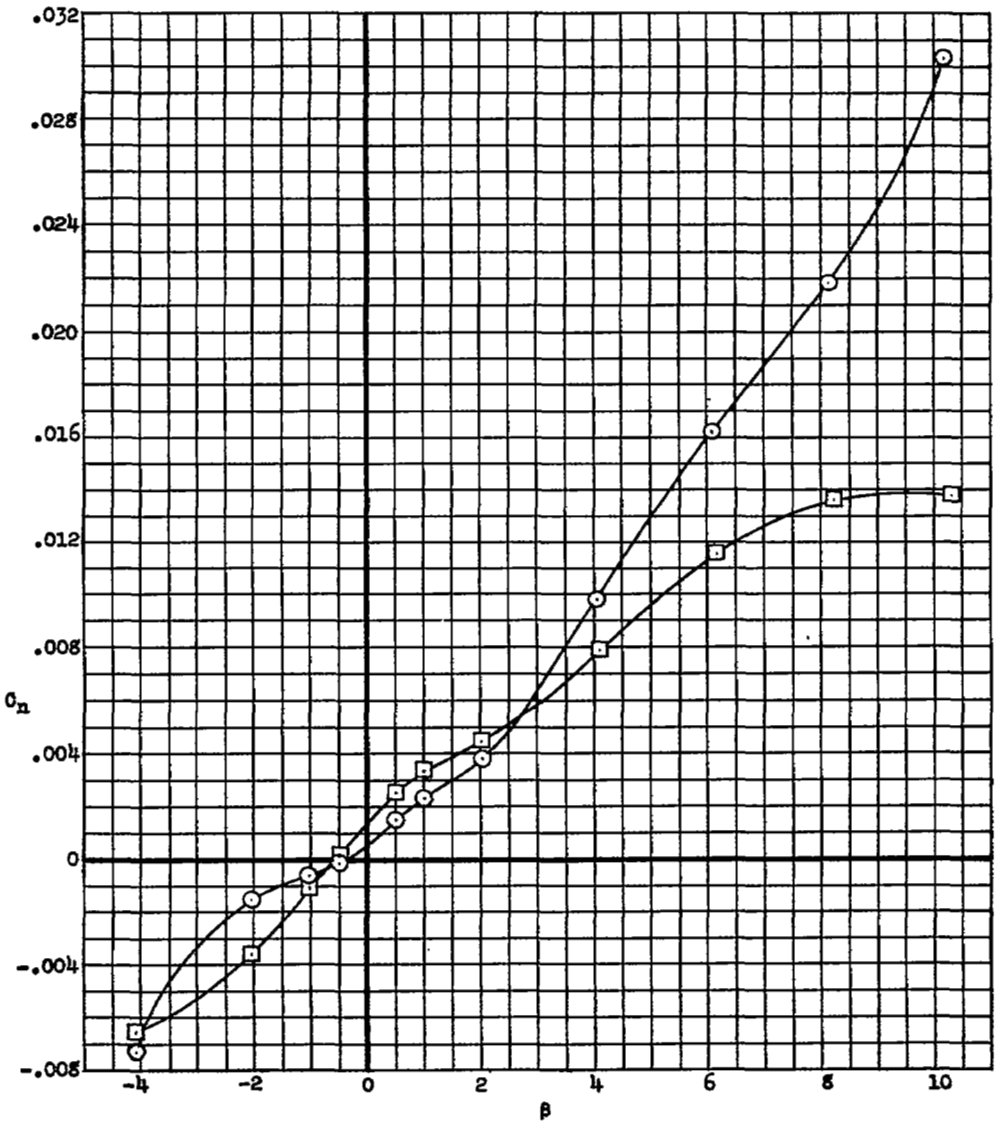

(a) M = 0.90

Figure 14.- Variation of the yawing-moment coefficient, C_n, with angle of sideslip for Model D at two angles of attack.

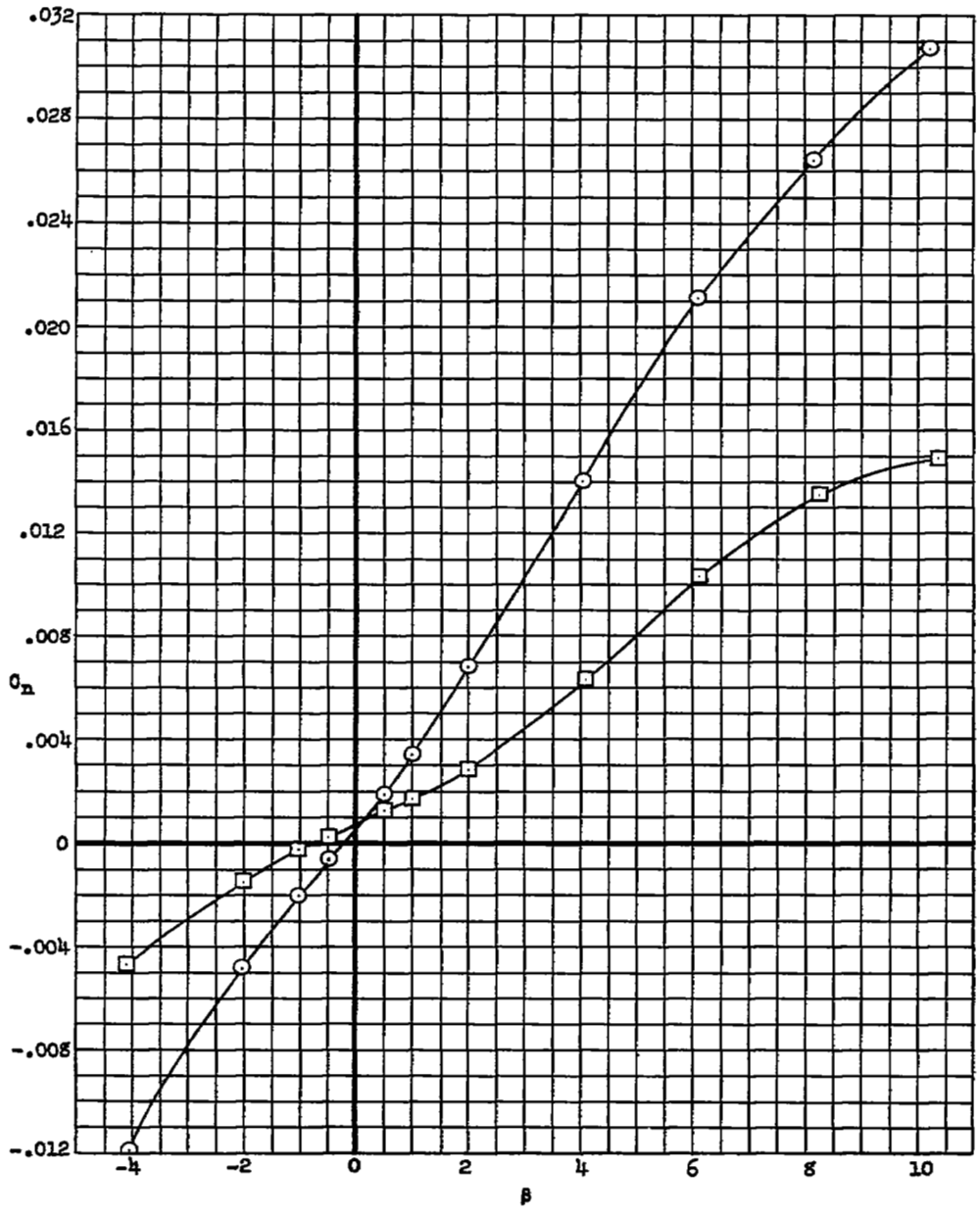

(b) M = 1.20

Figure 14.- Continued.

[redacted]

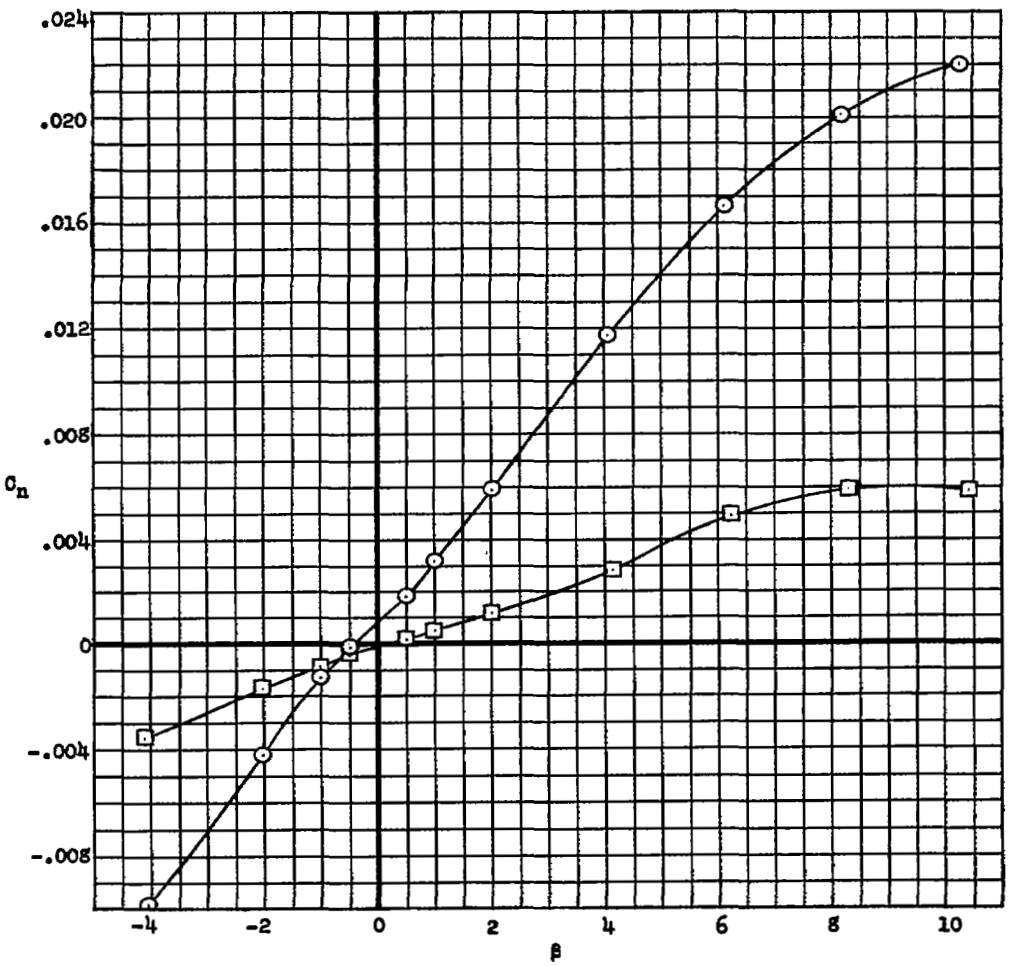

(c) M= 1.40

Figure 14.- Continued.

[redacted]

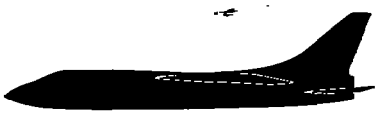

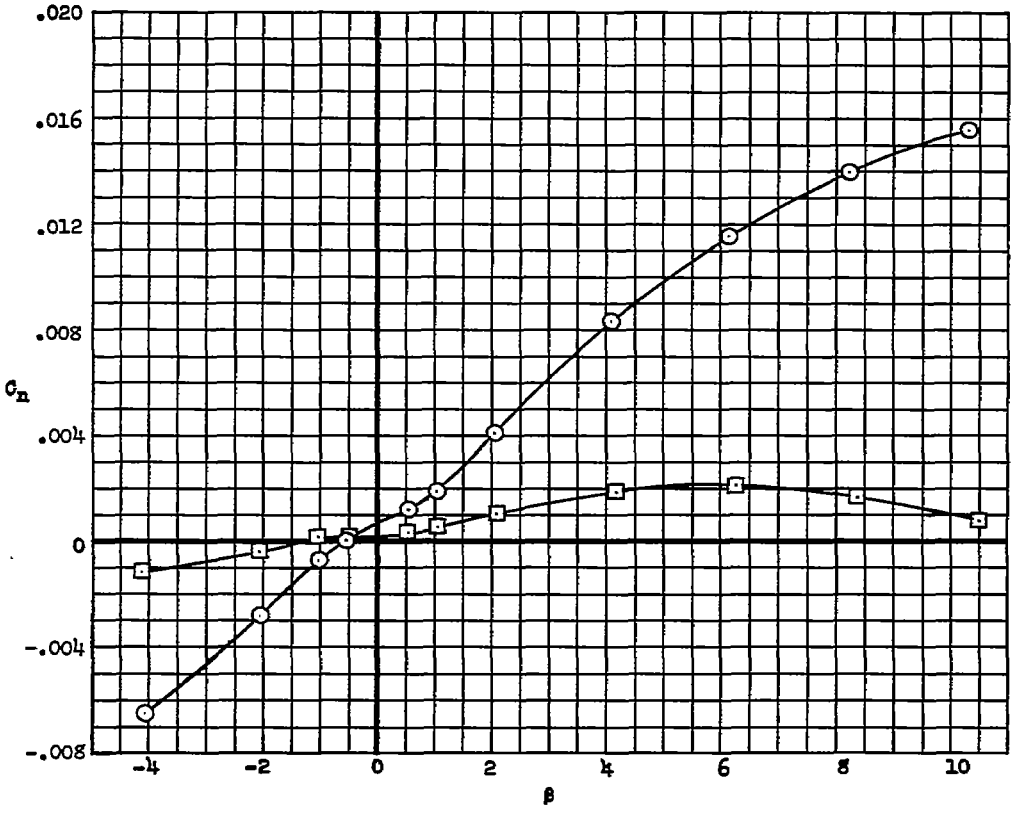

(d) M = 1.60

Figure 14.- Continued.

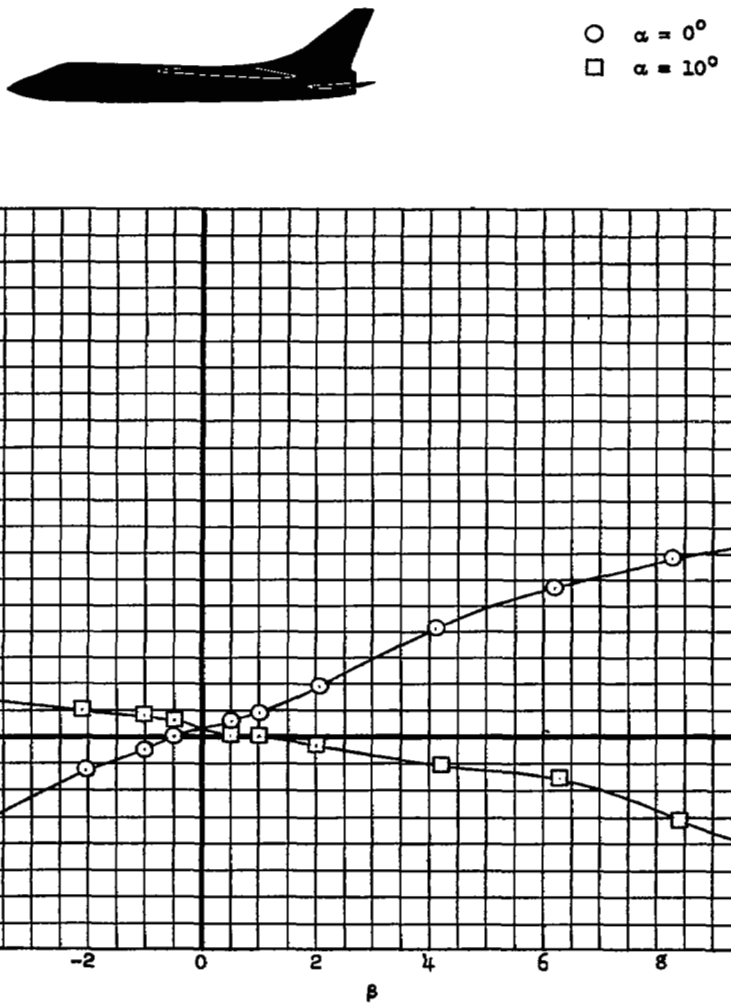

(e) M = 1.90

Figure 14.- Concluded.

[redacted]

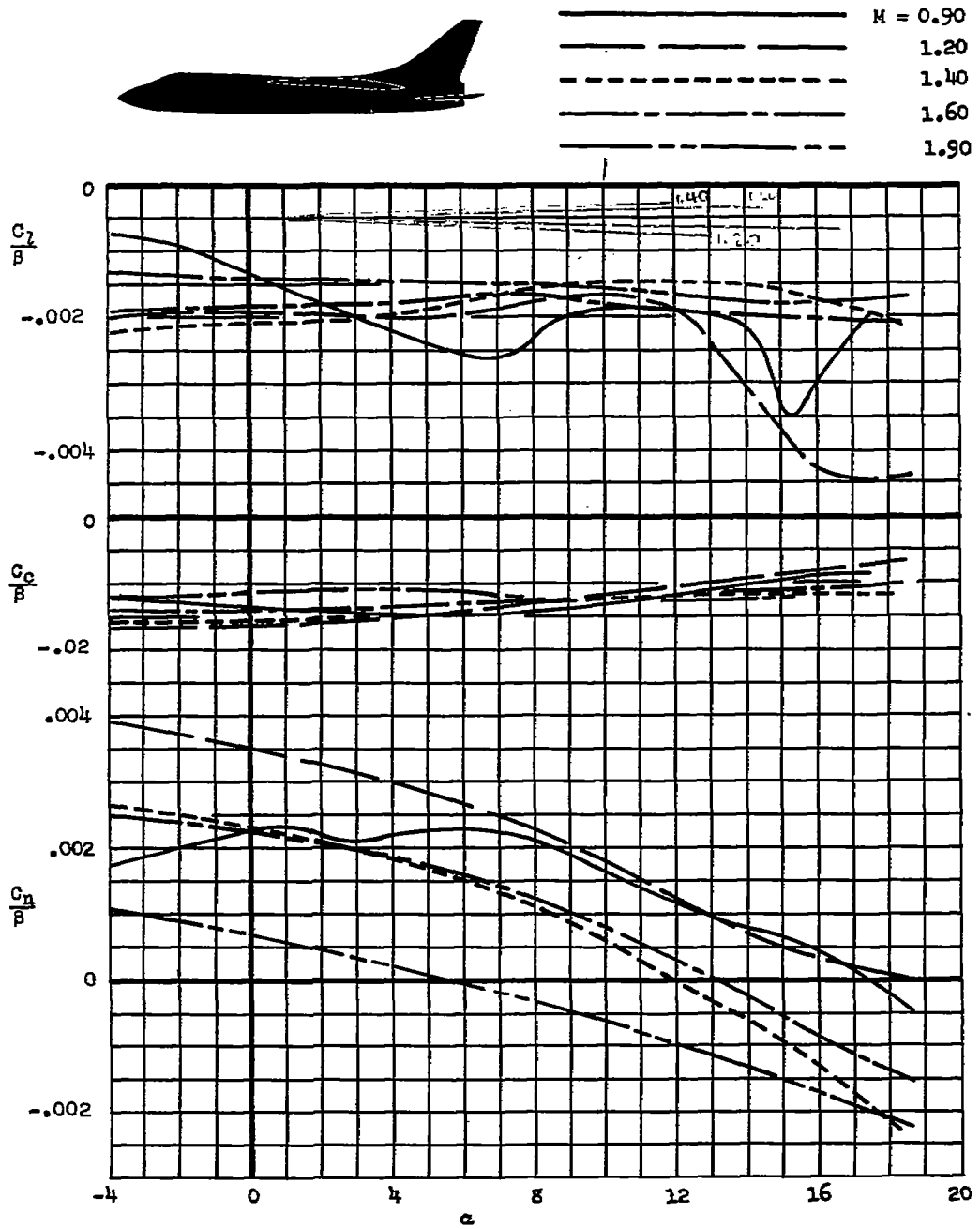

(a) Basic model.

Figure 15.- Variation of lateral-directional stability parameters C_l/β, C_c/β, and C_n/β with angle of attack for Model D with various modifications.

[redacted]

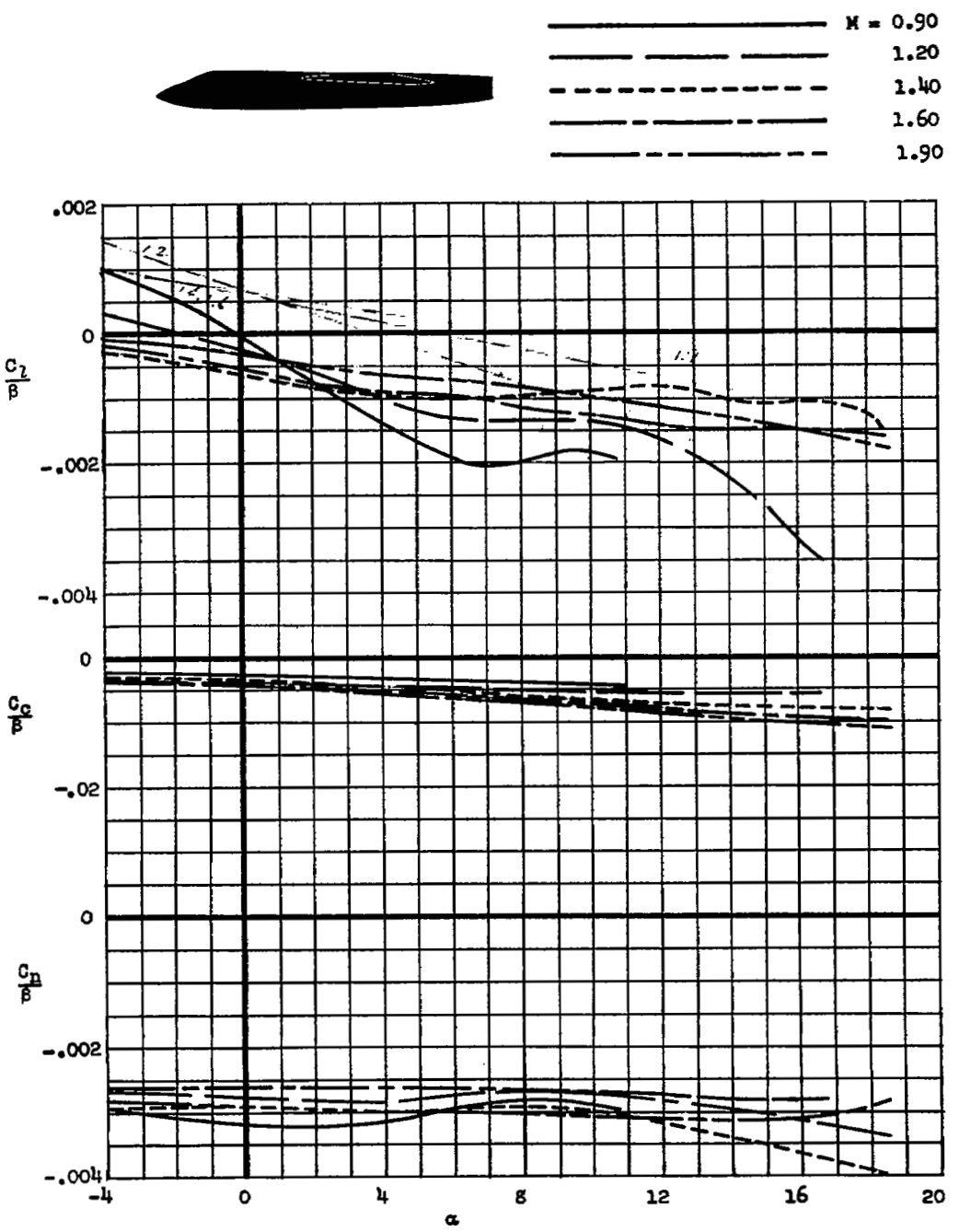

(b) Model without vertical and horizontal tail.

Figure 15.- Continued.

M = 0.90
1.20
1.40
1.60
1.90

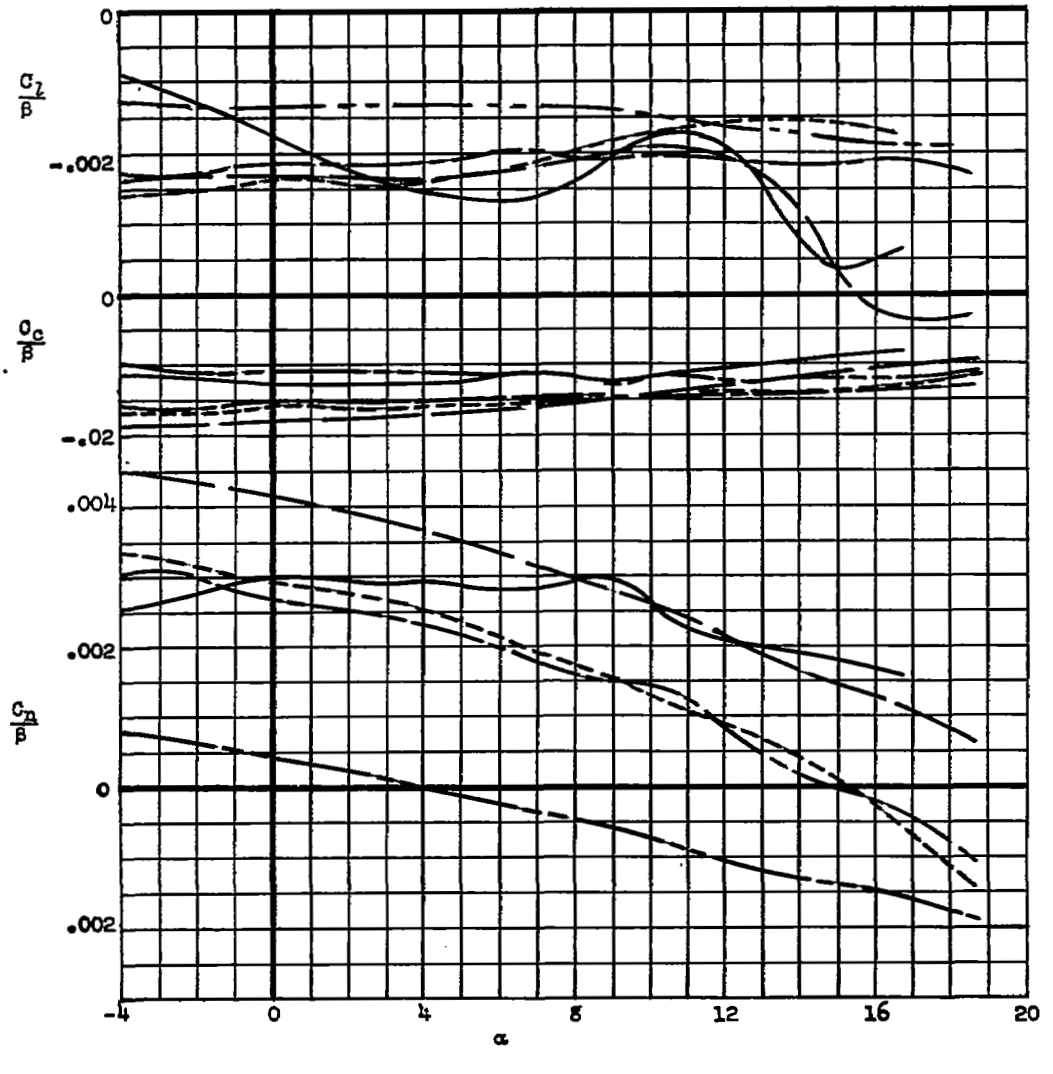

(c) Model with tall vertical tail.

Figure 15.- Continued.

[redacted]

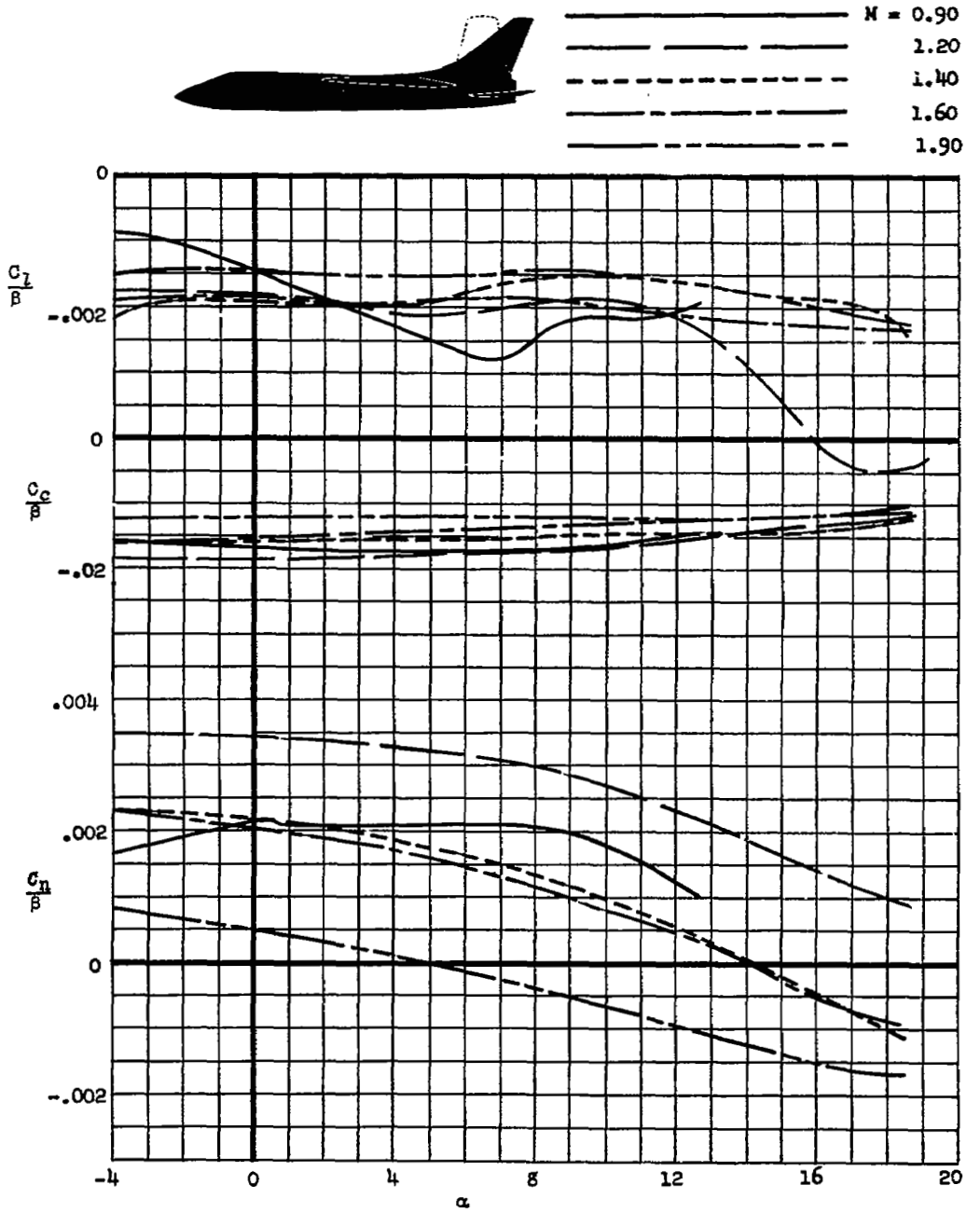

(d) Model with unswept vertical tail.

Figure 15.- Continued.

[redacted]

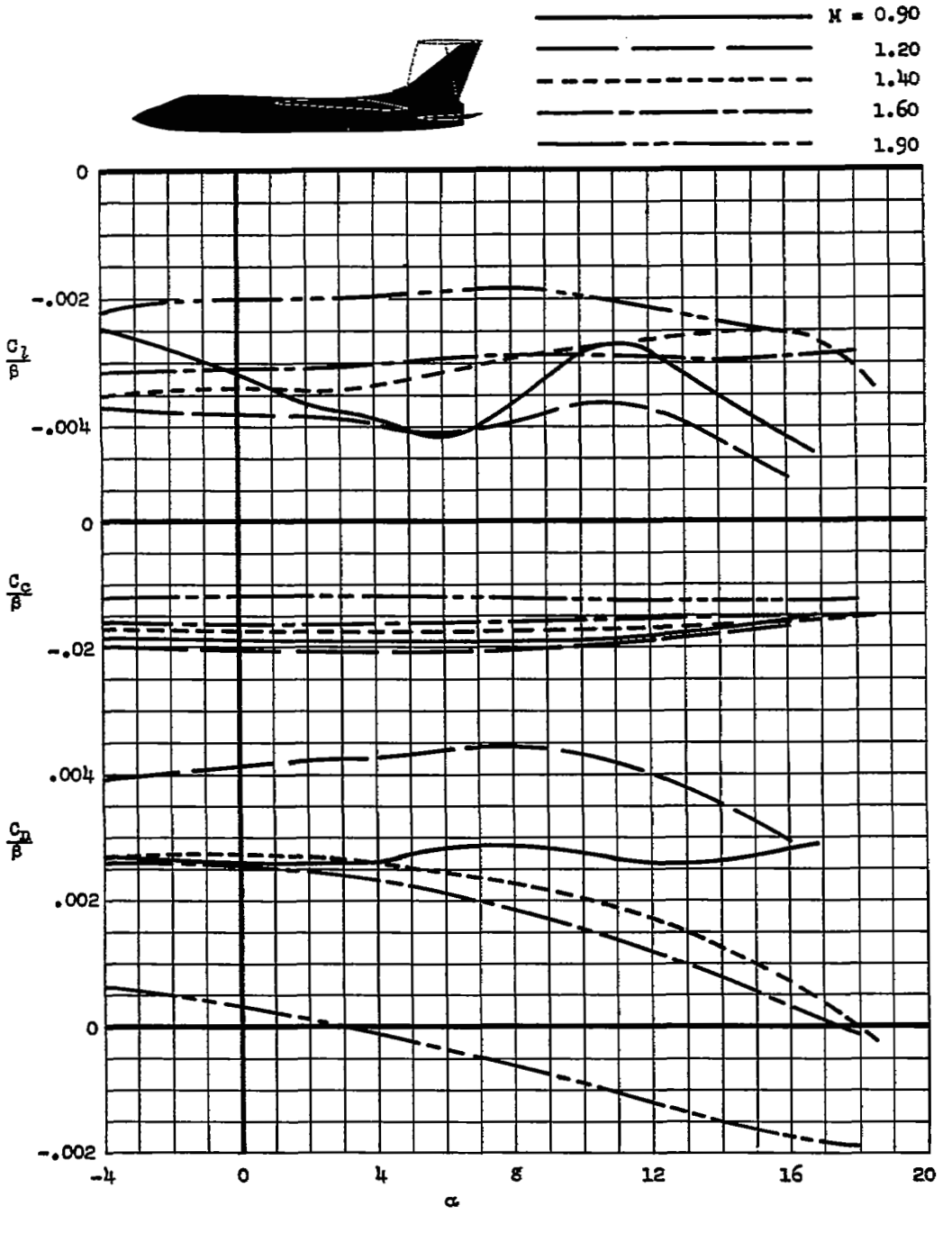

(e) Model with horizontal tail placed high on the unswept vertical tail.

Figure 15.- Continued.

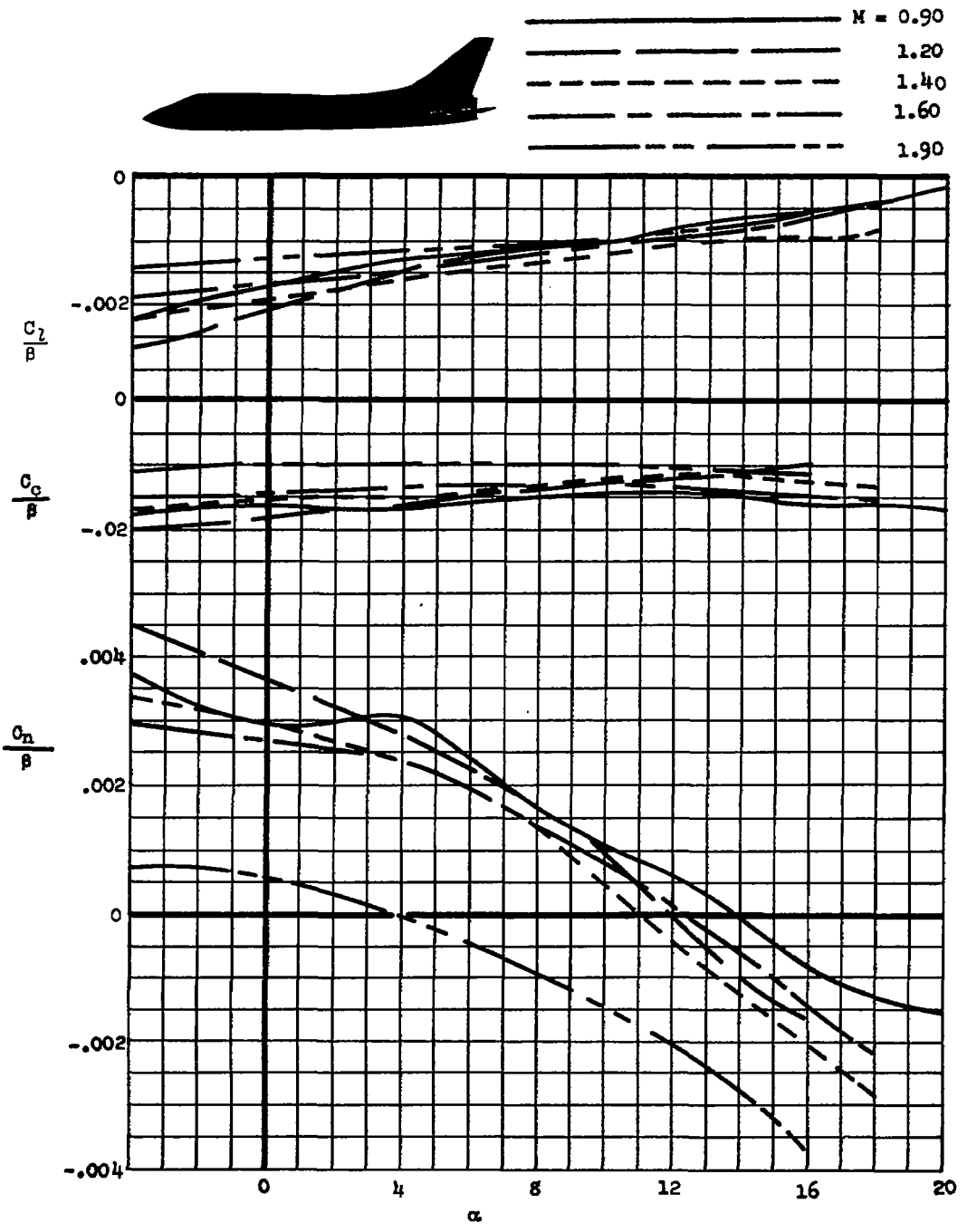

(f) Model less wing.

Figure 15.- Continued.

[redacted]

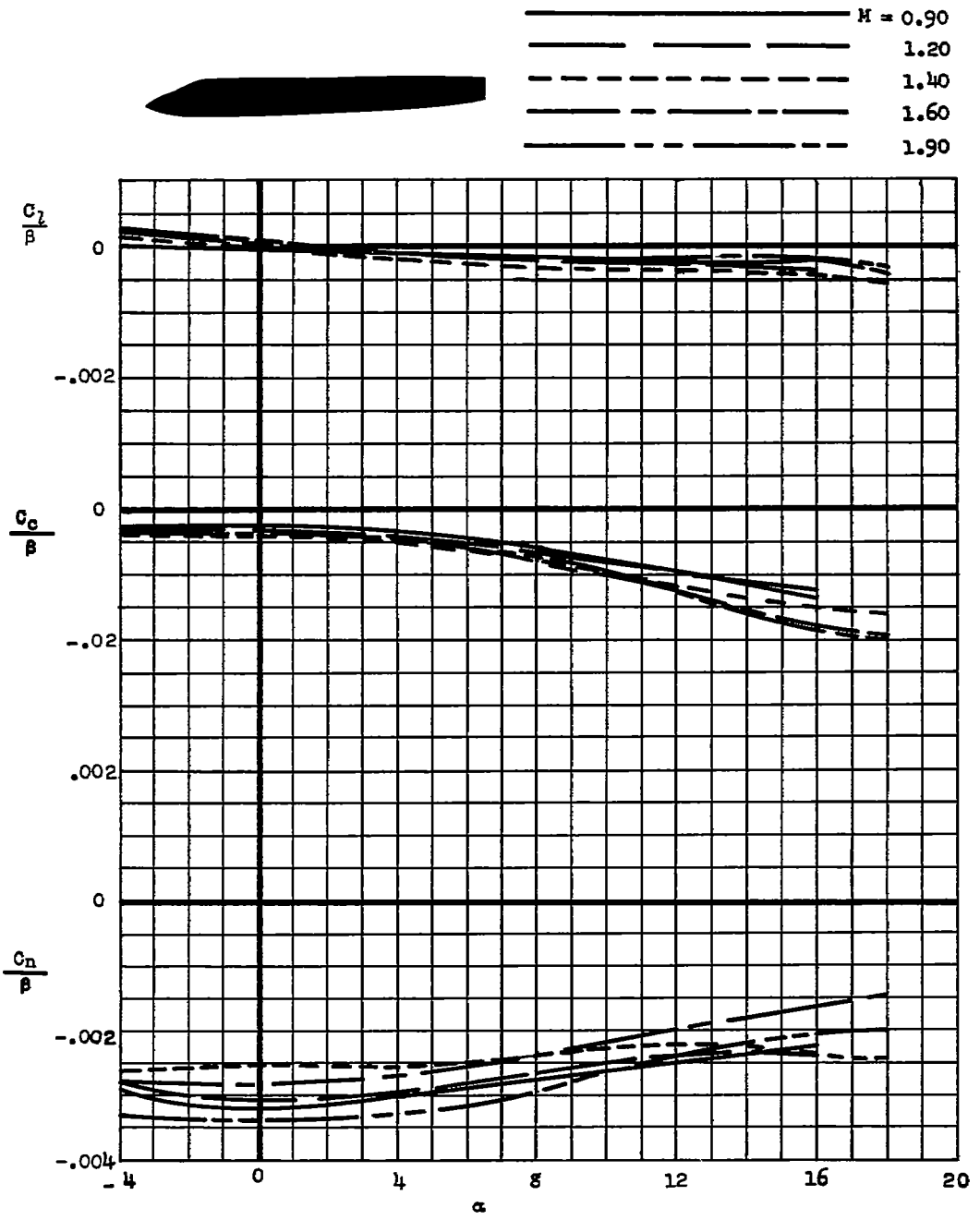

(g) Model less wing and empennage.

Figure 15.- Concluded.

[redacted]

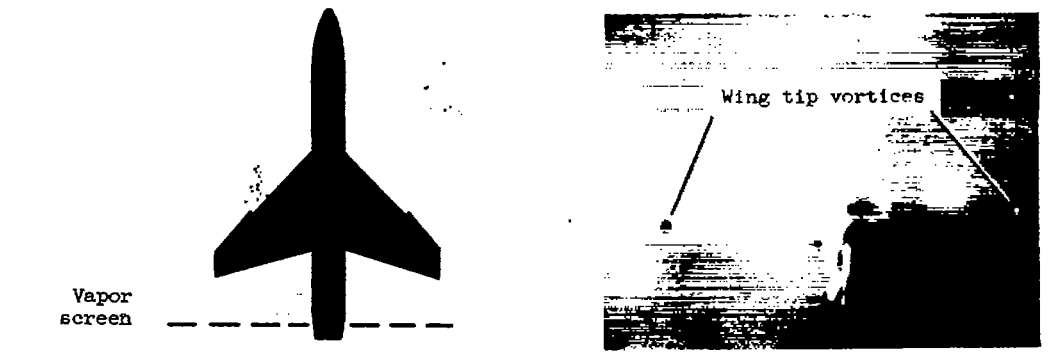

(a) $\alpha = 6^\circ$, $\beta = 5^\circ$

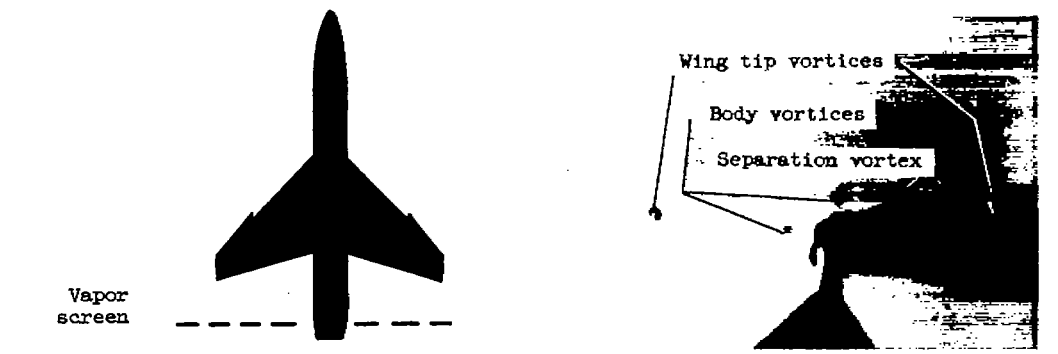

(b) $\alpha = 12^\circ$, $\beta = 5^\circ$

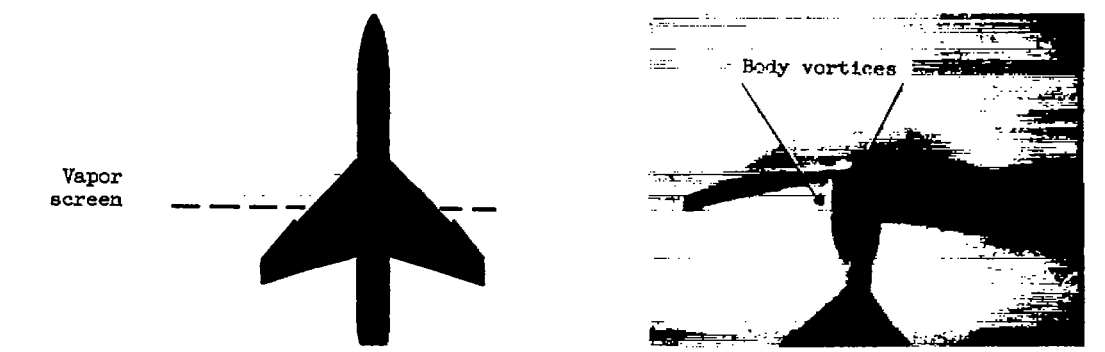

(c) $\alpha = 12^\circ$, $\beta = 5^\circ$ A-20030-1

Figure 16.- Vapor screen study of Model D; model less vertical and horizontal tail; Mach number 1.90.

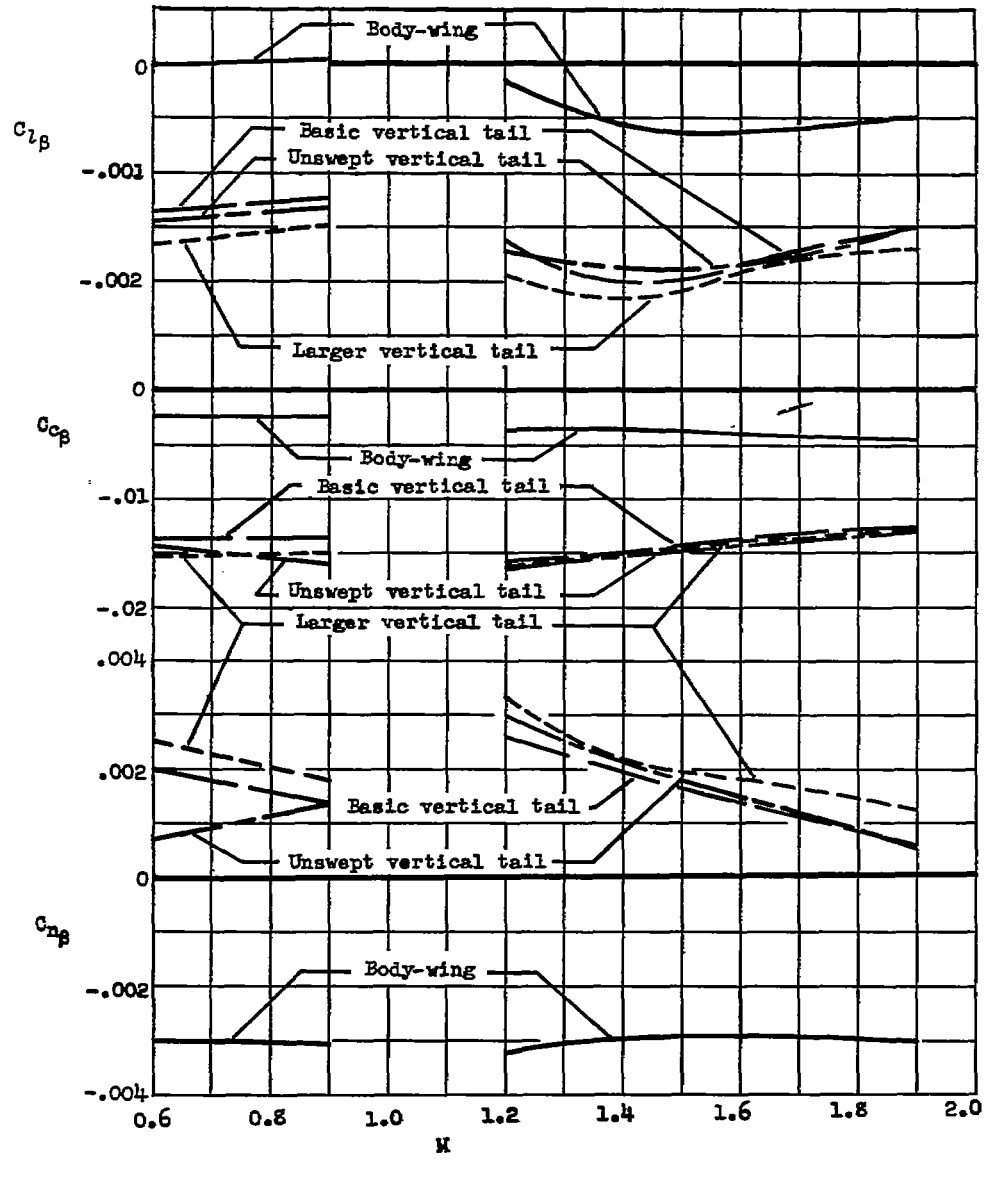

(a) Body-wing model; model with basic vertical tail, unswept vertical tail, and larger vertical tail; $\alpha = 0^{\circ}$.

Figure 17.- Comparison of the lateral-directional stability derivatives of Model D with various modifications as functions of Mach number.

[redacted]

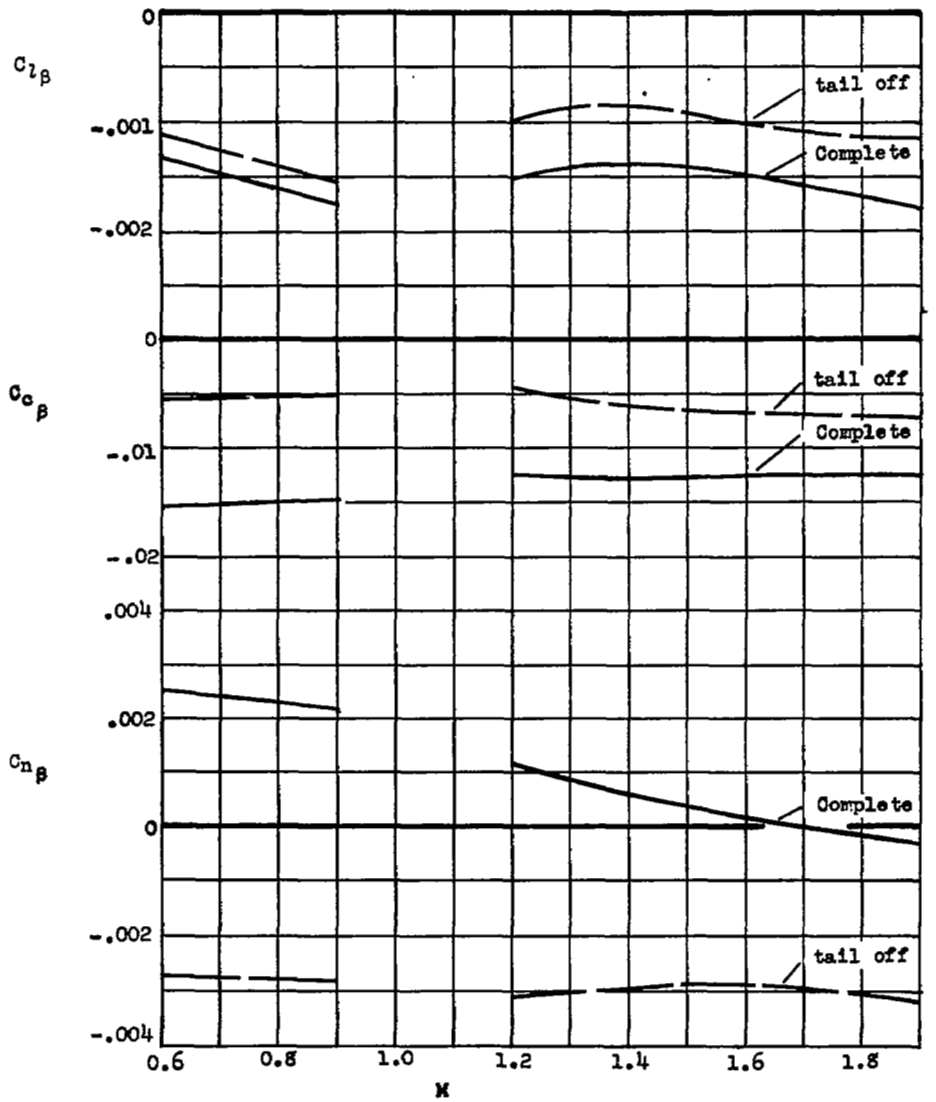

(b) Body-wing model and basic model; $\alpha = 10^\circ$.

Figure 17.- Concluded.

[redacted]

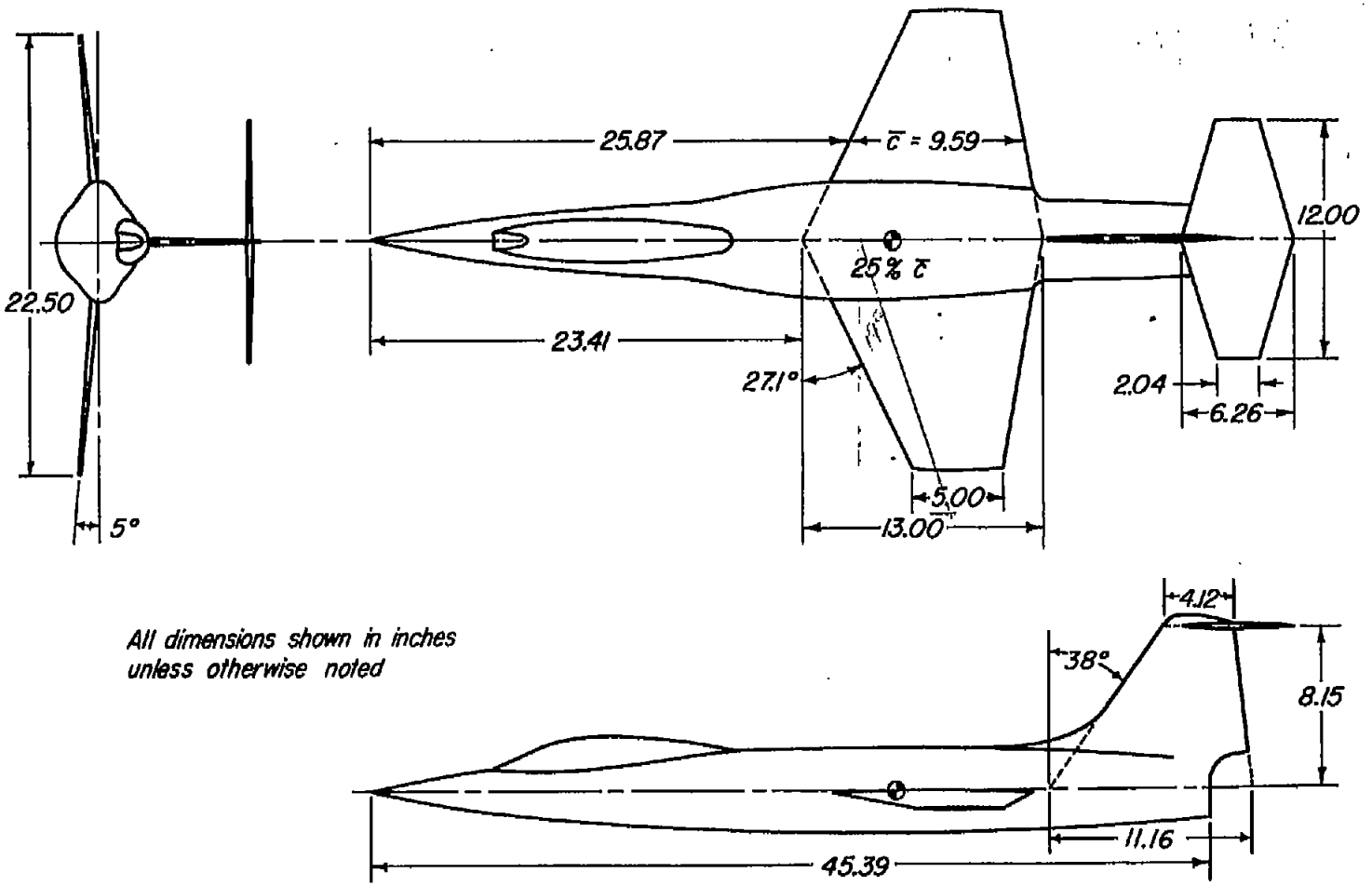

Figure 18.- Dimensional sketch of Model E.

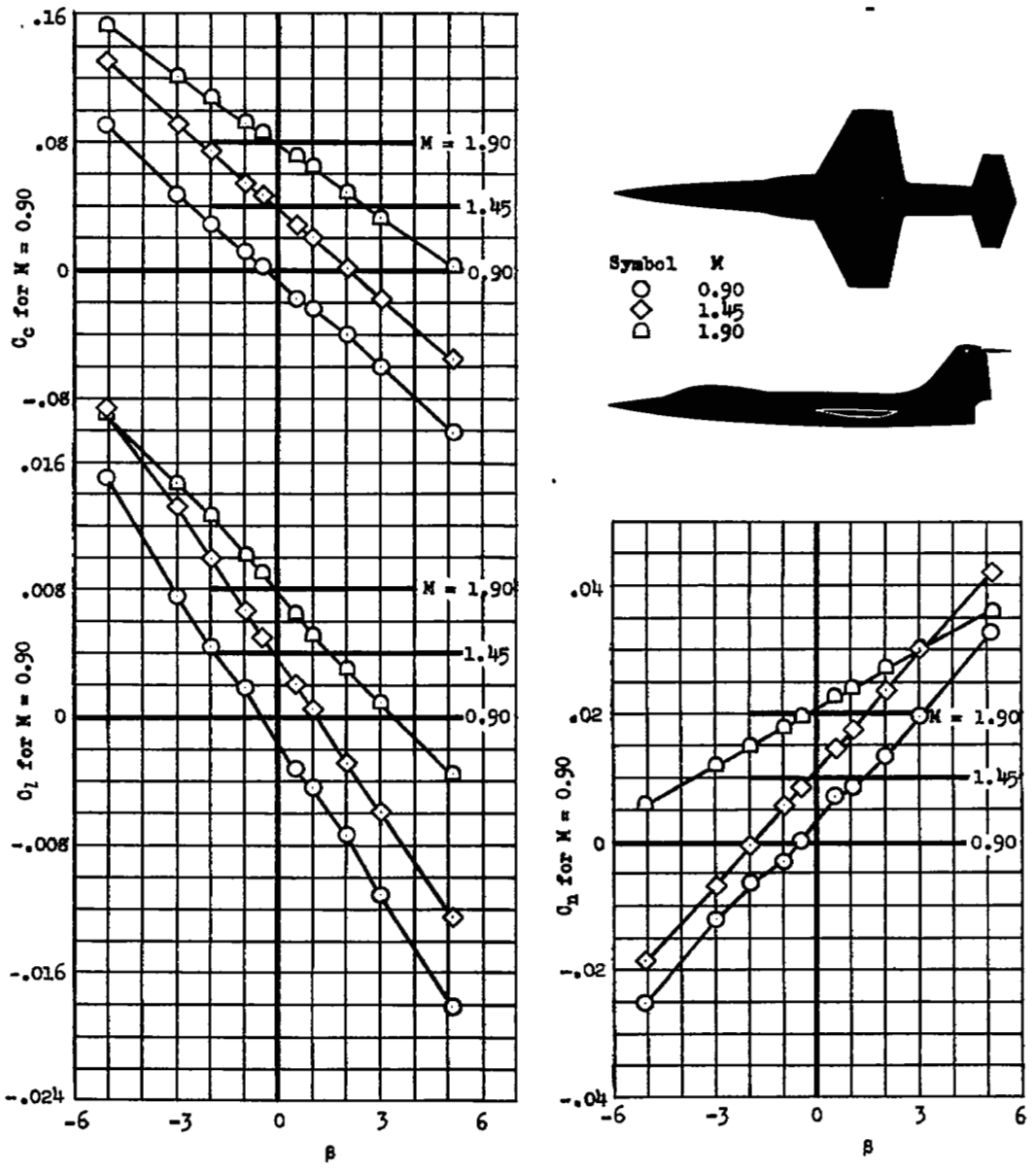

(a) Basic model; $\alpha = 0^{\circ}$.

Figure 19.- Variation of lateral-directional stability characteristics with angle of sideslip of Model E with various modifications.

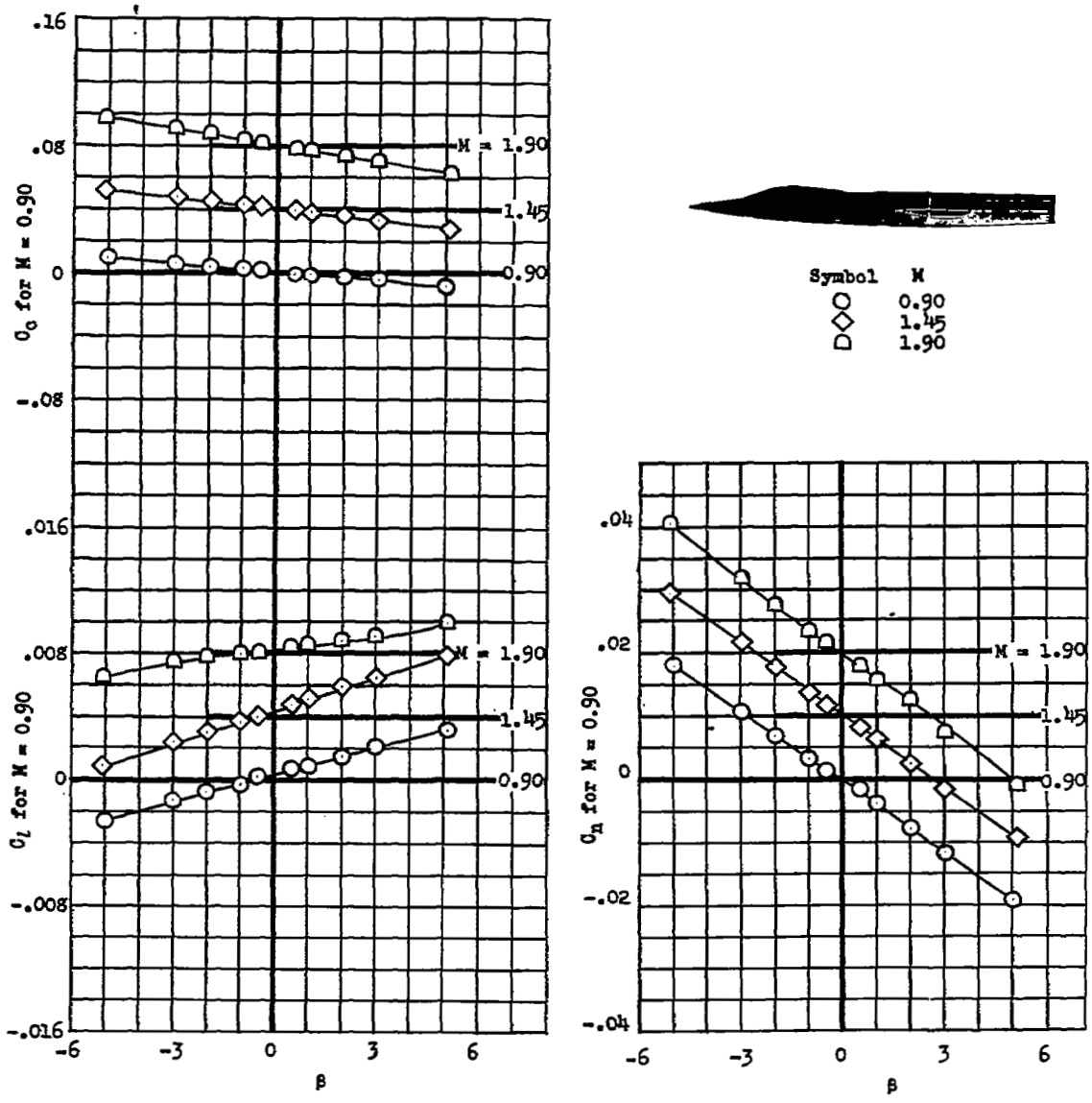

(b) Model without vertical and horizontal tail; $\alpha = 0^{\circ}$.

Figure 19.- Continued.

[redacted]

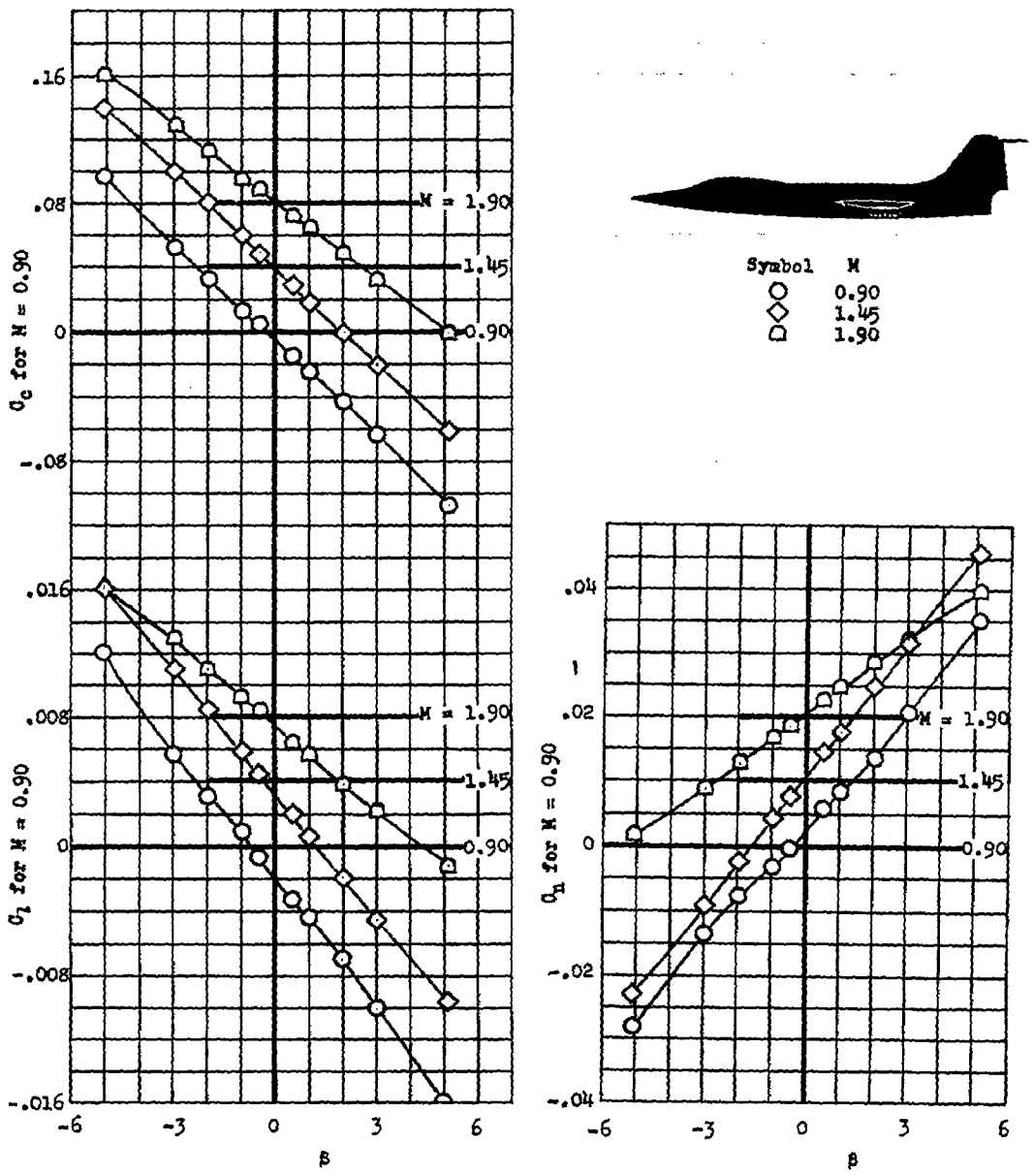

(c) Model with 10° negative dihedral wing; $\alpha = 0°$.

Figure 19.- Continued.

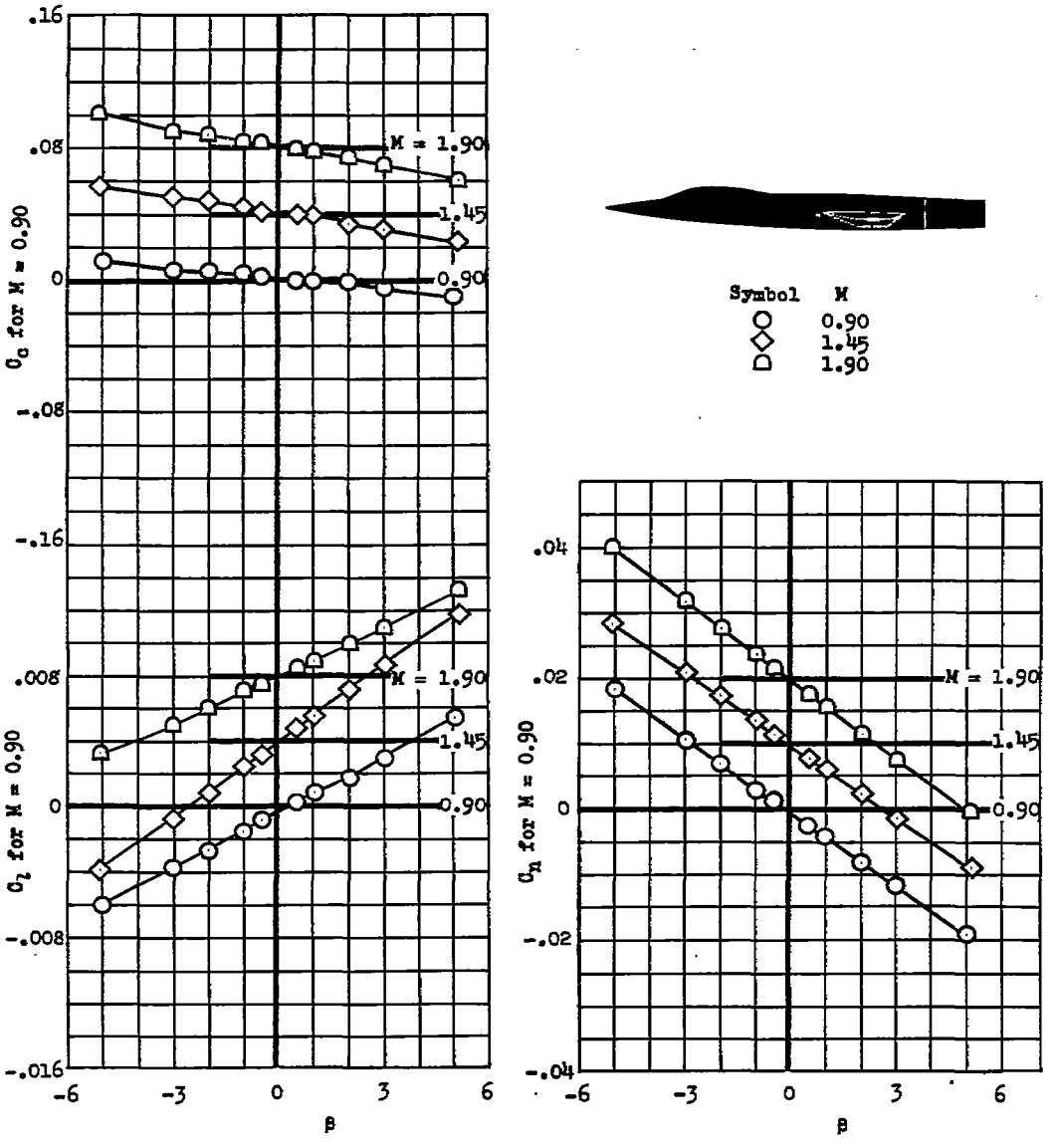

(d) Model with 10° negative dihedral wing and no vertical or horizontal tail; $\alpha = 0°$.

Figure 19.- Continued.

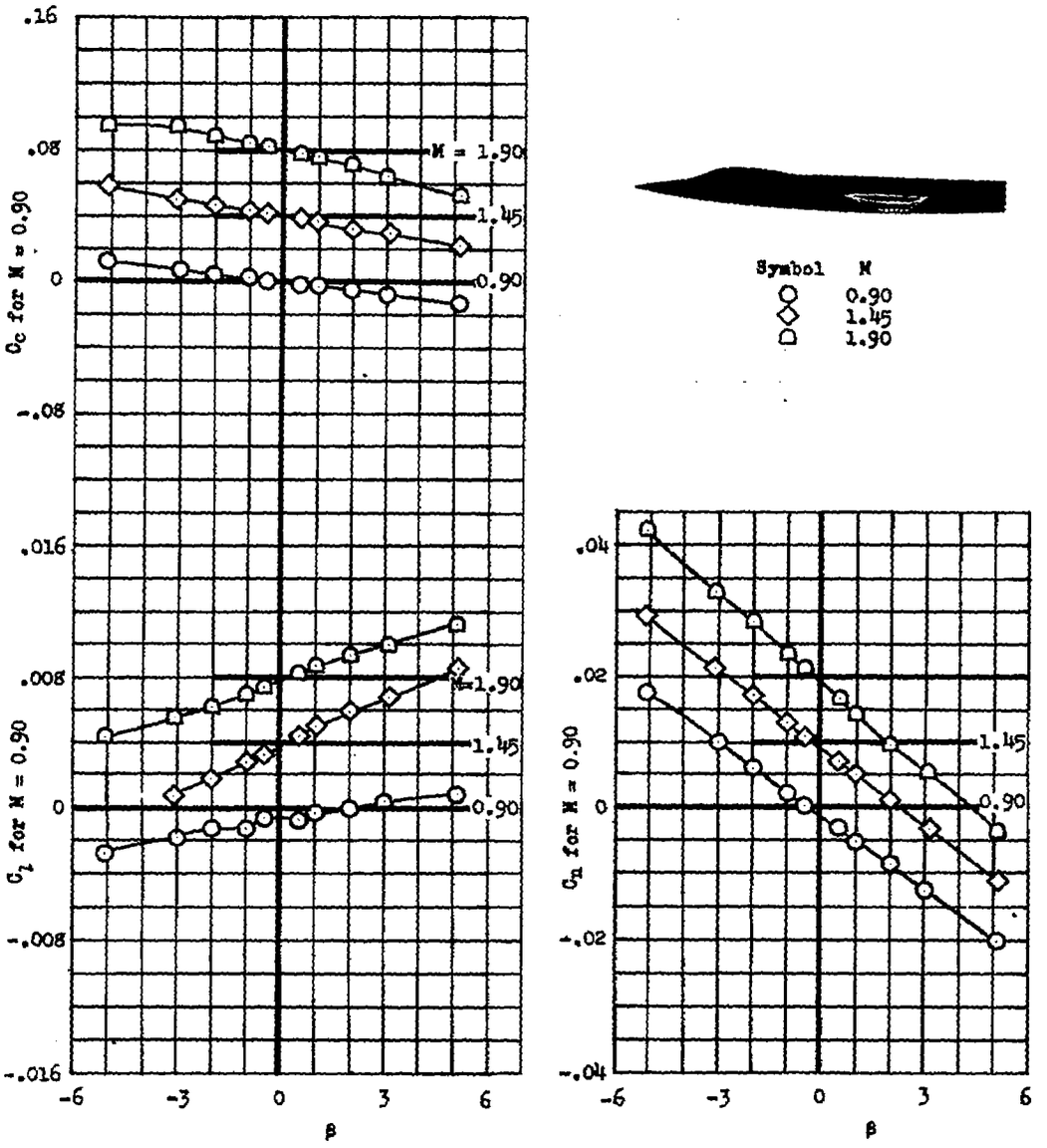

(e) Model with 10° negative dihedral wing and no vertical or horizontal tail; $\alpha = 5^{\circ}$.

Figure 19.- Continued.

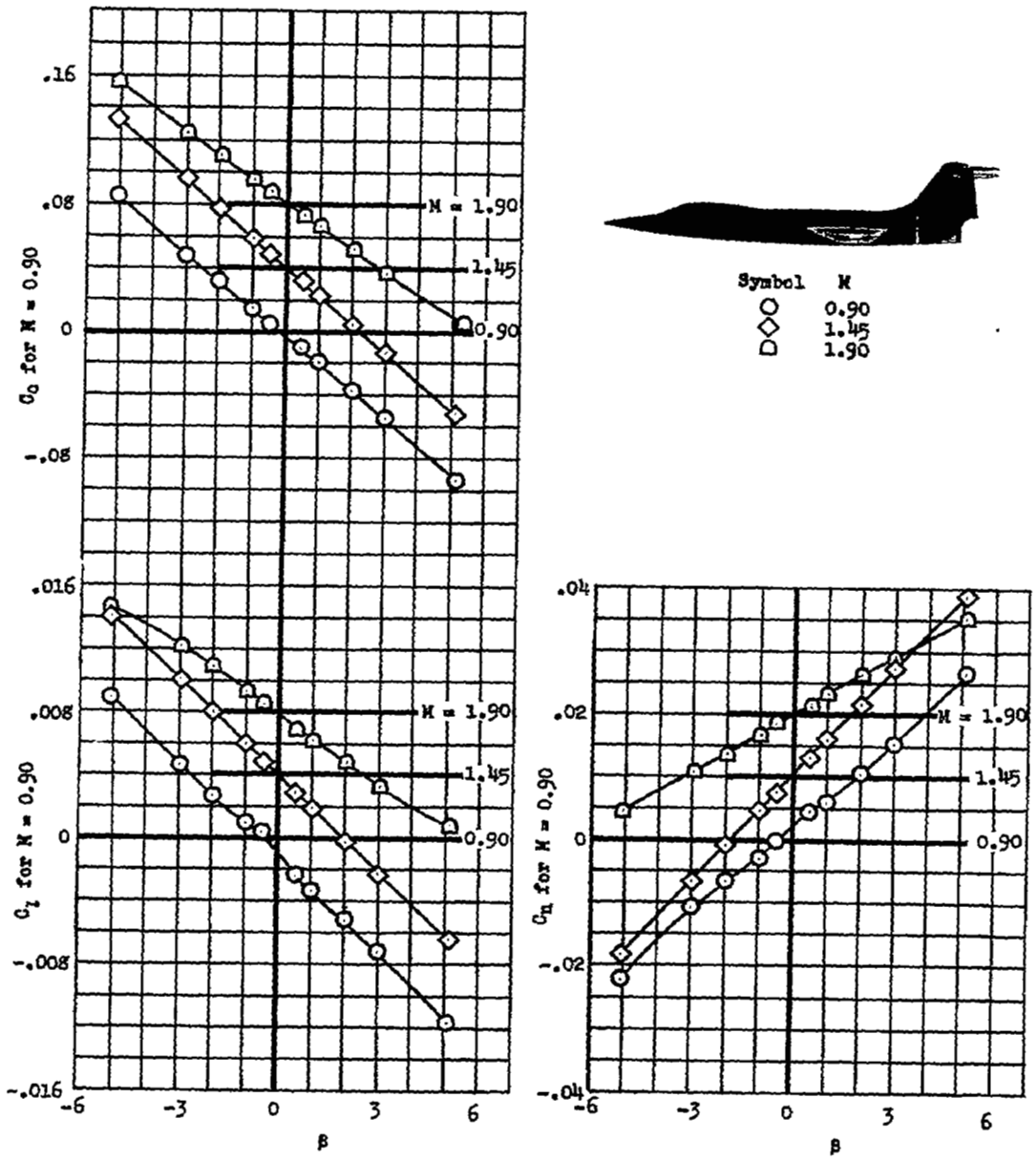

(f) Model with a small vertical tail, and 10° negative dihedral wing; $\alpha = 0^{\circ}$.

Figure 19.- Continued.

[redacted]

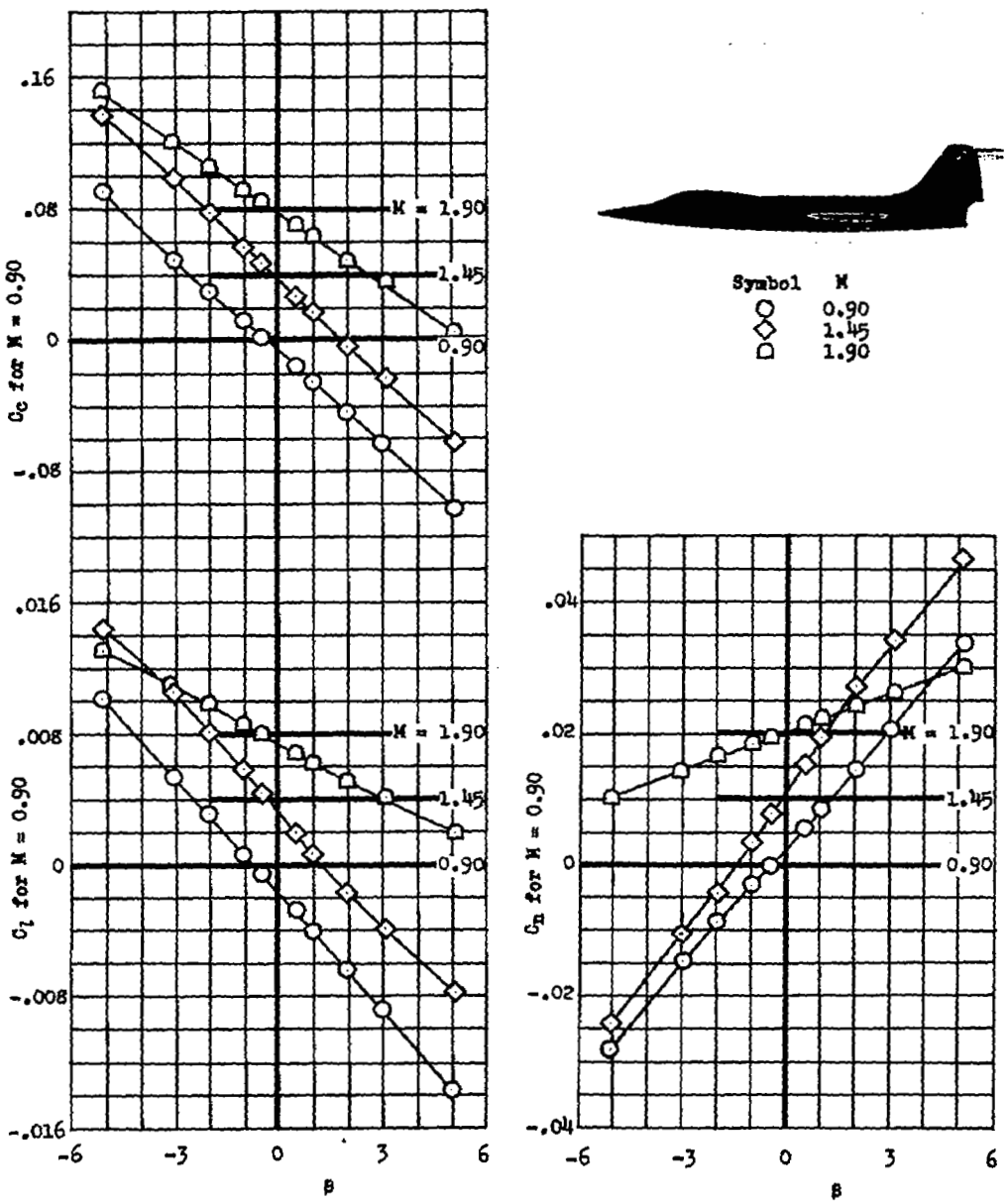

(g) Model with a small vertical tail, and 10° negative dihedral wing; $\alpha = 5°$.

Figure 19.- Continued.

[redacted]

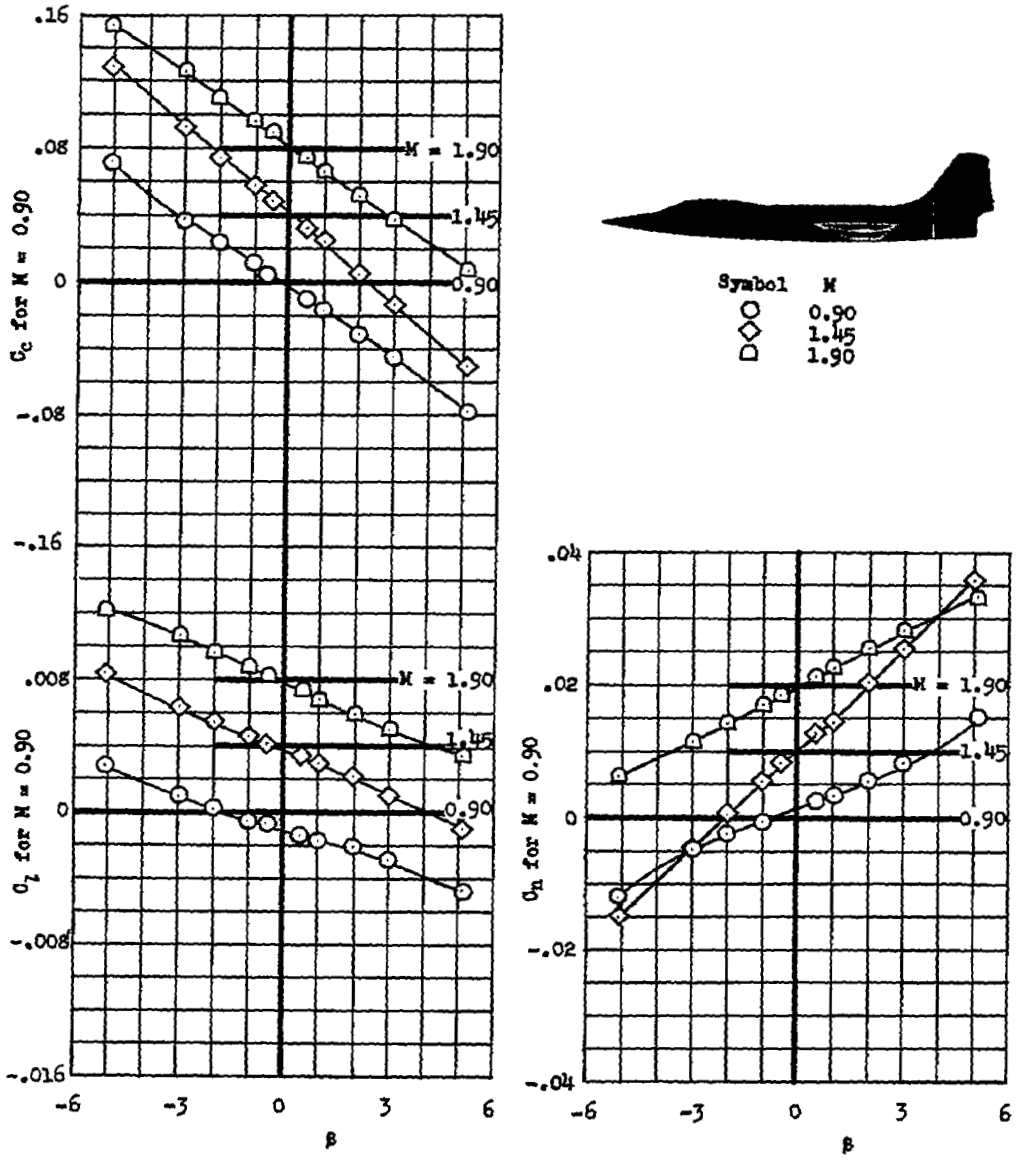

(h) Model with a small vertical tail, no horizontal tail, and 10° negative dihedral wing; $\alpha = 0°$.

Figure 19.- Continued.

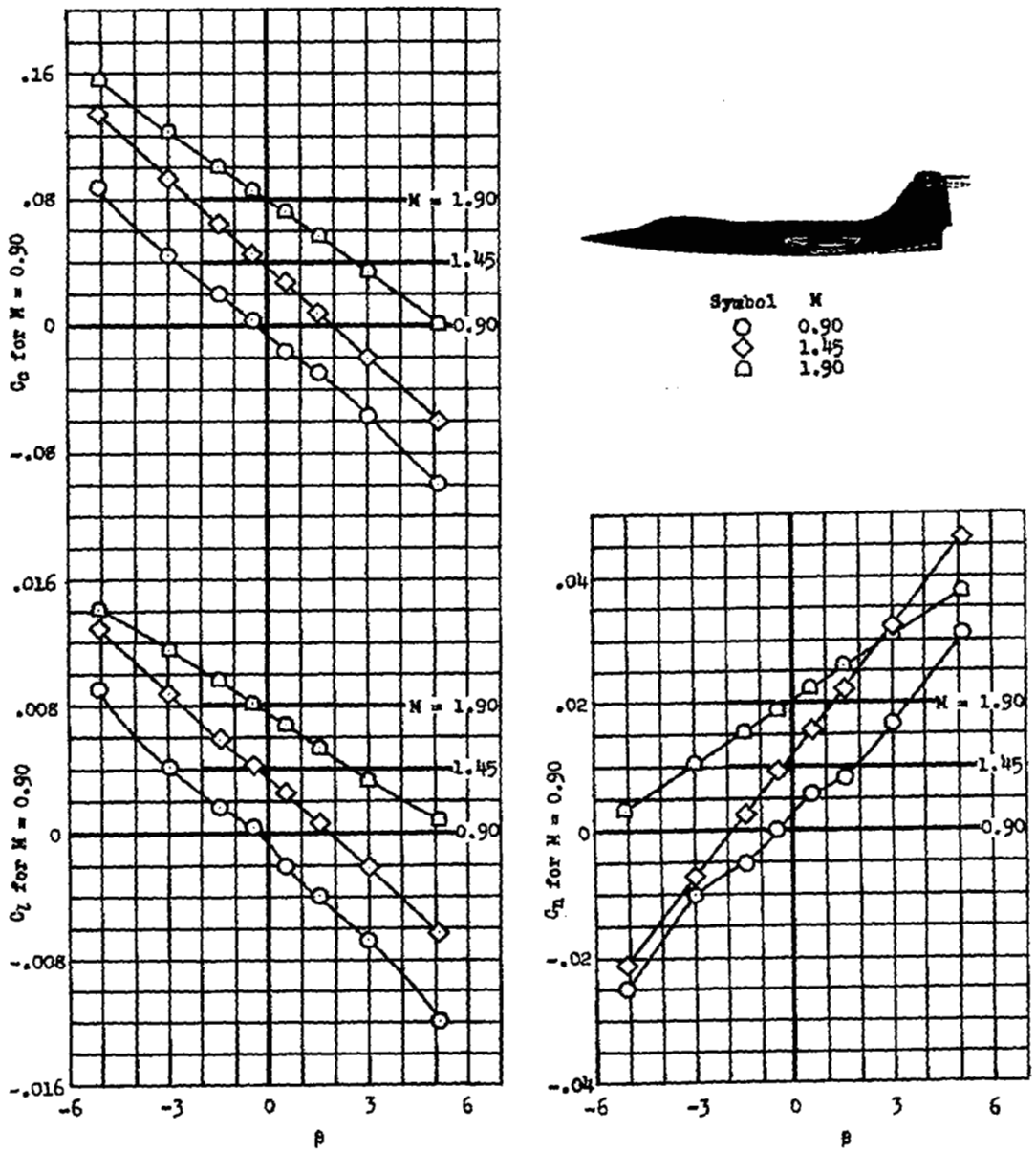

(i) Model with a small vertical tail, rear duct fairing, no internal flow, and 10° negative dihedral wing with -3° leading-edge flap deflection; $\alpha = 0°$.

Figure 19.- Continued.

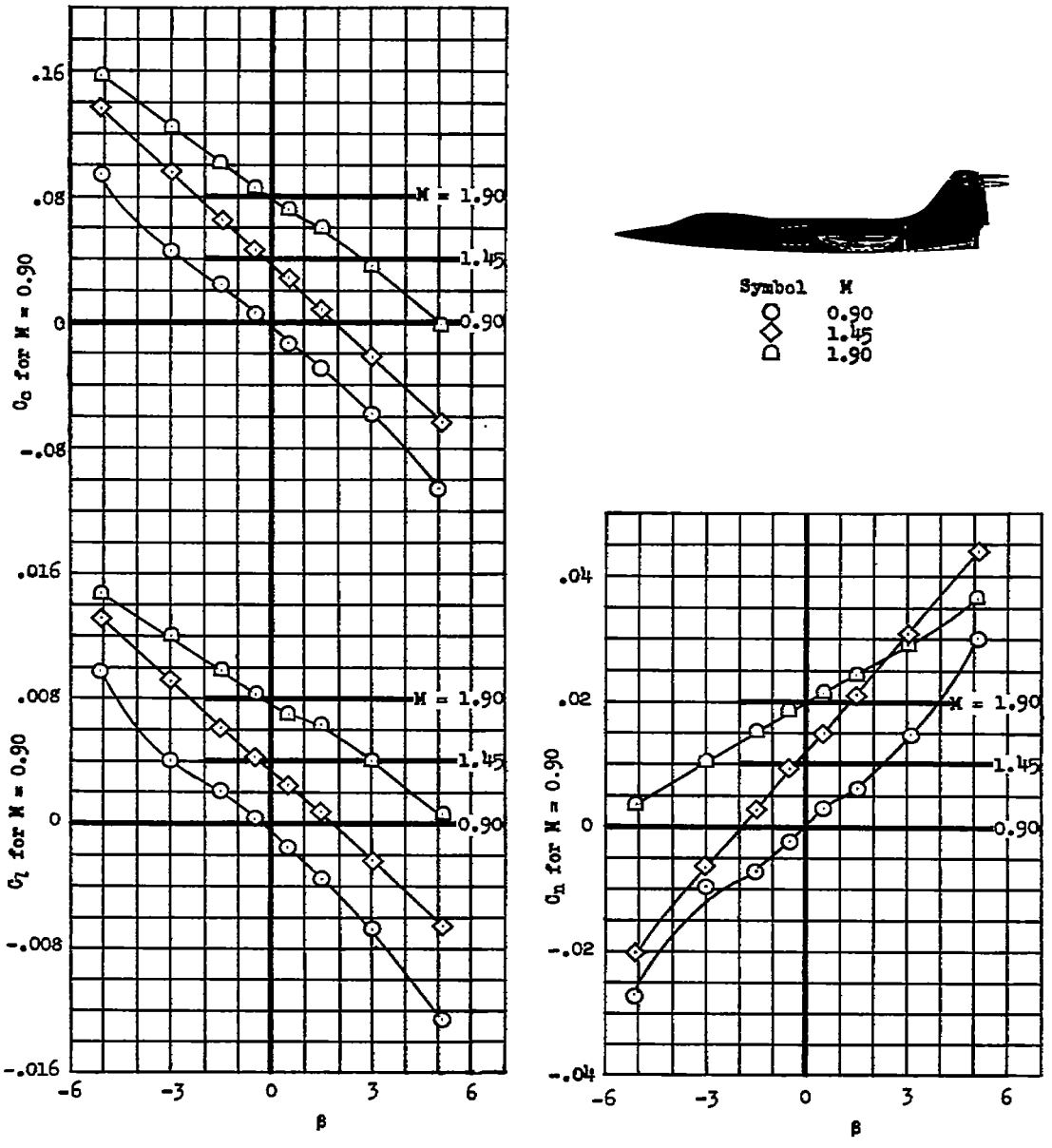

(j) Model with a small vertical tail, rear duct fairing to accommodate an $m/m_\infty = 0.8$, and 10° negative dihedral wing with -3° leading-edge flap deflection; $\alpha = 0°$.

Figure 19.- Continued.

[redacted]

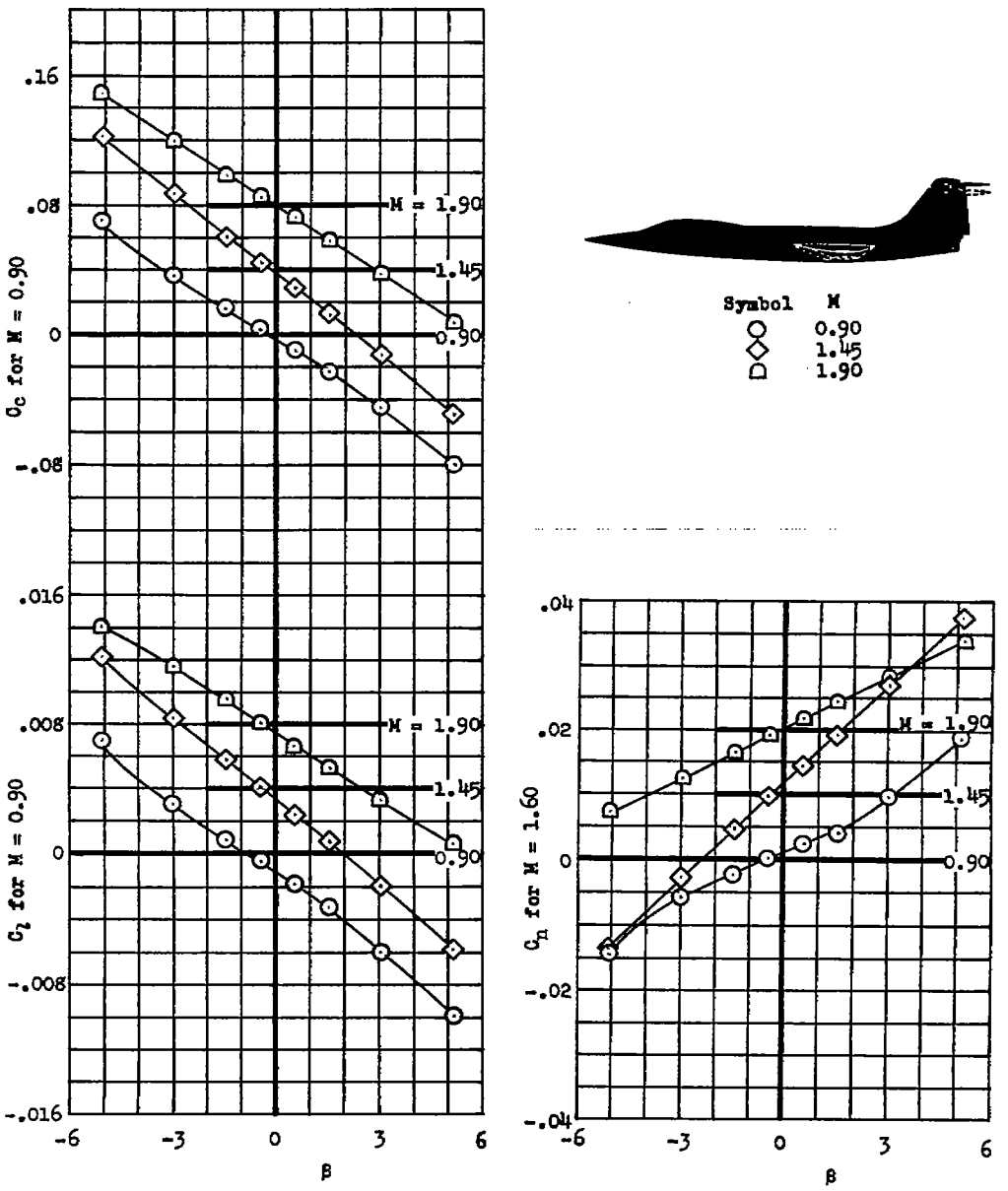

(k) Model with a small vertical tail, less rear duct fairing, no internal flow, and 10° negative dihedral wings with -3° leading-edge flap deflection; $\alpha = 0°$.

Figure 19.- Concluded.

[redacted]

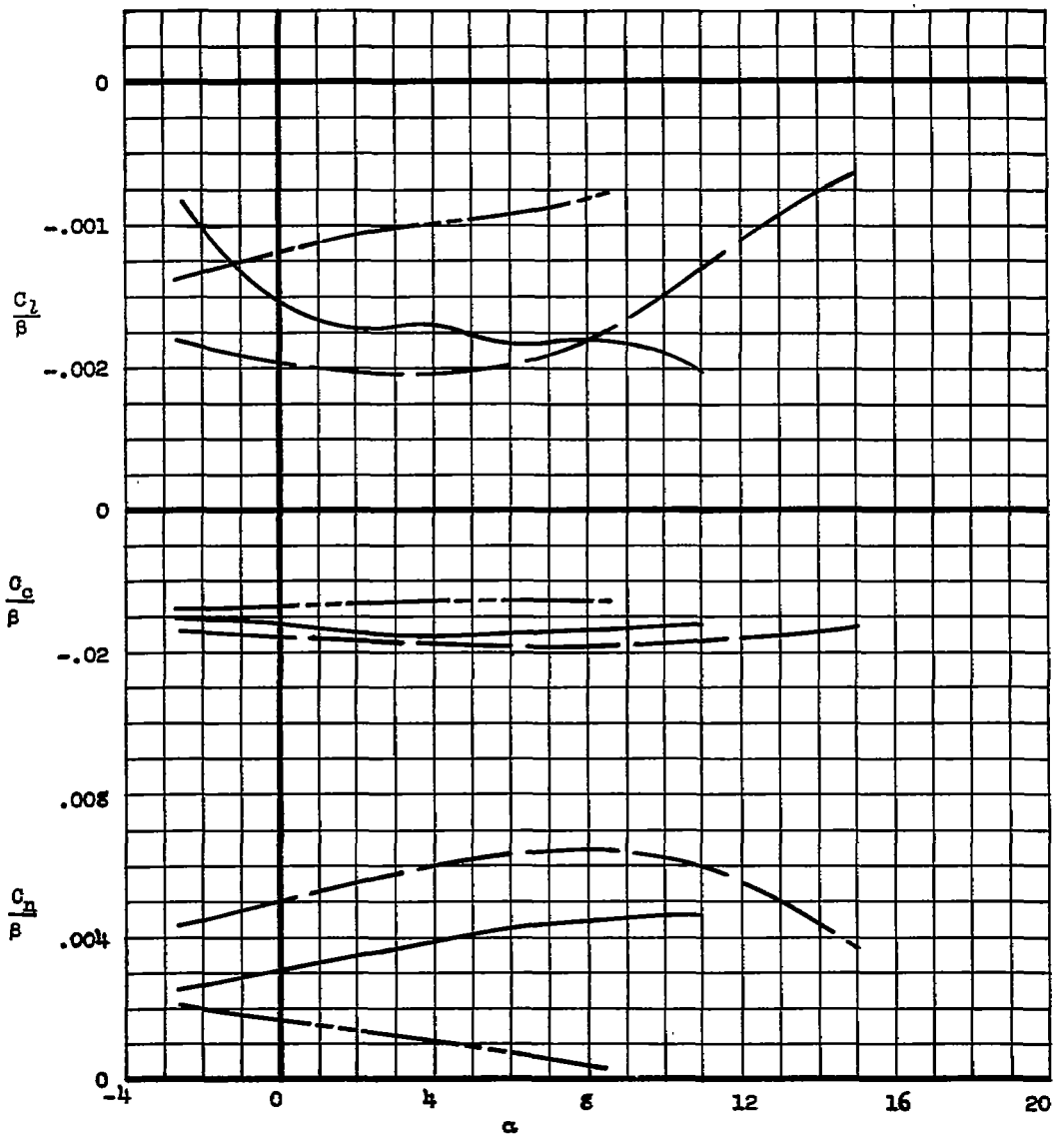

Figure 20.- Variation of lateral-directional stability parameters C_l/β, C_c/β, and C_n/β with angle of attack for Model E with a small vertical tail, and 10° negative dihedral wings with -3° leading-edge flap deflection; $m/m_\infty = 0.8$.

[redacted]